Structural characterization of single and interacting soft interfaces displaying brushes of synthetic or biomolecular polymers

---

Ignacio Rodriguez Loureiro

Kumulative Dissertation

zur Erlangung des akademischen Grades
"doctor rerum naturalium"
(Dr. rer. nat.)
in der Wissenschaftsdisziplin "Physik der weichen Materie"

eingereicht an der
Mathematisch-Naturwissenschaftlichen Fakultät
Institut für Physik und Astronomie
der Universität Potsdam
und
Max Planck Institut für Kolloid- und Grenzflächenforschung

Acknowledgements

Structural characterization of single and interacting soft interfaces displaying brushes of synthetic or biomolecular polymers

The interaction between surfaces displaying end-grafted hydrophilic polymer brushes plays important roles in biology and in many wet-technological applications. The outer surfaces of Gram-negative bacteria, for example, are composed of lipopolysaccharide (LPS) molecules exposing oligo- and polysaccharides to the aqueous environment. This unique, structurally complex biological interface is of great scientific interest as it mediates the interaction of bacteria with neighboring bacteria in colonies and biofilms. The interaction between polymer-decorated surfaces is generally coupled to the distance-dependent conformation of the polymer chains. Therefore, structural insight into the interacting surfaces is a prerequisite to understand the interaction characteristics as well as the underlying physical mechanisms. This problem has been addressed by theory, but accurate experimental data on polymer conformations under confinement are rare, because obtaining perturbation-free structural insight into buried soft interfaces is inherently difficult.

In this thesis, lipid membrane surfaces decorated with hydrophilic polymers of technological and biological relevance are investigated under controlled interaction conditions, i.e., at defined surface separations. For this purpose, dedicated sample architectures and experimental tools are developed. Via ellipsometry and neutron reflectometry pressure-distance curves and distance-dependent polymer conformations in terms of brush compression and reciprocative interpenetration are determined. Additional element-specific structural insight into the end-point distribution of interacting brushes is obtained by standing-wave x-ray fluorescence (SWXF).

The methodology is first established for poly[ethylene glycol] (PEG) brushes of defined length and grafting density. For this system, neutron reflectometry revealed pronounced brush interpenetration, which is not captured in common brush theories and therefore motivates rigorous simulation-based treatments. In the second step the same approach is applied to realistic mimics of the outer surfaces of Gram-negative bacteria: monolayers of wild type LPSs extracted from *E. Coli O55:B5* displaying strain-specific O-side chains. The neutron reflectometry experiments yield unprecedented structural insight into bacterial interactions, which are of great relevance for the properties of biofilms.

Strukturelle Charakterisierung von einzelnen und interagierenden weichen Grenzflächen mit Bürsten aus synthetischen oder biomolekularen Polymeren

Die Wechselwirkung zwischen Oberflächen mit end-gebundenen hydrophilen Polymerbürsten, spielt eine wichtige Rolle in der Biologie und in vielen nass-technologischen Anwendungen. Die äußeren Oberflächen Gram-negativer Bakterien bestehen beispielsweise aus Lipopolysaccharid (LPS) - Molekülen, welche ihrer wässrigen Umgebung Oligo- und Polysaccharide präsentieren. Diese einzigartige, strukturell komplexe biologische Grenzfläche ist von großem wissenschaftlichen Interesse, da sie die Wechselwirkung zwischen benachbarten Bakterien in Kolonien und Biofilmen vermittelt. Die Wechselwirkung zwischen Polymer-dekorierten Oberflächen ist im Allgemeinen mit der abstandsabhängigen Konformation der Polymerketten gekoppelt. Strukturelle Einblicke in die interagierenden Oberflächen sind daher eine Voraussetzung, um sowohl die Wechselwirkungseigenschaften als auch die zugrundeliegenden physikalischen Mechanismen zu verstehen. Dieses Problem wurde bereits theoretisch angegangen, aber genaue experimentelle Daten über Polymerkonformationen unter räumlicher Einschränkung liegen kaum vor, da es schwierig ist, störungsfrei strukturelle Einblicke in weiche Grenzflächen innerhalb kondensierter Materie zu erhalten.

In dieser Arbeit wurden Lipidmonoschichten, die mit hydrophilen Polymeren von technologischer und biologischer Relevanz versehen sind, unter kontrollierten Wechselwirkungsbedingungen, d. h. bei definierten Oberflächenabständen, untersucht. Zu diesem Zweck wurden spezielle Probenarchitekturen und experimentelle Methoden entwickelt. Mittels Ellipsometrie und Neutronenreflektometrie wurden Druck-Abstand-Kurven und abstandsabhängige Polymerkonformationen im Hinblick auf Bürstenkompression und gegenseitige Durchdringung bestimmt. Zusätzliche, elementspezifische strukturelle Einblicke in die Endpunktverteilung interagierender Polymerbürsten wurden durch Röntgenfluoreszenz unter stehenden Wellen (SWXF) gewonnen.

Die entwickelte Methodik wurde zunächst für Poly(ethylenglycol) (PEG) -Bürsten definierter Länge und Bindungsdichte etabliert. Für dieses System zeigte die Neutronenreflektometrie eine ausgeprägte Durchdringung der Bürsten, die in gängigen Bürstentheorien nicht erfasst wird und daher rigorose simulationsbasierte Studien motiviert. Im zweiten Schritt wurde der gleiche Ansatz auf realistische Modelle der äußeren Oberflächen Gram-negativer Bakterien angewandt: Monoschichten von aus E. coli O55 B5 extrahierten Wildtyp-Lipopolysacchariden, welche stammspezifische O-Seitenketten tragen. Die Neutronenreflektometrie-Experimente lieferten nie dagewesene strukturelle Einblicke in die Wechselwirkung von Bakterienoberflächen, Welche für die Eigenschaften von Biofilme von großer Bedeutung sind.

Table of contents

1.   Introduction

1.1 Interacting soft interfaces

Biological matter is largely composed of soft interfaces formed by two-dimensional molecular assemblies [1-4]. Membranes and protein- or carbohydrate complexes represent a large percentage of the mass of cells and tissues, and the physical interactions between their surfaces are responsible for both their function and structural organization. Membrane adhesion or vesicle release, for example, are intra-cellular processes characterized by a high degree of spatiotemporal reorganization [5]. This reorganization requires continuous adjustments of the membrane interactions by the organism. The diffusion of biomolecules between membrane surfaces is possible due to the hydrodynamic pathways generated when repulsive interaction profiles prevent contact between adjacent membranes. On the other hand, membrane adhesion or membrane fusion arise from well-defined membrane separations, created by attractive interaction profiles. The characteristics of membrane-membrane and membrane-surface interactions also govern processes such as cell adhesion [6], bacteria interactions in biofilms [7], biomineralization [8] and the adsorption of organisms to natural and artificial materials [9]. Also in technology the interaction between such soft interfaces plays an important role, in applications such as liquid purification and separative chemistry [10], lubrication [11], or cell-sheet harvesting [12].

When two soft interfaces interact in a liquid medium, the whole spectrum of interfacial forces comes into play, including electrostatic and van der Waals (vdW) forces, hydrogen bonding, and solvation and steric forces [13]. The contribution of each type of force will depend on the surface chemistry and on the composition of the liquid solution. This means that the molecular composition of such interacting surfaces will dictate the strength and range of the interaction, as well as whether they attract or repel each other. The interaction between biological membranes, for example, will be different if they are composed of neutral or charged lipids, or if they have or lack membrane-bound saccharides, polypeptides, and macromolecules [5, 14]. In technology, liquid/liquid interfaces are commonly stabilized with self-assembled amphiphilic surfactant or polymer layers, with the aim of rendering their mutual interaction more repulsive.

An important class of soft interfaces are those decorated with polymer brushes. They are the main subject of this thesis. In technology, they are used for colloidal stabilization or for shear lubrication. In biology, polymer-decorated surfaces can be found in the glycocalyx of certain cells. In particular, and as will be explained further below, the outer surface of Gram-negative bacteria is composed of sugar polymers (lipopolysaccharides). The interaction between such polymer decorated interfaces will be different if the polymer chains are able to mutually interpenetrate [15, 16]. This means that the physics behind the interaction between these type of interfaces is closely linked to the molecular conformation of the polymer chains, which vary on length scales of few Å to many nm [13]. Therefore, structural insight into the interaction is extremely valuable, but at the same time difficult to obtain for different reasons. First, scanning techniques like atomic force microscopy (AFM) or scanning tunneling microscopy (STM) cannot access the polymer chains because they are "buried" between the two surfaces to which they are grafted. In addition, and as stated above, the length scale of these structures is typically between a few Å and many nm, which are far below the resolution limit of optical microscopy and too small to be use fluorescent labels. Finally, structural changes upon interaction, such as the conformation of polymer chains, are strongly dependent on thermodynamic conditions like pressure and temperature. This means that cryotechniques are also not good candidates for studying these structures. Because of all these limitations, the only available techniques are mainly X-ray and neutron scattering. These are powerful tools to study the structure of interfaces at molecular length scales [17, 18], as they have access to buried interfaces, are usually non-destructive, and can be used under a wide range of conditions including ambient and physiological conditions. Moreover, they provide truly sample-averaged structural information rather than the isolated point-by-point structures often obtained by scanning techniques.

Specular reflectometry, which is one of the main techniques used in this work, reveals scattering length density (SLD) profiles perpendicular to an interface [17, 18]. For X-rays, the SLD of a medium is proportional to its electron density, while for neutrons it depends on its nuclear composition. In a neutron or X-ray specular reflectometry experiment, the relative intensity R of a beam reflected from a planar interface is recorded as a function of the perpendicular scattering vector component $q_z = \frac{4\pi}{\lambda} sin\theta$, where θ is the incident angle and λ is the X-ray or neutron wavelength. By analyzing the reflectivity curve, R(q_z), the interfacial

SLD can be reconstructed. The obtained SLD profiles can then be interpreted in terms of interfacial distributions of chemical components, based on their known characteristic electron or nuclear densities [19-21]. In neutron reflectometry, selective deuteration is commonly used to enhance the SLD contrast between different chemical components and thus to better discriminate between their interfacial distributions. With X-rays, direct sensitivity to the distribution of chemical elements can be achieved by exploiting the q_z - dependent characteristic X-ray fluorescence emitted by the elements of interest, in a technique known as Standing Wave X-ray Fluorescence (SWXF).

1.2 State of the art

Measurements of forces between soft interfaces across water are nowadays common practice. Pressure-distance curves, $\Pi(D)$, which provide the relation between the surface separation D and the dehydrating pressure Π, can be obtained with several methods. In so-called surface force apparatus (SFA) experiments [13, 22], the normal force F between two solid surfaces is recorded and translated into the corresponding interaction pressure Π. Importantly, the water chemical potential is D-independent and set by the reservoir. The same holds for a related technique named colloidal probe force spectroscopy, in which particles are brought into contact with functionalized surfaces [23]. The most common way of measuring $\Pi(D)$ involves multilamellar samples but is limited to systems that spontaneously assemble into periodic multilayers, like lipid or surfactant multibilayers. $\Pi(D)$ is then determined by subjecting the multilayers to controlled dehydrating osmotic pressures. The latter can be generated by the addition of hydrophilic polymers into the aqueous phase, which compete for the water molecules, i.e., depress the chemical potential, and thereby reduce the water layer between the layers [24]. The dehydrating pressure then corresponds to the osmotic pressure of the polymers in the solution. Higher dehydrating pressures can be generated via vapor exchange with a water reservoir of depressed chemical potential. The surface separation D can then be worked out from the lamellar periodicity of the multilayers, which is accessible by x-ray or neutron diffraction.

However, experimental setups suited for the measurement of interfacial forces are typically inadequate for a structural investigation with reflectometry techniques. The main reason is that reflectivity requires perfectly planar samples of lateral extensions of square millimeters (x-rays) to several square centimeters (neutrons). Bringing two such surfaces into a perfectly

parallel alignment at interaction distances of the order of 10 – 100 nm is very difficult. There have been various approaches to this challenge over the last decade, as summarized in a review article by Wei & Prescott [19]. Hamilton *et al.* performed NR measurements while keeping two functionalized planar solids in a parallel alignment at separations of less than 100 nm [25]. With this strategy they reconstructed the density profiles of polystyrene (PS) brushes interacting across toluene at two surface separations. Selective deuteration was employed in order to maximize the SLD contrast between the polymers and the solvent. Along the same line, in order to highlight the level of brush interpenetration, one deuterated and one hydrogenous brush was used. In their studies, interpenetration was found to increase with decreasing surface separation, but not as much as would be expected if the opposing brushes overlapped without mutual compression. In a recent study by Abbott *et al.* a flexible polymer sheet was used to compress hydrated single polymer brushes [26]. The idea was that this would facilitate the alignment and the exertion of compression forces. However, both strategies suffer from limitations: the use of two solid surfaces is intolerant to impurities and it is difficult to reach nanometric surface separations. On the other hand, the use of a plastic membrane is associated with high roughness on one side and hampers sophisticated surface functionalizations.

1.3 Aim of this thesis

In the present thesis, a toolset to investigate the distance-dependent structure of interacting soft interfaces of biological and technological relevance is established. This includes the development of sample preparation methods, sample environments and the use and adaption of neutron and x-ray scattering techniques. The toolset is applied to an important class of soft interfaces, namely those featuring end-grafted brushes formed by synthetic or biomolecular polymers.

First, a well-defined system composed of lipid anchored polyethyleneglycol (PEG) brushes is investigated. It serves as a proof of principle and, at the same time, has great technological relevance, since synthetic brushes are widely used in wet- and biotechnology. As mentioned above, applications include the biocompatible functionalization of nanoparticles and material surfaces[27], the stabilization of colloidal suspensions[28] and foams[29], as well as

shear lubrication[11]. An architecture is developed in which two planar amphiphilic monolayers act as grafting surfaces for the polymer brushes and are brought into contact at distances as small as few tens of nm and less. These are the typical length scales relevant for the interaction of polymer brushes on biological surfaces [7, 30] and of polymer-decorated nanoparticles in biotechnology [31]. Via controlled dehydration, our double-monolayer configuration enables the tunable approach of the two surfaces and the separation-dependent structural investigation. The monolayers are composed of phospholipids and lipopolymers (PEG-lipids), supported by a hydrophobized planar solid on one side, but free-standing on the other side. With that, a homogeneous surface separation on the planar substrate is readily realized, in contrast to approaches involving two planar solids, where creation of a defined interaction distance is generally difficult [19]. Ellipsometry is used to obtain the pressure-distance curves of interacting brushes of various polymerization degrees and grafting densities. Neutron reflectometry (NR) is used to determine the brush conformation as a function of the grafting surface separation. To this end the reflectivity curves are described in a wide separation range with a common model based on the volume fraction distributions of all chemical components and their distance dependence. Our results reveal strong interpenetration which is not predicted by standard theoretical models.

In a second part, element-specific density profiles in interacting soft interfaces are obtained by SWXF. With neutron reflectometry, the polymer and lipid distributions are obtained. However, the brush endpoint distribution and the grafting surface position, very meaningful features, are only accessible with SWXF. Therefore, the same type of samples as in the previous part are used, but with end-point-sulfur-labeled PEG-lipids. This enables us to simultaneously localize the brush grafting surface (via the phosphorus atoms present in the phospholipid headgroup) and the polymer endpoint distributions (via their sulfur atoms) under various interaction conditions. Our results show that SWXF is suited for the structural characterization of interacting soft interfaces, but as explained in the corresponding article (see section 4, reprints), working with bimodal distributions like the ones used is a challenging task.

Finally, the methodology established with the synthetic polymer brushes in the first two parts is applied to truly biologically relevant interfaces displaying linear macromolecules,

lipopolysaccharides (LPSs), which are the main constituents of the outer monolayer of the Gram-negative bacterial outer membrane (Figure 1) [32, 33]. Apart from their structural role, LPS surfaces mediate the interaction of bacteria with their surroundings and act as protection against harmful molecules. LPS molecules consist of a vastly invariant part, constituted by the fundamental building block Lipid A and the 'core' oligosaccharide. Lipid A possesses four to seven hydrocarbon chains and two phosphorylated, negatively charged glucosamines. The core oligosaccharide is composed of eight to twelve sugar units and carries additional negative charges in the form of phosphate and carboxyl groups. A variable fraction of LPS molecules (called 'smooth' LPS) possess strain-specific O-antigens (O-side chains) in the form of repetitive oligosaccharide motifs [34, 35]. However, the largest LPS fraction (called 'rough' LPS) lacks these O-side chains. Several *in vivo* studies [36-38] showed that Gram-negative bacteria are resistant against the intrusion of cationic antimicrobial peptides in the presence of divalent cations like Ca^{2+} or Mg^{2+}. Conversely, the outer membrane can be permeabilized with chelating agents like EDTA, which deplete the solution of divalent cations [38, 39]. This phenomenon has been drawing attention due to its fundamental importance for the mode of action of a class of antibacterial drugs [40]. Lipopolysaccharides also largely govern the mutual interaction between neighboring bacteria. This is of particular importance for bacteria in colonies and biofilms, where the bacteria are situated side by side [41]. In fact, structure and mechanics of biofilms were shown to be affected by the LPS chemistry [7]. With the help of neutron reflectometry, planar monolayers of wild-type LPS from *Escherichia Coli O55:B5* featuring strain-specific O-side chains have been characterized in the presence and absence of divalent cations and under controlled interaction conditions. Our results show that the structure of single solid-supported LPS monolayers is significantly affected by a depletion of calcium: the lateral packing is reduced and water appears to overlap with the hydrocarbon chain region. For interacting LPS monolayers liquid-like aqueous layer exists between neighboring bacteria when they are situated side-by-side, indicating that hydrodynamic pathways for the inter-cellular transport of small-enough molecules will be sustained in colonies and biofilms.
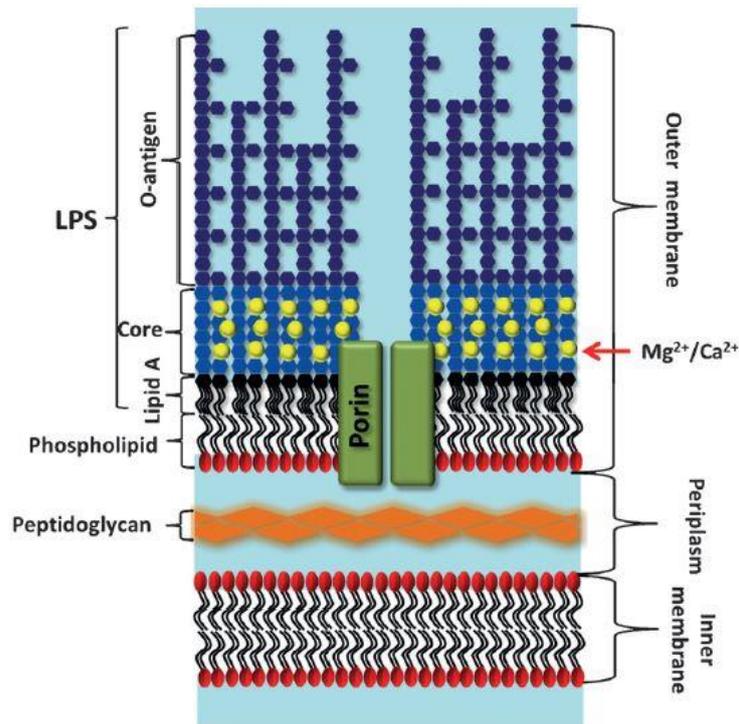
Figure 1: Schematic representation of the Gram-negative bacterial envelope. Image from Clifton *et al.* [42]

The thesis is structured in four main blocks.

First, in section 2, "Materials and sample preparation", the experimental procedures are explained, so that our experiments can be reproduced in the future.

Then, in section 3, "Theoretical background", the theory behind the experimental techniques and our system is explained, so that the thesis can be understood without additional literature.

In section 4, "Reprints", results are presented in form of reprints the three published articles corresponding to parts 1, 2 and 3 of the work (see above).

Finally, the main outcome of the thesis is summarized in section 5, "Conclusions", together with an outlook in section 6, "Outlook".

2. Materials and sample preparation

2.1 Materials and chemicals

Figure 2 shows the molecules used for preparing the polymer brushes together with the Lipopolysaccharide molecules forming the outer surface of Gram-negative bacteria. For a more detailed description of all materials and chemicals, check the "Materials and methods" section of each publication in chapter 4, "Reprints".
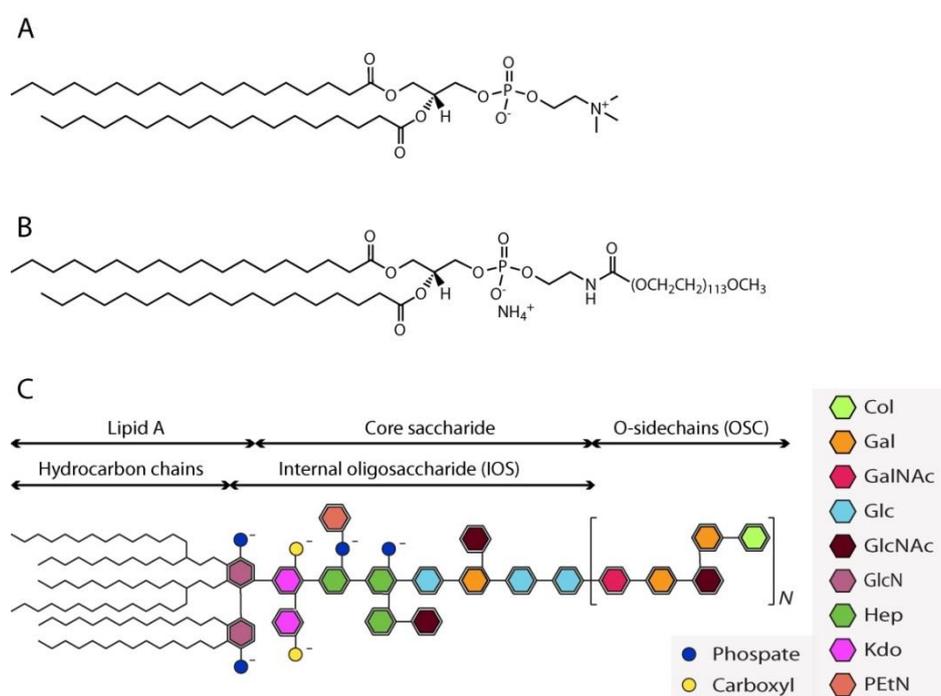
Figure 2: A) Chemical structures of the amphiphilic molecule DSPC (1,2-distearoyl-sn-glycero-3-phosphocholine). B) Chemical structure of PEG-lipid (1,2-distearoyl-sn-glycero-3-phosphoethanolamine-*N*-[methoxy(polyethyleneglycol)]).   C) Chemical structure of LPS molecules from *Escherichia Coli O55:B5*, featuring two main units: the LipidA hydrocarbon chains (LC) and a headgroup formed by the internal oligosaccharide (IOS). A certain fraction of the molecules additionally display O-side chains (OSC) consisting of pentasaccharide repeat units. Abbreviations: GlcN = glucosamine, KdO = keto-deoxyoctulosonate, PEtN = phosphorylethanolamine, Hep = L-glycero-D-manno-heptose, Glc = glucose, GlcNAc = N-acetyl-glucosamine, Gal = galactose, GalNAc = N-acetylgalactosamine, Col = colitose.

2.2 Sample preparation

In this section, the sample preparation methodology for reproducing and further developing our experiments is presented.

2.2.1 Cleaning of glassware

All glassware used –either for preparing solutions or for cleaning the substrates- needs to be extremely clean. Here is described, step by step, how to proceed. First, glassware is washed thoroughly with tap water and sodium dodecyl sulfate (SDS) to get rid of "bulk" dirt. Then, it is rinsed thoroughly with tap water to get rid of SDS. Afterwards, it is rinsed thoroughly with purified, double-deionized water to get rid of tap water contaminants and dried thoroughly with N_2 stream to avoid the creation of chloroform/water emulsions in the next step. To provide good solvents for all possible remaining contaminants, glassware is rinsed thoroughly with chloroform, acetone, ethanol and double-deionized water, in this order. To speed up the drying, it is rinsed with ethanol (more volatile than water). Glassware can now be inserted in the oven (preheated to 50 °C) until it's completely dry. Finally, it is removed from the oven and kept sealed to avoid any contamination.

2.2.2 Cleaning of Teflon holders

The Teflon holders employed for holding the substrates while cleaning and for sample deposition need to be extremely clean. First, they are washed thoroughly with tap water and sodium dodecyl sulfate (SDS) to get rid of "bulk" dirt. Then, they are rinsed thoroughly with tap water to get rid of SDS. In a next step, Teflon holders are rinsed thoroughly with purified, double-deionized water to get rid of tap water contaminants and dried thoroughly with N_2 stream to avoid the creation of chloroform/water emulsions in the next step. To provide good solvents for all possible remaining contaminants, holders are rinsed thoroughly with chloroform, ethanol and double-deionized water, in this order. To speed up the drying, a last rinsing with ethanol (more volatile than water) is needed. The holder can now be inserted in the oven (preheated to 50 °C) until it's completely dry. Finally, it is removed from the oven and kept sealed to avoid any contamination.

2.2.3 Cleaning of substrates

All the substrates on which our interacting monolayers are deposited –silicon blocks for neutron reflectometry, silicon chips for ellipsometry and multilayered chips for standing wave X-ray fluorescence- need to be extremely clean. In the case of small chips (SWXF and ellipsomerty), a clean Teflon holder is needed for this step. In the case of silicon blocks for NR, the block will be placed in a previously cleaned glass container with the surface to be functionalized exposed to the solution. The cleaning procedure is now described. First, the chip/block is washed thoroughly with tap water and sodium dodecyl sulfate (SDS) to get rid of "bulk" dirt. Then, it is rinsed thoroughly with tap water to get rid of SDS. After this step, it is rinsed thoroughly with purified, double-deionized water to get rid of tap water contaminants and dried thoroughly with N_2 stream to avoid the creation of chloroform/water emulsions in the next step. In a next step, to provide good solvents for all possible remaining contaminants, the block/chip is immersed in chloroform, acetone, ethanol and double-deionized water, in this order, for one hour. To speed up the drying, a last rinsing is done with ethanol (more volatile than water). The chip/block is then dried thoroughly with N_2 stream and inserted in the UV-Ozone chamber for one hour. It is then removed from the UV-Ozone chamber and rinsed thoroughly with purified, double-deionized water. The block/chip can now be inserted in the oven (preheated to 50 °C) until it is completely dry.

2.2.4 OTS functionalization

Chips or blocks for OTS deposition are first cleaned as described in the previous section. Once the chip is completely dry, it is removed from the oven and inserted in 50 mililiter of anhydrous hexadecane. This needs to be done fast, while the chip is still warm. The surface to be functionalized needs to be exposed to the solution. Now, 20 microliter of OTS are added and wait for one hour. Remove the OTS-hexadecane solution and add hexadecane (does not need to be anhydrous). After 15 minutes, the hexadecane is removed and replaced by ethanol. After 15 more minutes, ethanol is removed and new ethanol is added. This step will be repeated as many times as needed until no

hexadecane drops are left in the ethanol. The chip/block is now dried under N_2 stream. The success of the OTS coating can be checked by pouring water droplets on the surface. If the surface is hydrophobic, drops should "slip" over the surface and the contact angle should be high by visual inspection.

2.2.5 Organic solution preparation

For preparing organic solutions, the dry material is weighed in a clean glass bottle and the selected solvent is addedwith a Hamylton syringe until the desired final concentration is achieved.

For the DSPC and PEG-lipids, chloroform was used as solvent. Solutions were prepared with a final concentration of 2 mg/ml.

For the LPS, the solvent used was a mixture of liquid phenol (9:1 phenol:water v:v) with chloroform and petroleum ether in a volume ratio of 2:5:8. The final concentration of our solutions is 1 mg/ml. Sonication is needed for dissolving the molecules, and the solution is hazy after sonication.

2.2.6 Sample deposition

The single/interacting monolayers are prepared using a Langmuir-Blodgett trough. The trough surface is cleaned with a powder-free tissue and a small amount of chloroform. This step is repeated with ethanol. Once the trough is clean, it is filled with purified, double-deionized water. Water is removed and this step is repeated until the surface is perfectly clean. This is achieved when the surface pressure experiences no change upon closing/ opening the barriers. Subsequently, the trough can be filled with the desired subphase (water or salt solution). The chip/block is placed in the holder with the hydrophobic surface facing the subphase. Then, the monolayer of interest can be spread at the air/water interface. This is done with a Hamylton syringe. Drops of solution are added at different points of the surface. To avoid that the drop sinks into the bulk, a drop is formed at the tip of the syringe and it is made come into contact with the water. Drops are added as an onset on the pressure, on the order of several mN/m, is observed. Wait for 10 minutes to allow for solvent evaporation. Once the solvent has completely evaporated, the monolayer is compressed to a target pressure of 35 mN/m by closing the barriers. The trough is set so that this pressure is kept constant. The chip/block can

then be moved down. The dipper must move at a speed slow enough for the barriers to keep the surface pressure constant. Once the surface has come into contact with the water, the first monolayer is transferred. The whole chip/block is now immersed under water and rotated by 90 degrees so that the surface with the monolayer is now perpendicular to the air/water interface. The lateral pressure needs to be checked and kept at 35 mN/m. Finally, the chip/block can be moved up until it is completely out of the water. If the transfer has been successful, the chip/block looks dry when leaving water because the lipid hydrocarbon tails (hydrophobic) are now exposed to air. A sketch of the sample deposition procedure is presented in figure 3.
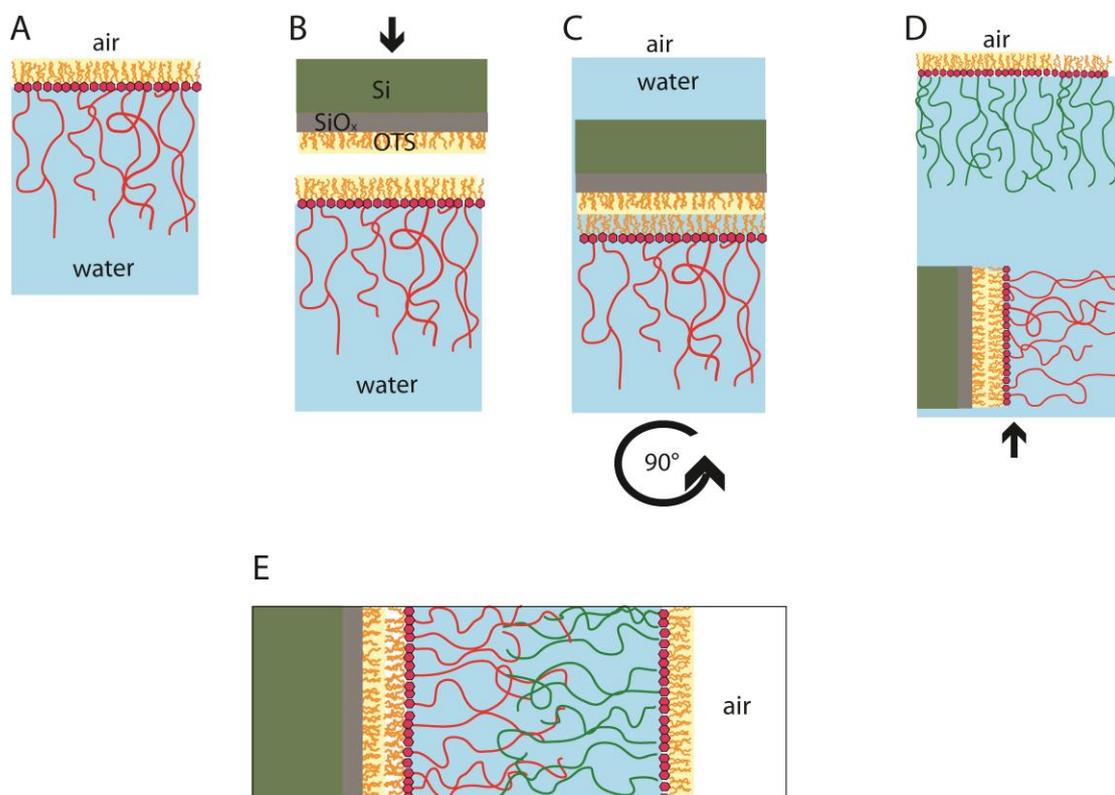

Figure 3: A) Monolayer deposited at the air water interface. B) Transfer of the monolayer via Langmuir-Schaefer deposition to a hydrophobized block. C) Once the block is under water, rotation of 90°. D) Transfer of the second monolayer via Langmuir-Blodgett deposition. E) Final architecture of two interacting lipid monolayers displaying polymer brushes.

3. Theoretical background

In this section, the main theoretical and technical aspects are described. It serves as a basis for the reprints in section 4. The section is divided in four subsections, namely neutron reflectometry, standing wave X-ray fluorescence, ellipsometry, and polymer brush theory.

Neutron reflectometry, X-ray standingwave fluorescence and ellipsometry are the main experimental techniques used in this thesis. While neutron reflectometry and SWXF gives structural information into single and interacting soft interfaces, ellipsometry enables to record pressure-distance curves, which give us information about the thermodynamics of the interaction.

On the other hand, knowledge of polymer brush theory is a prerequisite for understanding the interaction between surfaces displaying polymer brushes, which are the main focus of this thesis.

3.1 Neutron Reflectometry

Neutron reflectometry is the main technique used in this thesis. It enables to structurally characterize the interaction between two surfaces in terms of the volume fraction distributions of all chemical components. Its main theory and its relevant aspects in the context of this work are briefly described in this section.

3.1.1 Principles of neutron scattering

Neutron scattering is ideal for the structural characterization of a sample at molecular length scales because it provides structural information with high spatial resolution without destroying the sample and it provides information about buried structures [43, 44].

Because samples are probed at large length scales compared to their atomic structures (≈ 1 Å), they can be described in terms of continuous media. Their atomic structure is therefore neglected and they are parametrized with a refractive index $n(\mathbf{r})$, a complex function of the spatial coordinates $\mathbf{r}$:

$n = 1 - \delta + i\beta$

$\delta = \dfrac{\lambda^2}{2\pi}\rho$

$\beta = \dfrac{\lambda}{4\pi}\mu$

where λ denotes the wavelength of the neutrons, ρ the scattering length density (SLD) of the medium and μ the absorption coefficient of the medium for the beam. In case of cold or thermal neutrons, μ accounts for neutron capture processes, while the SLD depends on the nuclear composition of the medium:

$$\rho = \sum_j v_j b_j$$

v_j denotes the volume density of the nuclide species j, and b_j its coherent scattering length, which is tabulated for most nuclides[45].

There are two characteristics of neutrons which make them ideal candidates for studying our samples. First, their absorption coefficients are very low, so they can be used for the investigation of deeply buried structures. Second, their scattering length strongly varies between two isotopes of the same chemical element. This offers the possibility of manipulating the scattering contrast. This method is known as "contrast variation" and is particularly powerful for soft-matter and biological samples. Molecules or parts of molecules can be hindered or highlighted by isotopic labeling without changing their behavior. This is done by replacing hydrogen with deuterium (deuteration).

3.1.2 Specular neutron scattering

The specular scattering of oriented planar samples (*e.g.* thin films on a flat substrate) contains structural information along the out-of-plane (z) direction [46, 47]. Oriented samples are commonly modeled with "slab models" [48-51] (figure 4), where each slab represents a layer of constant refractive index n. Since absorption can be neglected, the sample structure is described in terms of SLD profiles rather than in terms of refractive index profiles.
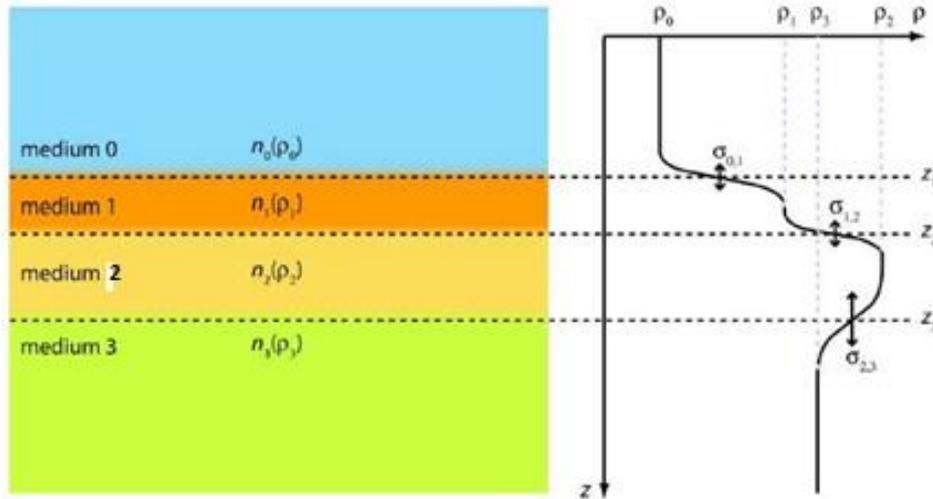
Figure 4: Slab model of an oriented sample. From [52]

The transition of ρ at the interface between two adjacent slabs is accounted for with an error function, characterized by a transition width σ.
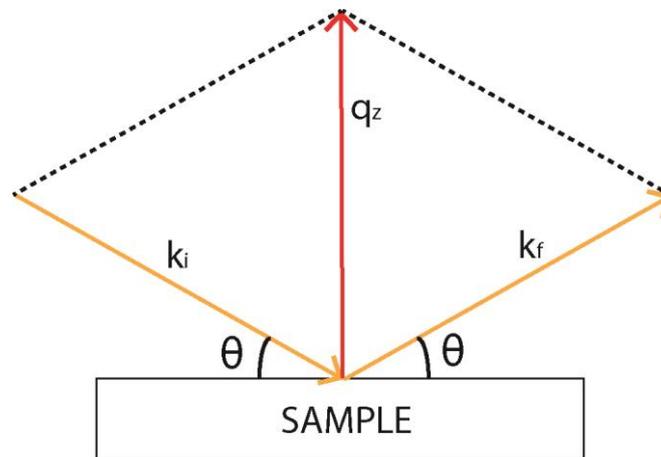
Figure 5: Specular scattering geometry.

Let a monochromatic beam with wave vector $\mathbf{k_i}$ hit an oriented sample with incident angle ϑ, as shown in Figure 5. The beam is scattered at an angle ϑ (specular reflection) and has a wave vector $\mathbf{k_f}$. The length of the wave vector is conserved (elastic scattering), so that:

$$\left| \mathbf{k_i} \right| = \left| \mathbf{k_f} \right| = \frac{2\pi}{\lambda}$$

The momentum transfer vector corresponding to the scattering process is characterized by the scattering vector q_z = $\mathbf{k_f}$ - $\mathbf{k_i}$ = $\frac{2\pi}{\lambda}$ (sin θ + sin θ) = $\frac{4\pi}{\lambda}$ sin θ.

3.1.3 Reflectivity from a single ideal interface

Consider an ideal planar interface between two homogenous media, 0 and 1, and a beam hitting the interface coming from medium 0. The out-of-plane component k_j^z of the wave vector in each medium depends on $\mathbf{q_z}$ and on the refractive indices, n_0 and n_1:

$$k_j^z = \frac{2\pi}{\lambda} \sqrt{\left(\frac{q_z \lambda}{4\pi}\right)^2 - n_j^2 - 1}$$

If absorption is neglected, we can simplify the previous expression:

$$k_j^z = \frac{2\pi}{\lambda} \sqrt{\left(\frac{q_z}{2}\right)^2 - 4\pi \rho_j}$$

The complex amplitudes of the reflected and transmitted waves are given as the Fresnel amplitude reflection and transmission coefficient:

$r_{0,1}^F = \frac{k_0^z - k_1^z}{k_0^z + k_1^z}$ and $t_{0,1}^F = 1 + r_{0,1}^F$

The specular reflectivity **R**, defined as the ratio between the reflected intensity I_r and the incident intensity I_i, is the absolute square of the complex Fresnel amplitude reflection coefficient:

$$R(q_z) = \frac{I_r}{I_i} = \left| r_{0,1}^F \right|^2$$

If the refractive index of medium 1 is lower than that of medium 0, the beam is totally reflected (R=1) below a critical q_z value, denoted with q_z^c. This value can be approximated in terms of the SLDs of the media:

$$q_z^c \cong \sqrt{16\pi(\rho_1 - \rho_0)}$$

3.1.4 Interfacial roughness

Non-ideal interfaces between two media do not possess a sharp jump in the SLD but a gradual transition. To describe this transition, error functions characterized by the transition width **σ** are used. For this case, Nevot and Croce[53] have derived how the amplitude reflection coefficient for an interface should be modified:

$$r_{0,1}^F \rightarrow r_{0,1}^F \cdot \exp(-\tfrac{1}{2} q_z^2 \sigma_{0,1}^2), \text{ where } \mathbf{exp}\left(-\tfrac{1}{2} \boldsymbol{q_z^2 \sigma_{0,1}^2}\right) \text{ is the so called Nevot-Croce factor.}$$

In figure 6, the reflectivity of an ideal interface (for two media with $\rho_0 = 0$ and $\rho_1 = 20 \times 10^{-6}$ Å^{-2}) and that of an interface with roughness $\sigma = 5$ Å is shown.
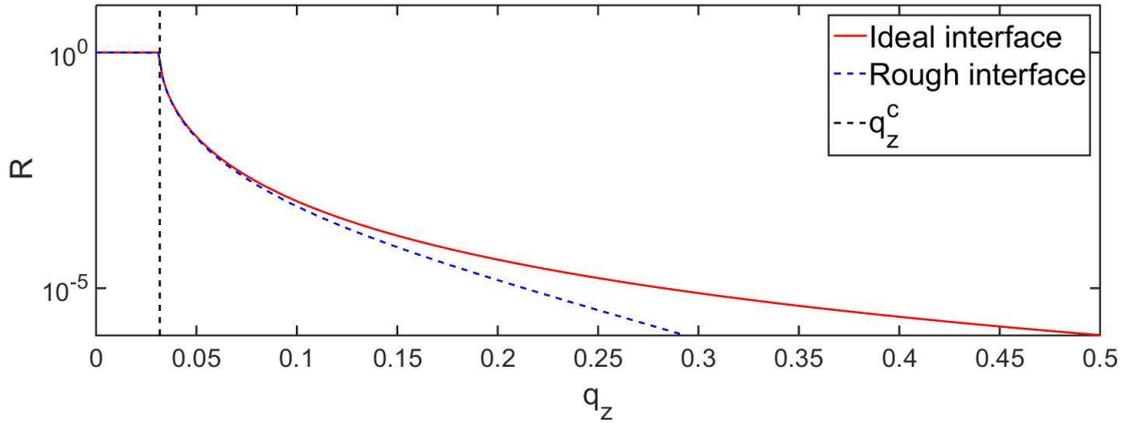
Figure 6: (red) Fresnel reflectivity from a single ideal interface. (blue) Influence of interfacial roughness.

At this point it should be noted that, in the approach taken in this thesis –described in detail in the "Material and methods section" of each paper in section 4, "Reprints"-, the slabs used to describe the volume fraction distributions of the different components are not the same slabs used for the reflectivity calculation. The continuous SLD profile of our system is discretized into hundreds of thin slabs of 1 or 2 Å of constant SLD (see Figure 7). This allows to get rid of the Nevot-Croce factor and simplify the calculations. This can be done because slabs are so highly resolved that the roughness between them can be neglected. In fact, for the maximal q_z (0.25 Å^{-1}) and for roughnesses below 1 Å, the Nevot-Croce factor approaches unity.
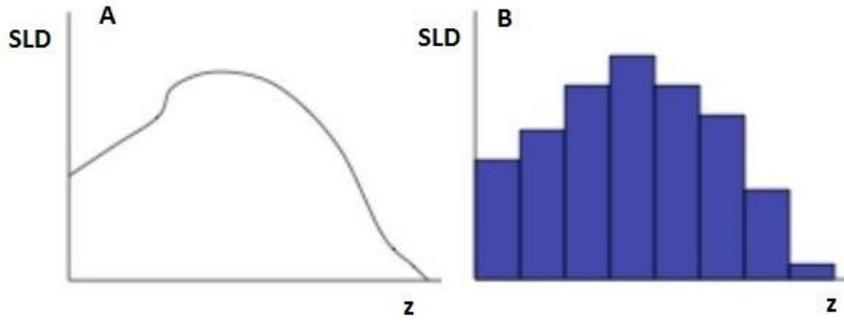
Figure 7: (A) Continuous SLD profile. (B) SLD profile after discretization into thin slabs of constant SLD.

3.1.5 Stratified interfaces

The reflectivity from N stratified interfaces can be calculated using Parrat's formalism [54]. Based on the Fresnel amplitude reflection coefficients,

$$r_{j,j+1}^{F} = \frac{k_j^z - k_{j+1}^z}{k_j^z + k_{j+1}^z} \cdot \exp(-\frac{1}{2}q_z^2 \sigma_{j,j+1}^2)$$

the effective amplitude reflection coefficient of the stratified system $r_{0,N}$ is calculated recursively starting from the last interface (between medium N-1 and medium N):

$$r_{N-1,N} = r_{N-1,N}^{F}$$

$r_{j,N} = \frac{r_{j,j+1}^{F} + r_{j+1,N} \cdot e^{2ik_{j+1}^Z d_{j+1}}}{1 + r_{j,j+1}^{F} \cdot r_{j+1,N} \cdot e^{2ik_{j+1}^Z d_{j+1}}}$, j counting downwards from N-2 to 0.

$d_j = z_{j+1} - z_j$ denotes the thickness of medium j.

The reflectivity is then given as $R(\boldsymbol{q_z}) = \left| r_{0,N} \right|^2$

A calculated reflectivity curve from 3 stratified interfaces ($\rho_0 = 0$, $\rho_1 = 15 \times 10^{-6}$ Å^{-2}, $\rho_2 = 30 \times 10^{-6}$ Å^{-2} and $\rho_3 = 10 \times 10^{-6}$ Å^{-2}, $d_1 = 15$ Å, $d_2 = 25$ Å, $\sigma_{0,1} = \sigma_{1,2} = \sigma_{2,3} = 4$ Å) is presented in figure 8.
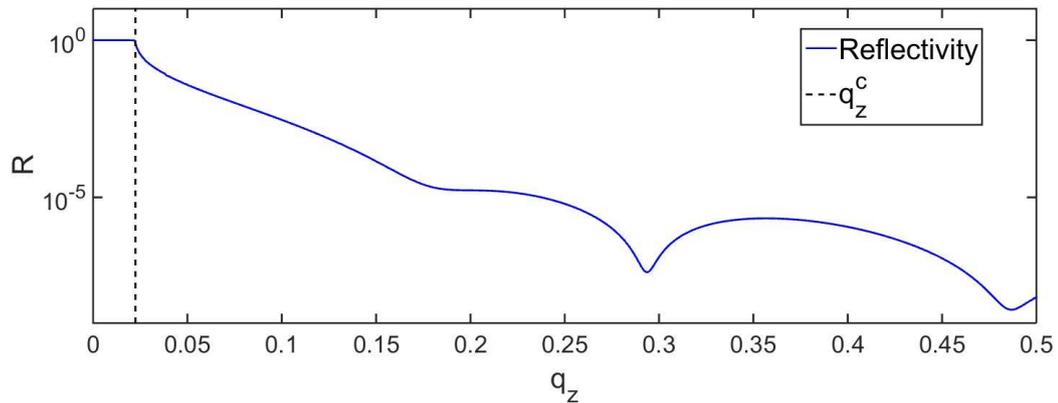
Figure 8: Reflectivity from 3 stratified rough interfaces

In contrast to the single interface case, the reflectivity from stratified interfaces shows many features like oscillations and deep minima (Kiessig fringes) caused by the interference of the waves reflected at different interfaces. The Parratt formalism constitutes a fully dynamical description of the scattering process where the intensity of the incident beam is conserved, and the reflections from each interface (including back and forth reflections) as well as the interference of all reflected and transmitted waves are considered.

3.1.6 Practical aspects of our Neutron Reflectivity measurements

In the following, some practical aspects of our reflectivity measurements will be discussed.

The most important aspect is the fact that we measure the reflectivity using a polychromatic neutron beam. The use of a polychromatic beam is often called *Time of flight* because different wavelengths correspond to different time for neutrons to travel from the neutron guide to the detector, crossing the sample. This means that neutrons detected at different times correspond to different wavelengths and with the knowledge of this time we can reconstruct the distribution in λ of neutrons. This feature enables us to record the reflectivity over a given q_z range without having to change the angle.

In the following, the calculation of neutron reflectivity from raw time-of-flight data is explained based on the article by Gutfreund *et al.* [55] .

If a polychromatic beam with $\lambda \in [\lambda_{min} , \lambda_{max}]$ is considered, the maximum and minimum q_z values for a fixed angle θ are given by:

$$q_{z,max} = \frac{4\pi}{\lambda_{min}} \sin\theta$$

$$q_{z,min} = \frac{4\pi}{\lambda_{max}} \sin\theta$$

This feature enables to record the reflectivity curve over the whole q_z range with just two angles of incidence.

The wavelength of the detected neutrons is calculated measuring the corresponding time-of-flight [55]:

$$\lambda = \frac{h t_{TOF}}{D_{TOF} m_n}$$

Where h is Planck´s constant, t_{TOF} is the time of flight, D_{TOF} is the distance between the chopper (starting point of the neutron´s flight) and the detector and m_n is the neutron´s mass.

The pick-up pulse from the first chopper is used to trigger the acquisition schedule, as sketched in figure 9. Subsequently the detector acquisition is idle during a certain delay time, t_{delay}, which can be set electronically in order to set-up a minimum time-of-flight, which corresponds to the shortest wavelength (fastest neutron) to be recorded. The minimum delay time which comes from signal conversion processes is about 2 µs. If using a constant time channel width τ_a, the detector acquisition is sequentially histogramming the detected neutrons into N_{TOF} time channels. The time-of-flight of a neutron registered in the time channel n_{TOF} is calculated according to the following equation:

$$t_{TOF} = \tau_a(n_{TOF} + 0.5) + t_{delay} - \frac{(\Phi_{off} - (\phi - \phi_{off}))}{4\pi} T$$

If the first time channel is zero, Φ_{off} is twice the angle between the trailing edge of the leading chopper blade and the physical pick-up position that sends the electronic start signal to the detector acquisition. ϕ is the opening between the choppers so that a value of zero means that there is no direct line of sight between the choppers and T is the chopper period.

Finally, in order to obtain the R(q$_z$) curve, the recorded intensity is normalized by the direct beam.
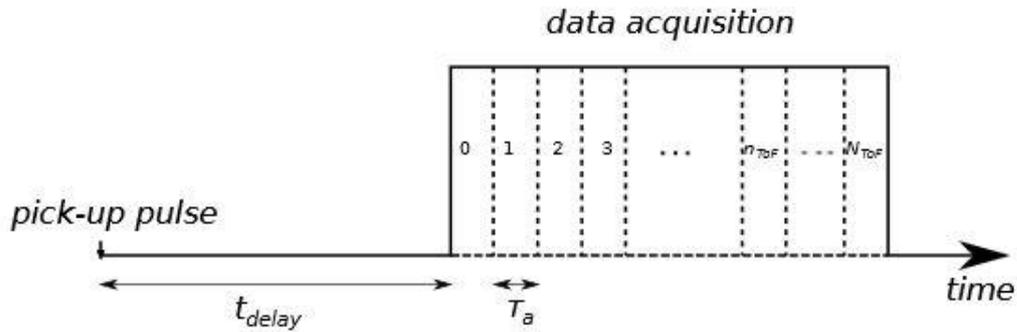
Figure 9: Sketch of the detector acquisition schedule as assumed by COSMOS. From [55]

3.2 Ellipsometry

As stated above, scattering techniques –which give us structural information- are combined with ellipsometry, which allows to determine the water layer thickness for various interacting pressures and therefore to construct pressure-distance curves, containing thermodynamic information of the interaction.

Ellipsometry enables the characterization of interfacial layers in terms of refractive indices and thicknesses. The method is based on the change in the polarization state of light (from linear/circular to elliptical) upon reflection from a surface. For a given refractive index *n*, the change depends on the layer thickness and is quantified in terms of the phase difference Δ and the amplitude ratio Ψ encoded in the ratio (ρ) between the complex reflection coefficients R$_s$ and R$_p$ for perpendicular and parallel polarizations, respectively [56].

$$\rho = \frac{R_p}{R_s} = \tan \Psi \cdot \mathrm{e}^{-\mathrm{i}\Delta}$$

Where Ψ is the ratio of amplitudes before and after reflection and Δ is the change in phase difference (δ) caused by reflection.

$$\tan \Psi = \frac{A_p^r / A_s^r}{A_p^i / A_s^i}$$

$$\Delta = (\delta_p^r - \delta_s^r) - ((\delta_p^i - \delta_s^i)$$

The superscripts *i* and *r* denote incident and reflected, respectively.

Ellipsometry has many advantages for measuring thin films. It measures very fast (in seconds) and it is a non-destructive technique. It measures changes in both the amplitude (intensity) and the phase of polarized light after reflection, hence it is very sensitive: it can detect changes in thickness of 0.1 nm and in refraction index of 0.001. Furthermore, it is suited for any interface: solid/air, solid/liquid, liquid/liquid, liquid/air, etc.

The main requirement is that there must be specular reflection from the interface (or interfaces) of interest to measure with ellipsometry. Therefore, the sample needs to be smooth. The system should also be thinner than the penetration depth of light (z), which is given by

$$z = \frac{\lambda}{2\pi\kappa}$$

Where λ is the wavelength of the incident light and κ is the extinction coefficient of the film.

The pressure-distance relations are obtained with ellipsometry in two main steps: first, the dry thickness of the system is measured. Then, based on the measured value and on the well known refractive index of water (n_{wat} = 1.33), the water layer thickness is obtained as a function of the osmotic pressure. A more detailed explanation of the measurement procedure can be found on the "Maerials and methods" section of each article in section 4, "Reprints".

3.3 Standing Wave X-Ray Fluorescence

This technique is used to gain structural insight into the interaction, but in terms of element-specific density profiles instead of in terms of the volume fraction distributions that we obtain with neutron reflectometry. While NR gives information about the polymer and lipid distributions, some specific and meaningful features like the polymer endpoint distribution or the grafting surface position are only accessible by SWXF. That´s why SXF is used in this thesis.

The Standing-wave X-ray fluorescence (SWXF) technique allows determining element-specific density profiles across an interface [57]. It is based on the element- characteristic fluorescence induced by a standing X-ray wave. The θ-dependent fluorescence intensity of an element j, $I_j(\theta)$, scales with a spatial integral containing the elemental concentration profile perpendicular to the interface, $c_j(z)$, and the θ-dependent SW intensity, $\Phi(\theta, z)$:

$$I_j(\theta) = A \int_{-\infty}^{\infty} \Phi(\theta, z)\, c_j(z) dz,$$

where A is a pre-factor that accounts for beam footprint, fluorescence yield and detector field-of-view. Therefore, it has a weak $\theta-$ dependence [57]. The calculation of the SW intensity, $\Phi(\theta, z)$, is described in the next section.

This technique has been used for studying many interfacial phenomena in solid, liquid, and gas phases [58-66]. Planar, nanometric multilayers are used to create strongly modulated standing waves above the terminal surface, close to the Bragg reflection condition [59, 60], and this leads to high resolution perpendicular to the interface. In the past, these studies dealt only with the localization of heavy elements. Biological surfaces needed to be labeled with such heavy elements (not naturally present in biological matter) [67]. It was only recently that a development of SWXF was implemented by Schneck *et al* [57] enabled the localization of lighter and biologically relevant chemical elements like P and S with atom scale precision and without any labels. This work serves as a starting point for our SWXF studies.

3.3.1 Calculation of the illumination intensity profile, $\Phi(\theta, z)$

The calculation of the illumination intensity profile, $\Phi(\theta, z)$ or $I^{illu}_{q_z}(z)$, is explained in the following, based on the book of Born and Wolf [68] and the thesis of Schneck [52].

Consider E_0 to be the amplitude at z = 0 of an electromagnetic wave arrivinging from medium 0 and hitting a set of N-1 stratified slabs. Media 0 and N are semi-infinite bulk media, as depicted in figure 10.
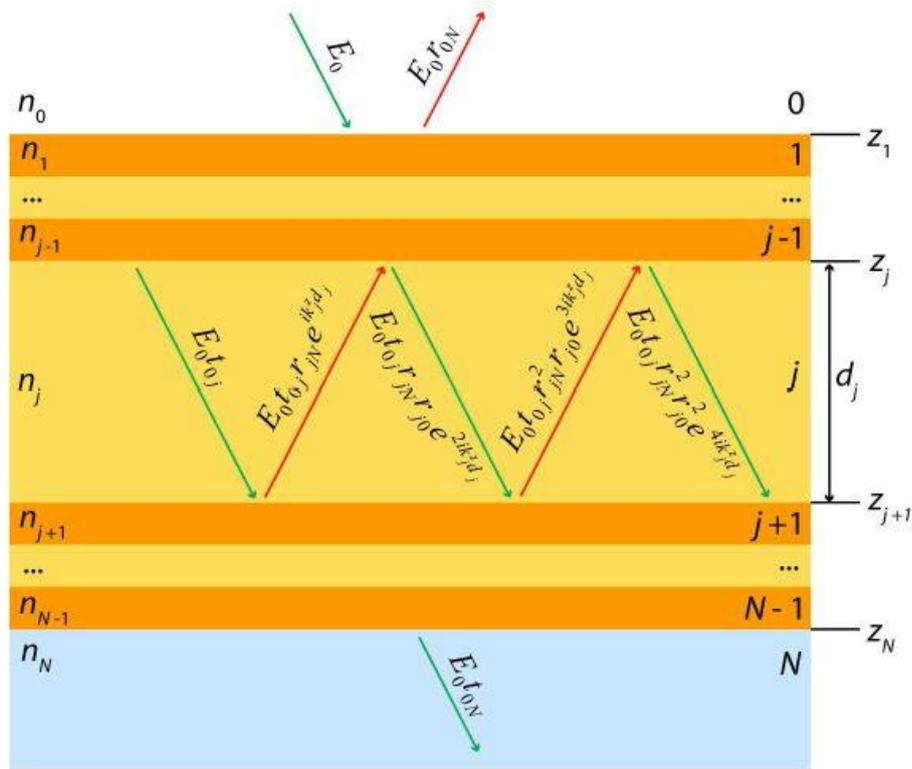
Figure 20: Sketch of the electromagnetic waves propagating in positive (green arrows) and negative (red arrows) z-directions in a stratified system of homogeneous slabs that is illuminated with the incident wave E_0. From [52].

The component of the wave vectors perpendicular to the interface, k^z_j, in each medium depend on q_z and on the refractive indices n_j of the media, and thus on the electron densities, $\rho_{el,j}$, as explained in section 3.1.

$$k^z_j = \frac{2\pi}{\lambda} \sqrt{\left(\frac{q_z\lambda}{4\pi}\right)^2 - n^2_j - 1}$$

In each medium j, the vertical intensity profile is the absolute square of the sum of the electromagnetic waves E_+ and E_-, propagating in positive and negative z directions, respectively.

$$I_{q_z}^{illu}(z) = \left| E_+(q_z, z) + E_-(q_z, z) \right|^2$$

In the first medium (j=0):

$$E_+^0(q_z, z) = E_0 e^{ik_0^z(z-z_1)}$$

$$E_-^0(q_z, z) = E_0 r_{0,N} e^{ik_0^z(z_1-z)}$$

$$I_{q_z}^{illu}(z < z_1) = \left| E_0(e^{ik_0^z(z-z_1)} + r_{0,N} e^{ik_0^z(z_1-z)}) \right|^2$$

$E_+^0(q_z, z)$ coincides with the amplitude of the incident wave, while $E_-^0(q_z, z)$ represents the amplitude of the wave reflected by the layered system and $r_{0,N}$ denotes the Parratt amplitude reflection coefficient (see section 3.1) for a beam traveling from medium 0 to medium N.

In the last medium (j=N):

$$E_+^N(q_z, z) = E_0 t_{0,N} e^{ik_N^z(z-z_N)}$$

$$E_-^N(q_z, z) = 0$$

$$I_{q_z}^{illu}(z \geq z_N) = \left| E_0 t_{0,N} e^{ik_N^z(z-z_N)} \right|^2$$

$E_+^N(q_z, z)$ represents the amplitude of the wave transmitted through the entire layered system and $t_{0,N}$ denotes the Parratt amplitude transmission coefficient for a beam traveling from medium 0 to medium N. $E_-^N(q_z, z)$ vanishes, as there is no more reflected wave in the last medium.

For the intermediate media, multiple reflections have to be considered, as illustrated in figure 11. This requires an infinite summation to obtain $E_+^j(q_z, z)$ and $E_-^j(q_z, z)$:

$$E_+^j(q_z, z) = E_0 \left(t_{0,j} + t_{0,j} r_{j,N} r_{j,0} e^{2ik_j^z d_j} + t_{0,j} r_{j,N}^2 r_{j,0}^2 e^{4ik_j^z d_j} + \cdots \right) e^{ik_j^z(z-z_j)}$$

$$= E_0 t_{0,j} \left(1 + r_{j,N} r_{j,0} e^{2ik_j^z d_j} + (r_{j,N} r_{j,0} e^{2ik_j^z d_j})^2 + \cdots \right) e^{ik_j^z(z-z_j)}$$

$$= E_0 t_{0,j} e^{ik_j^z(z-z_j)} \sum_{l=0}^{\infty} (r_{j,N} r_{j,0} e^{2ik_j^z d_j})^l = \frac{t_{0,j}}{1 - r_{j,N} r_{j,0} e^{2ik_j^z d_j}} E_0 e^{ik_j^z(z-z_j)}$$

And similarly:

$$E_-^j(q_z, z) = E_0 \left(t_{0,j} r_{j,N} e^{ik_j^z d_j} + t_{0,j} r_{j,N}^2 r_{j,0} e^{3ik_j^z d_j} + t_{0,j} r_{j,N}^3 r_{j,0}^2 e^{5ik_j^z d_j} \ldots \right) e^{ik_j^z(z_{j+1}-z)}$$

$$= \frac{t_{0,j} r_{j,N} e^{ik_j^z d_j}}{1 - r_{j,N} r_{j,0} e^{2ik_j^z d_j}} E_0 e^{ik_j^z(z_{j+1}-z)}$$

Finally:

$$I_{q_z}^{illu}(z_j \leq z \leq z_{j+1}) = \left| \frac{t_{0,j}}{1 - r_{j,N} r_{j,0} e^{2ik_j^z d_j}} \left(e^{ik_j^z(z-z_j)} + r_{j,N} e^{ik_j^z d_j} e^{ik_j^z(z_{j+1}-z)} \right) E_0 \right|^2$$

$d_j = z_{j+1} - z_j$ denotes the thickness of the jth medium and $r_{x,y}$ and $t_{x,y}$ the Parratt amplitude reflection and transmission coefficients for a beam traveling from medium x to medium y. This means that an N x N matrix of Parratt coefficients needs to be calculated before calculating an illumination intensity profile. For a beam traveling in positive z-direction the commonly used recursion formula for the reflection coefficients can be used, together with the corresponding formulae for the transmission coefficients [54].

$$r_{j,N} = \frac{r_{j,j+1}^F + r_{j+1,N} \cdot e^{2ik_{j+1}^z d_{j+1}}}{1 + r_{j,j+1}^F r_{j+1,N} \cdot e^{2ik_{j+1}^z d_{j+1}}}, r_{N-1,N} = r_{N-1,N}^F$$

$$t_{j,N} = \frac{t_{j,j+1}^F \cdot t_{j+1,N} \cdot e^{ik_{j+1}^z d_{j+1}}}{1 + r_{j,j+1}^F \cdot r_{j+1,N} \cdot e^{2ik_{j+1}^z d_{j+1}}}, t_{N-1,N} = t_{N-1,N}^F$$

For a beam traveling in negative z-direction the inverse problem has to be solved:

$$r_{j,0} = \frac{r_{j,j-1}^F + r_{j-1,0} \cdot e^{2ik_{j-1}^z d_{j-1}}}{1 + r_{j,j-1}^F r_{j-1,0} \cdot e^{2ik_{j-1}^z d_{j-1}}}, r_{1,0} = r_{1,0}^F$$

$$t_{j,N} = \frac{t_{j,j-1}^F \cdot t_{j-1,0} \cdot e^{ik_{j-1}^z d_{j-1}}}{1 + r_{j,j-1}^F \cdot r_{j-1,0} \cdot e^{2ik_{j-1}^z d_{j-1}}}, t_{1,0} = t_{1,0}^F$$

3.4 Polymer Brushes

This thesis deals with the structural characterization of interacting polymer brushes, both biological (LPSs from bacterial surfaces) and synthetic (PEG). To model data, suitable theoretical models for the conformation of polymer brushes and for the interaction between two opposing brushes are needed. Several theoretical models are provided in the framework

of various brush theories. Here, a brief introduction into important brush theries is given, based on the review article by Milner [69] .

Polymer brushes are long-chain polymer molecules attached by one end to a surface or interface by some means, with a density of attachment points high enough so that the chains stretch away from the interface (Figure 11). This situation is very different from the behavior of polymers in a solution, where chains adopt random-walk configurations.
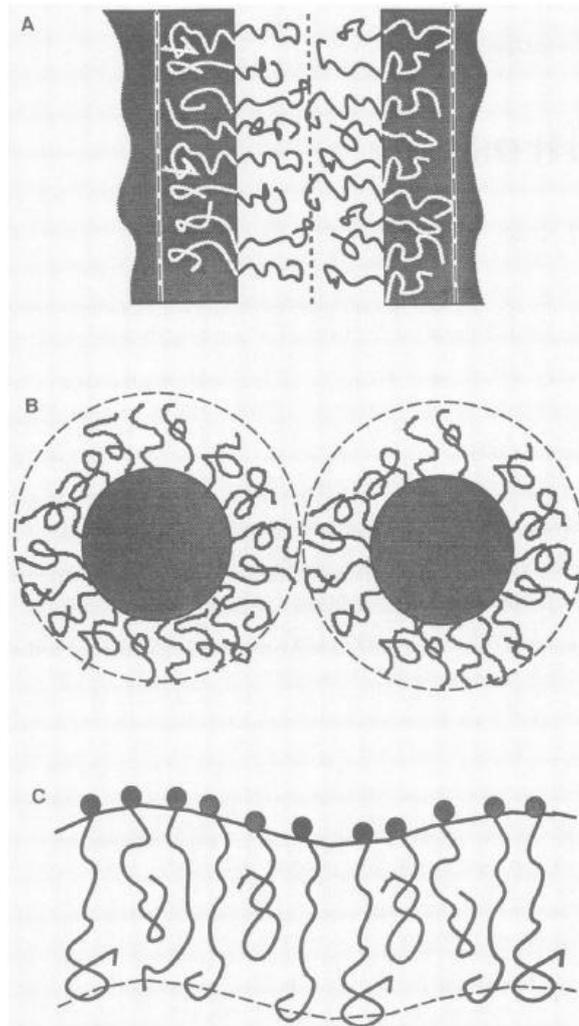

Figure 31: Cartoons of three physical situations in which polymer brushes are present. Extracted from [69]. A) Diblock copolymers forming a lamellar microphase. B) Colloidal particles stabilized in suspension by polymer brushes of end-grafted soluble polymer chains. C) Polymeric surfactant molecules adsorbed on a liquid-liquid, liquid-vapor or liquid-solid interface.

3.4.1 Alexander-de Gennes model for polymer brushes

The conformation of polymer brushes can be understood by free-energy-balance arguments. Consider the case of polymer chains of length N (measured in units of the persistence or Kuhn length a) attached at a grafting density of σ chains per unit area to a flat interface and exposed to a solvent. The polymer chains have two opposite tendencies. First, they adopt random-walk configurations to maximize their configurational entropy (this leads to short and dense brushes). Second, they prefer to be in contact with solvent molecules (which favors tall sparse brushes). If the distance (given by $\sigma^{-1/2}$) between grafting sites is much smaller than its radius of gyration, $R_g = N^{1/2}a$, both tendencies cannot be met. The height h of the polymer brush will be dictated by a balance between these two free energy costs. Chains overlap with their neighboring chains, thus reducing the energetically favorable contact with solvent molecules, and they stretch, reducing the configurational entropy.

The simplest estimate of this free energy balance achieved by polymer brushes is the so-called Flory [70] argument, first presented by Alexander [71] and de Gennes [72, 73]. This argument estimates the reduction in configurational entropy from results for an ideal random walk constrained to travel a distance h from the grafting surface to the outer edge of the brush. More physically, the polymer chains of length N can be thought of as entropic "springs" with spring constant k_BT/R_g^2 (that is, it costs k_BT to double the typical end-end separation) stretched from the grafting surface to the outer edge of the brush. The cost of unfavorable contacts between chains is estimated by assuming that the chain units are randomly distributed with a uniform density equal to the average density in the brush, $\phi \sim N\sigma/h$. This leads to a free-energy cost per chain

$$\Delta f \sim k_B T \left[\frac{3h^2}{2Na^2} + wN\left(\frac{N\sigma}{h}\right) \right] \qquad (1)$$

in which w is the excluded volume parameter, which measures the strength of the repulsion between chain units. If minimized with respect to the brush height, h

$$h \sim N(w\sigma a^2)^{1/3} , f \sim k_B TN(w\sigma a^{-1})^{2/3} \qquad (2)$$

This result implies that in a sequence of brushes with the same coverage σ and increasingly large N, the height h grows linearly with N, while the unstretched chain dimension R_g only grows as $N^{1/2}$. For long polymer chains, h is much larger than R_g (meaning that the chains are

strongly stretched). According to this, the properties of a polymer chain grafted to a surface will be quite different from that of polymer chains in solution.

3.4.2 Self Consistent Field Theory

The previously presented free-energy-balance argument [71-73] only estimates the energetic balance between stretching and chain-chain contact, but it gives no information about the conformation of the polymer chains or about the brush volume fraction distribution, ɸ(z), at a distance z from the grafting surface.

The Flory argument leads to a brush in which its end points are all at the same distance from the grafting surface, which means that the volume fraction distribution is a step-function. This implies that all the chains behave exactly the same, with no possibility for a chain to deviate from its most likely path. This requirement of all of the chain ends residing at the outer edge of the brush does not result in the optimum state. It could be the case that a polymer chain could bend backwards towards the grafting surface lowering its stretching free energy without suffering more contacts with chain units. For the chains to be stretched away from the interface in a stable and self-consistent way, the osmotic pressure Π(z) of a chain, this is, the cost to place a chain unit at a distance z from the interface, must decrease as z increases. For brushes with solvent, like the ones presented in this thesis, the cost of adding a chain unit is the likelihood of contact with another chain, so Π(z) α ɸ(z).

If it is assumed that the end points of the polymer chains can be located at any distance from the grafting surface, we can obtain the shape of Π(z). [This approach was developed for brushes with solvent by Milner, Witten, and Cates [74] and independently by Skvortsov, Zhulina, Priamitsyn, and collaborators [75, 76]. The equation that gives the most favorable configuration of a chain in a potential Π(z), is found by minimizing the sum of *local* stretching and repulsion free-energy terms (analogous to the global Flory estimate) with respect to the configuration Z(s) of a chain (only the distance Z(s) of chain unit s from the interface is relevant):

$$0 = \frac{\delta F[Z(s)]}{Z(s)} = \frac{\delta}{\delta Z(s)} \int ds [\frac{3}{2a^2} \left(\frac{\delta Z}{\delta s}\right)^2 + \Pi[Z(s)]] = -\frac{3}{a^2} \frac{\delta^2 Z}{\delta s^2} + \frac{\delta \Pi}{\delta Z} \quad (4)$$

This equation looks like the trajectory of motion of a particle with trajectory Z(s) falling in a potential -Π(z). The chain length N is analogous to the time of flight of the particle. For

chains to be in equilibrium with free ends at any distance from the interface, then the potential μ must be such that any starting point (free end position) gives the same time of flight (length of chain to the interface). That potential is a parabola, the potential of the harmonic oscillator

$$\Pi(z) = constant - \frac{\pi^2}{8N^2} z^2 \qquad (5)$$

Figure 12 shows volume fraction distributions, ϕ(z), for the AdG brush and the self-consistent field brush.
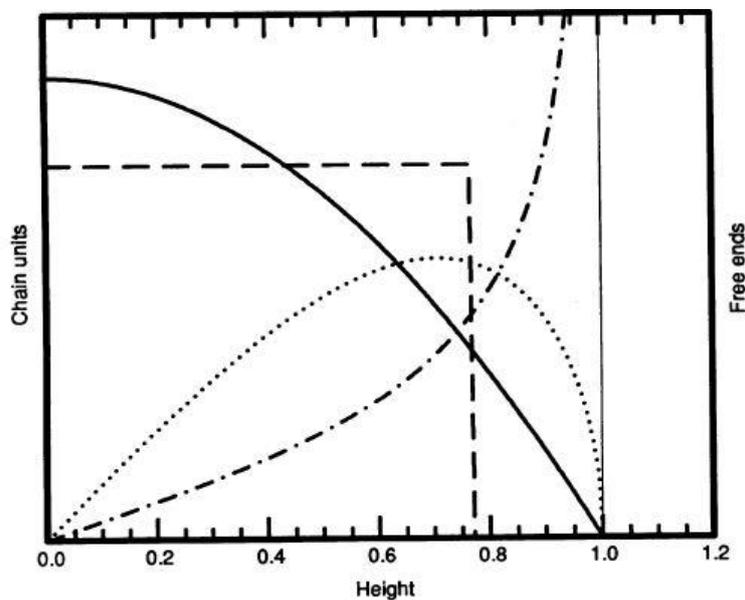
Figure 12: Chain-unit density profiles Φ(z) for a "parabolic" brush (that is, Φ<<1 so μ α Φ), and the step-function ansatz at equal coverage σ and chain length N. Also shown are end-density profiles for brushes with (dotted) and without (dot-dashed) solvent. From [69].

3.4.3 Pressure-Distance relations

The repulsive forces from compressed brushes have been described with both the scaling (Alexander-deGennes) and self-consistent-field theories. In the scaling scheme, it is supposed that the monomer concentration is constant throughout a polymer layer with thickness L. Alexander [77] and de Gennes [78] considered the physical response of the

polymer when two apposed brush-covered surfaces are brought into contact. The pressure depends on the distance between surfaces (h) as:

$$\Pi_{AdG}(h) = \left(\frac{k_B T}{D^3}\right)\left(\left(\frac{2L}{h}\right)^{\frac{9}{4}} - \left(\frac{h}{2L}\right)^{\frac{3}{4}}\right)$$

Here, $L = Na\left(\frac{a}{D}\right)^{2/3}$, N is the number of monomers, a is the length of a monomer and D the distance between grafting points. The first term is repulsive and represents the osmotic pressure, while the second term is attractive and arises from the elastic restoring force.

The self-consistent field theory by Milner *et al.* [74] takes into account the possibility that the individual polymer chains may not be uniformly distributed, so that the monomer concentration varies throughout the polymer layer. The concentration profile of this brush is parabolic, as shown in the previous section, and, as a result, the mean-field brush is "softer" upon compression than predicted by scaling arguments. However, these mean-field arguments give pressure relationships with exponents close to the ones obtained by Alexander and deGennes, therefore predicting a force law rather similar to theirs.

The self-consistent field theory represents the repulsive pressure as

$$\Pi_{SCF}(h) = P_0 \left(\frac{L_0}{\left(\frac{h}{2}\right)^2} - \frac{h}{L_0^2} + \frac{\left(\frac{h}{2}\right)^4}{L_0^5}\right)$$

where $\Pi_0 = (K_b TN/2)\left(\frac{\pi^2}{12}\right)^{\frac{1}{3}}(a^{\frac{4}{3}}/D^{\frac{10}{3}})$ and $L_0 = \left(\frac{12}{\pi^2}\right)^{\frac{1}{3}} N(a^{\frac{5}{3}}/D^{\frac{2}{3}})$

Pressure-distance relations for brushes of different height and grafting density are presented in Figure 13.

Figure 13: (A) Measured pressure-distance data for interacting PEG brushes -composed by mixtures of DSPC and PEG-lipids at a PEG-lipid mol fraction of 10 mol%- (black dots) compared with theoretical predictions for de Gennes brushes (dotted line) and Milner brushes (dashed line). The solid line is the theoretical prediction for polydisperse brush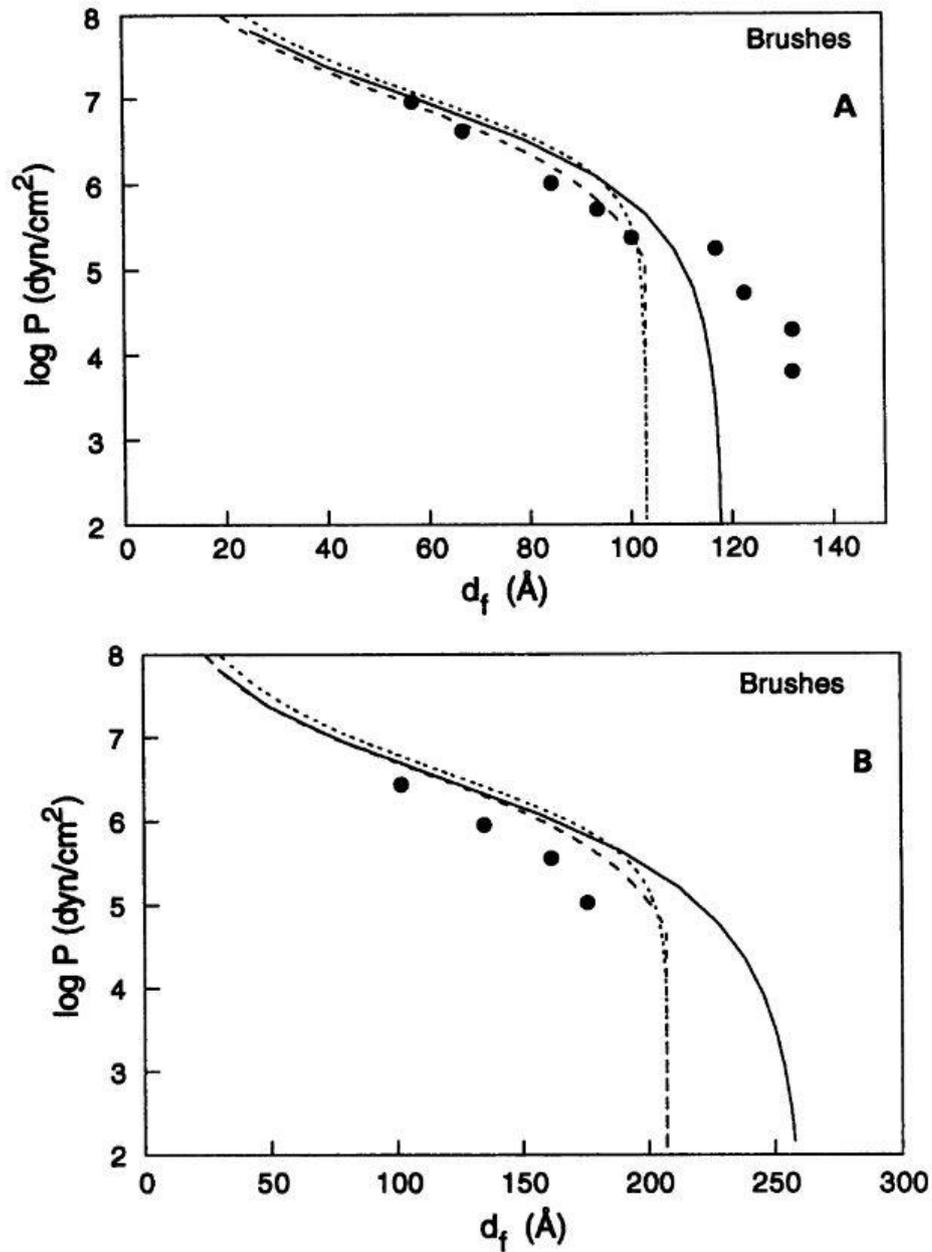es. (B) Measured pressure- distance data for interacting PEG brushes -composed by mixtures of DSPC and PEG-lipids at a PEG-lipid mol fraction of 5 mol%- (black dots) compared with theoretical predictions for de Gennes brushes (dotted line) and Milner brushes (dashed line). The solid line is the theoretical prediction for polydisperse brushes. Image from Parsegian *et al.* [16].

4. Reprints

Manuscript 1. Neutron Reflectometry Yields Distance-Dependent Structures of Nanometric Polymer Brushes Interacting across Water

Ignacio Rodriguez-Loureiro[a], Ernesto Scoppola[a], Luca Bertinetti[a], Aurelio Barbetta[a,b], Giovanna Fragneto[c], and Emanuel Schneck[a,*]

[a]Max Planck Institute of Colloids and Interfaces, Am Mühlenberg 1, 14476 Potsdam, Germany

[b]Institut de Chimie Séparative de Marcoule, 30207 Bagnols sur Cèze, France

[c]Institut Laue-Langevin, 71 avenue des Martyrs, 38000 Grenoble, France

[*]Corresponding author: schneck@mpikg.mpg.de, Phone: +49-331567-9404, Fax: +49-331567-9402

Abstract

The interaction between surfaces displaying end-grafted hydrophilic polymer brushes plays important roles in biology and in many wet-technological applications. In this context, the conformation of the brushes upon their mutual approach is crucial, because it affects interaction forces and the brushes' shear-tribological properties. While this aspect has been addressed by theory, experimental data on polymer conformations under confinement are difficult to obtain. Here, we study interacting planar brushes of hydrophilic polymers with defined length and grafting density. Via ellipsometry and neutron reflectometry we obtain pressure-distance curves and determine distance-dependent polymer conformations in terms of brush compression and reciprocative interpenetration. While the pressure-distance curves are satisfactorily described by the Alexander-de-Gennes model, the pronounced

brush interpenetration as seen by neutron reflectometry motivates detailed simulation-based studies capable of treating brush interpenetration on a quantitative level.

1. Introduction

Nanometric brushes of end-grafted polymers are widely used in wet- and biotechnology. Applications include the biocompatible functionalization of nanoparticles and material surfaces[27], the stabilization of colloidal suspensions[28] and foams[29], as well as shear lubrication[11]. In most cases the forces between two interacting brushes are responsible for their function, where the forces both perpendicular[28, 29] or parallel[11] to the brush-grafting surfaces can play the principal role. Both are relevant also for the saccharide-based polymer brushes found on the surfaces of biological membranes[7, 30], as they affect, for instance, the interaction between adjacent Gram-negative bacteria in biofilms, and in turn biofilm mechanical properties. A pivotal aspect of the interaction of two brushes is the polymer conformation in terms of compression and mutual interpenetration. The latter has immediate consequences for the brushes' shear tribological properties, because shear stress between sliding polymer brushes is known to depend on the level of brush interpenetration[79]. The interaction of polymer brushes has been extensively studied theoretically[15, 77, 78, 80] and computationally[79, 81-83], both in terms of pressure-distance curves (i.e., distance-dependent interaction pressures) and in terms of brush conformations. Pressure-distance curves have been determined also experimentally, using amphiphilic multilayers[16], surface force apparatus (SFA)[84] and atomic force microscopy (AFM)[85]. In contrast, experimental data on the conformation of interacting brushes has remained sparse[25, 86], despite its great technological and biological importance.

Insight into structures "buried" between two surfaces or interfaces, such as the conformation of polymer brushes under confinement, is generally difficult to obtain experimentally. At first, neither of the two surfaces is accessible by scanning near-field techniques like AFM, because this is prevented by the presence of the respective counterpart. Secondly, the relevant structures are of the order of 0.1 - 100 nm; these small length scales cannot be resolved by optical microscopy and at the same time impede the use of fluorescent labels, therefore excluding complementary techniques like fluorescence resonance energy transfer (FRET). Finally, the structural features of interest are easily

perturbed and sensitive to thermodynamic conditions, rendering all cryo-based techniques inadequate. X-ray and neutron scattering are among the very few techniques that can probe such structures with the required sub-nanometer spatial resolution. They can be used in a wide pressure and temperature range and provide sample-averaged structural information. Neutron scattering, apart from being truly non-destructive, has the unique advantage of contrast variation: Chemical components of interest can be highlighted by selective deuteration (i.e., replacing hydrogen with deuterium) without changing their chemistry[87]. Specular neutron reflectometry (NR) with contrast variation unambiguously reveals matter density profiles perpendicular to an interface[17, 18], but requires macroscopically-large planar samples with near-perfect flatness and very low surface roughness. While the fabrication of single surfaces meeting these requirements is well established to date, bringing two such surfaces into a defined interaction distance over large areas has remained a challenging task. In their pioneering studies, Kuhl and co-workers carried out NR measurements while keeping two brush-decorated solid substrates parallel at separations down to below 100 nm[25]. Using this approach, they determined the density profiles of comparatively thick polystyrene (PS) brushes interacting across toluene for two grafting surface separations. Later, in order to unambiguously determine the degree of brush interpenetration, one of the PS brushes was deuterated (dPS) while the other one was hydrogenated (hPS)[86].

Here, we study the interaction of hydrophilic polymer brushes across aqueous media. For this purpose, we make use of an architecture in which two planar amphiphilic monolayers act as grafting surfaces for the polymer brushes and are brought into contact at distances as small as few tens of nm and less. These are the typical length scales relevant for the interaction of polymer brushes on biological surfaces[7, 30] and of polymer-decorated nanoparticles in biotechnology[31]. Via controlled dehydration our double-monolayer configuration enables the tunable approach of the two surfaces and the separation-dependent structural investigation[88]. The monolayers are composed of lipids and lipopolymers (Fig. 1A), supported by a hydrophobized planar solid on one side, but free-standing on the other side (Fig. 1 B and C). With that, a homogeneous surface separation on the planar substrate is readily realized, in contrast to approaches involving two planar solids, where creation of a defined interaction distance is generally difficult[19]. We use ellipsometry to obtain the pressure-distance curves of interacting brushes of various

polymerization degrees and grafting densities. For selected brushes, we use NR to determine the brush conformation as a function of the grafting surface separation. To this end we describe the reflectivity curves in a wide separation range with a common model based on the volume fraction distributions of all chemical components and their distance dependence. We find that the pressure-distance curves are surprisingly well described by the Alexander-de-Gennes (AdG) model[77, 78]. In contrast, NR reveals pronounced brush interpenetration captured only by the most rigorous simulation-based theoretical descriptions of interacting polymer brushes.
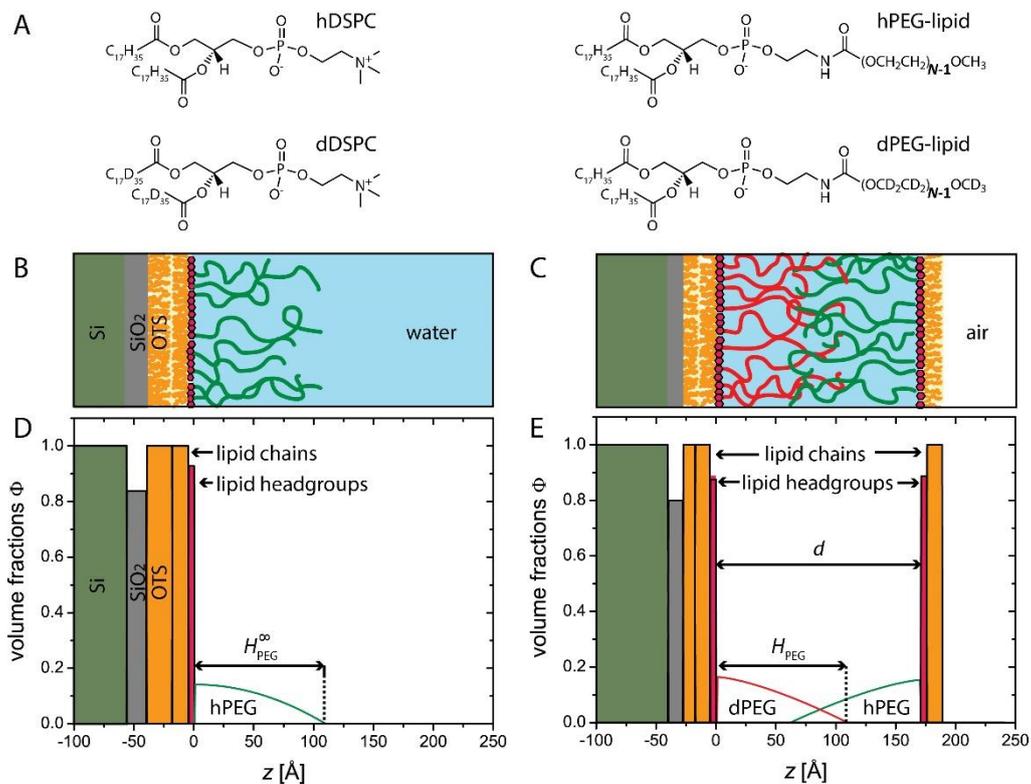
Figure 1: (A) Chemical structures of the amphiphilic molecules DSPC (1,2-distearoyl-sn-glycero-3-phosphocholine) and PEG-lipid (1,2-distearoyl-sn-glycero-3-phosphoethanolamine-*N*-[methoxy(polyethylene glycol)]). Hydrogenous and chain-deuterated versions of DSPC are denoted as hDSPC and dDSPC, respectively. PEG-lipid versions with hydrogenous and deuterated PEG chains are denoted as hPEG-lipid and dPEG-lipid. (B) Schematic illustration of a single uncompressed lipid-anchored brush in water. (C) Schematic illustration of a double-monolayer architecture with two interacting lipid-anchored PEG brushes. Distal lipid chains and the proximal PEG brush are deuterated while the proximal lipid chains and the distal PEG brush are hydrogenous. The solid surface is hydrophobically functionalized with

octadecyltrichlorosilane (OTS). (D and E) Simplified representations of the spatial distributions of all components (Si, SiO_2, OTS, lipid chains, lipid headgroups, and PEG) in panels B and C, respectively.

2. Materials and Methods

2.1. Materials and Sample Preparation

Unless stated otherwise, all chemicals were purchased from Sigma (St. Louis, MO, USA) and used without further purification. D_2O (99%) was purchased from Euriso-Top, Saint-Aubin, France. PEG brushes -either in hydrogenous form (hPEG) or fully deuterated (dPEG)- were prepared from mixtures of two lipids, whose chemical structures are shown in Fig. 1A: (i) distearoyl-*sn*-glycero-3-phosphoethanolamine lipids with a PEG chain comprising $22 \leq N \leq 114$ monomers attached to the hydrophilic headgroup (hPEG-lipid or dPEG-lipid); (ii) 1,2-distearoyl-*sn*-glycero-3-phosphocholine (DSPC), either in hydrogenous form (hDSPC) or with fully deuterated alkyl chains (dDSPC). DSPC and PEG-lipid were purchased from Avanti Polar Lipids (Alabaster, AL, USA). Silicon single (111) crystal blocks of 50 mm x 50 mm x 10 mm or 50 mm x 40 mm x 10 mm size, polished on one large face, were purchased from Synchrotronix (Annemasse, France). The polished surface was covered with a thin layer of native amorphous silicon oxide (SiO2). Silicon wafers (150 mm diameter, 625 µm thickness) of which the polished surface was covered with a 105 nm layer of thermal silicon oxide were purchased from SIEGERT Wafer GmbH (Aachen, Germany) and cut into rectangular pieces of 20 mm x 10 mm. Silicon blocks and pieces were cleaned by washing with organic solvents (chloroform, acetone, and ethanol) and UV-ozone treatment. They were then rendered hydrophobic via covalent functionalization with octadecyltrichlorosilane (OTS) by immersion in freshly prepared solutions of OTS in hexadecane at a concentration of 1 mM for 1 h and subsequent rinsing in hexadecane and ethanol. Lipid monolayers anchoring the PEG brushes were deposited onto the functionalized substrates utilizing a combination of the Langmuir-Schaefer (LS) and Langmuir-Blodgett (LB) techniques[89]. For this purpose, mixtures of DSPC (either hDSPC or dDSPC) and PEG-lipid (either hPEG-lipid or dPEG-lipid), with PEG-lipid mole fractions f ranging from 0% to 10%, in chloroform at 2 mg/ml overall concentration were prepared and spread at the air-water interface in a Teflon Langmuir trough (Nima Technology, Coventry, UK) containing H2O. After compression to a lateral pressure of

Π_{lat} = 35 mN/m, a first monolayer was transferred onto the hydrophobic OTS by LS, i.e., with the solid surface facing the water surface. This procedure results in single uncompressed brushes exposed to bulk water (see Fig. 1B). No significant change in Π_{lat} upon substrate/monolayer contact was observed, evidencing a transfer ratio close to 100 %, which is typical for the LS technique. Selected samples were characterized by NR already at this stage, in order determine their structure (see Results section). In all other cases, the Si block was then rotated under water by 90°, so that its surface ended up perpendicular to the water surface. The remaining lipid monolayer at the air/water interface were then removed and replaced with a fresh monolayer compressed to Π_{lat} = 35 mN/m. This second monolayer was then transferred by LB, i.e., by pulling the block upwards. As a result, the PEG brushes anchored to the monolayers face each other as schematically illustrated in Fig. 1C. With this combination of LS and LB highly structured sample architectures were achieved (see Results section). Alternative sample preparations by the commonly used double LB deposition were less successful (see Supplementary Information).

2.2. Determination of Pressure-Distance curves by Ellipsometry

Ellipsometry enables the characterization of interfacial layers in terms of refractive indices and thicknesses. The method is based on the change in the polarization state of light upon reflection from the surface. For a given refractive index n, the change depends on the layer thickness and is quantified in terms of the phase difference Δ and the amplitude ratio Ψ encoded in the ratio between the complex reflection coefficients R_s and R_p for s and p polarizations, respectively[90]:

$$R_p/R_S = tan\, \Psi\, e^{-i\Delta} \tag{1}$$

For ellipsometry measurements, silicon chips with thermal oxide were used as substrates for the double monolayers. Silicon has the complex refractive index n_{Si} = 3.885 - 0.018i[91]. Measurements were performed by scanning the incident angle α_i from 63° to 75°, with an Optrel Multiskop ellipsometer working with a wavelength λ_{elli} = 632.8 nm. The best fit to the results on bare substrates yielded a SiO_2 refractive index of n_{SiO2} = 1.468, close to the literature value[92] and an oxide layer thickness of 105.5 nm. In the next step, the measurement values obtained for fully dehydrated samples (h_{rel} < 5 %, achieved by streaming with N_2) were modeled while accounting for the above-defined oxide layer

properties, to obtain the thickness D_{org} of the dry organic layer jointly formed by OTS and the two brush-decorated lipid monolayers. In this procedure, the best fit was obtained with a refractive index $n_{org} = 1.5$, consistent with earlier reports on organic materials[93-95]. Fig. 2 shows the two ellipsometric angles, Δ and Ψ, as functions of α_i for various dry samples. The solid lines indicate simultaneous fits to both ellipsometric angles and correspond to organic layer thicknesses of $D_{org} = 2.1$ nm, $D_{org} = 7.4$ nm, $D_{org} = 8.6$ nm, and $D_{org} = 10.7$ nm for bare OTS, for OTS with interacting DSPC monolayers ($f = 0\%$), and for OTS with interacting DSPC monolayers displaying brushes with $f = 10\%$ and $N = 45$ or $N = 114$, respectively. This systematic increase is remarkably proportional to the material amount that is added according to the double-monolayer architecture (see supporting material).
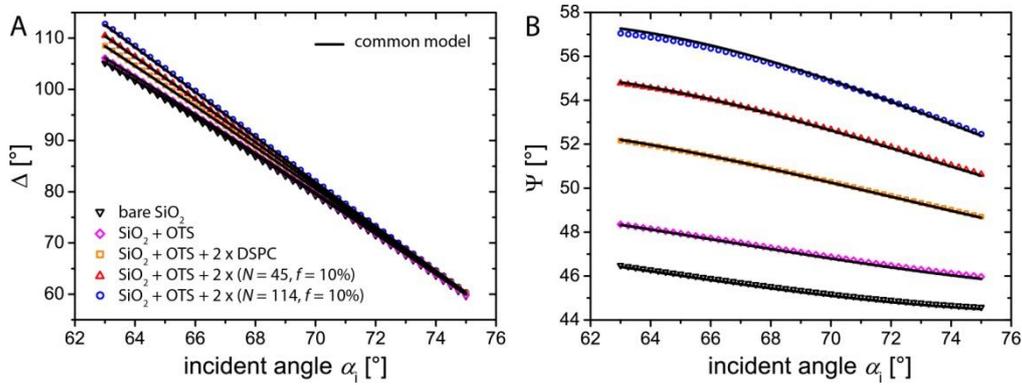
Figure 2: Ellipsometric angles Δ (A) and Ψ (B) as functions of the incident angle α_i for various samples under fully dehydrated conditions: (i) bare SiO_2, (ii) SiO_2 with OTS, (iii) SiO_2 with OTS and interacting DSPC monolayers, and (iv) SiO_2 with OTS and interacting DSPC monolayers displaying brushes with $f = 10\%$ and $N = 45$ or $N = 114$. Statistical errors are smaller than the symbol size. Solid lines indicate the bets-matching combined fits to Δ and Ψ for each sample.

In the last step, the ellipsometric angles obtained at controlled humidity h_{rel} were modeled while accounting for the known optical parameters of oxide and dry organic layers. The humidity-dependent equivalent thickness (see Eq. 5 below) of the water layer, $D_w(h_{rel})$, was then determined assuming $n_w = 1.33$ for the refractive index of water. As shown in the supporting material, the position of the water layer with respect to the organic layer in the model has negligible influence on the results. This is because in the thin-film limit ellipsometry is merely sensitive to the overall optical path. In order to instantly follow the

evolution of h_{rel}, these measurements were performed at a fixed incident angle of $\alpha_i = 70°$. Note that measurements at a single incident angle are sufficient to determine the incremental change of a layer thickness when this is the only unknown parameter. Humidity was controlled by placing the samples inside a closed chamber through which humidified N_2 was streamed. The gas was humidified by letting it pass through a temperature-controlled water bath in the form of mm-sized bubbles. High humidities were realized by elevating the water temperature to close to or even slightly above the sample temperature. Low humidities were realized either by lowering the bath temperature or by mixing the humidified N_2 stream with dry N_2. The humidity at the sample position was measured with a calibrated humidity sensor (Sensirion SHT75, measurement uncertainty $\Delta h_{rel} = \pm 2\%$), placed close to the sample surface.

2.3. Structural Investigation by Neutron Reflectometry

2.3.1: Setup and Experiments

Neutron reflectometry (NR) measurements were performed on the D17 time-of-flight (TOF) reflectometer at the Institut Laue-Langevin (ILL, Grenoble, France). The intensity of the reflected neutron beam relative to the intensity of the incident beam was recorded as a function of the component of the scattering vector normal to the interface, $q_z = (4\pi/\lambda)\sin\theta_i$, where λ is the neutron wavelength and θ_i the incident angle. Measurements were carried out at two fixed angles of incidence, $\theta_i = 0.8$ deg and $\theta_i = 3.2$ deg using a wavelength range of $2 \text{ Å} < \lambda < 22 \text{ Å}$. The relative resolution in q_z, $\Delta q_z/q_z$, defined via the *full width at half maximum* (FWHM) was q_z-dependent and varied in the range $2\% < \Delta q_z/q_z < 14\%$. While modeling experimental reflectivity curves the finite experimental resolution was taken into account by convoluting the initial reflectivity curves, calculated for the case of infinite resolution, with Gaussian functions representing the resolution function of the experiments. The reflectivity curves displaying the reflected intensity as a function of q_z (see Figs. 3A and 5A) depend on the depth profile of the neutron scattering length density (SLD) ρ across the interface between the two bulk media, Si on one side and water or humidified air, respectively, on the other side. The SLD of a homogeneous medium depends on the density n_i/v of the constituting nuclides and on their coherent scattering lengths b_i:

$$\rho = \sum_i \frac{n_i}{v} b_i, \text{ where } n_i \text{ is the number of nuclides } i \text{ in a volume } v. \tag{2}$$

Single uncompressed brushes exposed to bulk water (see Fig. 1B) were characterized in several contrast fluids obtained by mixing H_2O and D_2O at defined mixing ratios leading to distinct SLDs. H_2O and D_2O have SLDs of ρ_w = -0.56 x 10^{-6} Å^{-2} and ρ_w = 6.36 x 10^{-6} Å^{-2}, respectively. In addition, we used H_2O/D_2O mixtures having ρ_w = 4.0 x 10^{-6} Å^{-2} (4MW) and with ρ_w = 2.07 x 10^{-6} Å^{-2}, the latter known as *silicon-matched water* or SMW since its SLD matches that of the silicon substrate. For interacting brushes (see Fig. 1C) the relative humidity was H_2O-based and was varied using the newest generation humidity cells of D17 using Peltier elements to warm up the sample and a water reservoir thermally isolated from the sample, and a temperature-controlled water bath to cool down. High humidities were realized by elevating the water temperature to close to or even slightly above the sample temperature. Reflectivity curves were measured in loops of 5 min acquisitions, to capture also conditions of extremely high humidity which are difficult to maintain over longer periods[96, 97].

2.3.2: Reflectivity Data Analysis

The reflectivity data were analyzed in the spirit of our recent work on polymer brushes in contact with protein solutions[98, 99]: The samples are described by common models accounting for all measurement conditions. For a single uncompressed brush in water (see Fig. 1B) the corresponding model comprises measurements in all contrast fluids. For interacting brushes subject to controlled dehydration (see Fig. 1C), the corresponding model accounts for all hydration levels characterized by their respective grafting surface separations *d*. Each model describes the volume fractions Φ_i of all compounds, i.e., silicon (*i* = "Si"), silicon oxide (*i* = "SiO2"), OTS (*i* = "OTS"), lipid chains (*i* = "CH"), lipid headgroups (*i* = "HG"), PEG (*i* = "PEG"), and water (*i* = "W") as functions of the depth coordinate *z*. It incorporates several adjustable parameters that are fitted simultaneously to the results obtained under different conditions. Simplified schematic illustrations of single and interacting brushes are presented in Fig. 1 D and E.

The SLD profile for a single uncompressed brush is given by:

$$\rho(z) = \Phi_{Si}(z)\rho_{Si} + \Phi_{SiO2}(z)\rho_{SiO2} + \Phi_{OTS}(z)\rho_{OTS} + \Phi_{CH}(z)\rho_{CH} + \Phi_{HG}(z)\rho_{HG} + \Phi_{PEG}(z)\rho_{PEG} + \Phi_w(z)\rho_w, \quad (3)$$

where *z* denotes the distance measured along the normal to the planar sample surface. The brush grafting surface on the solid substrate is at *z* = 0 and coincides with the interface

between lipid headgroups and the aqueous region (Fig. 1D). When a second brush is deposited on top of the first one then the second grafting surface is located at $z = d$ (Fig. 1D). Selective deuteration of lipid chains and PEG portions (Fig. 1A) further allows distinguishing between proximal and distal chain and PEG distributions (i = "CH,P", i = "CH,D", i = "PEG,P", and i = "PEG,D", respectively), leading to the following description of the SLD profile for two interacting brushes:

$$\rho(z) = \Phi_{Si}(z)\rho_{Si} + \Phi_{SiO2}(z)\rho_{SiO2} + \Phi_{OTS}(z)\rho_{OTS} + \left(\Phi_{HG,P}(z) + \Phi_{HG,D}(z)\right)\rho_{HG} +$$
$$\Phi_{w}(z)\rho_{w}$$
$$+\Phi_{CH,P}(z)\rho_{CH,P} + \Phi_{CH,D}(z)\rho_{CH,D} + \Phi_{PEG,P}(z)\rho_{PEG,P} + \Phi_{PEG,D}(z)\rho_{PEG,D}, \tag{4}$$

where we also distinguish between proximal and distal headgroups (i = "HG,P" and i = "HG,D", respectively), although they have the same SLD. To quantify the amount per area of each component (except the bulk media) it is convenient to introduce the equivalent thickness

$$D_i = \int_{-\infty}^{\infty} \Phi_i(z)dz, \tag{5}$$

which can be viewed as the thickness of an equivalent layer entirely composed of component i. The profiles of Si, SiO$_2$, OTS, and lipid regions (HC chains and headgroups), are treated with a slab model, in which the crystalline silicon substrate is represented by a semi-infinite continuum with fixed scattering length density ρ_{Si} = 2.07 × 10^{-6} Å^{-2}. The SiO$_2$, OTS, lipid chain and lipid headgroup layers are represented as homogeneous slabs with adjustable thicknesses d_{SiO2}, d_{OTS}, d_{CH}, and d_{HG}, respectively (Fig. 1 D and E). To account for interfacial roughness, the profiles of all slabs are modulated by error functions with adjustable roughness parameters ζ_i. The SLD of silicon oxide is fixed at the literature value, ρ_{SiO2} = 3.4 × 10^{-6} Å^{-2}. The water fraction (in the form of hydration layers or silanols) in the SiO$_2$ layer, Φ_w^{SiO2}, is an adjustable parameter. The SLD of OTS is allowed to vary between -0.5 × 10^{-6} Å^{-2} and 0, and the water content in the OTS and lipid chain layers is set to 0, due to their hydrophobic character. To model the lipid layers we use the SLD and volume values reported in Ref [100]: Chains of the proximal lipids are all hydrogenous, so that ρ_{CH} (Eq. 3) and $\rho_{CH,P}$ (Eq. 4) are set to the value for hydrogenous chains, ρ_{hCH} = -0.4 × 10^{-6} Å^{-2} (ref.[100]). In the distal monolayer the fraction of hydrogenous chains (those of dPEG-lipid) is f, while the fraction of deuterated chains (those of dDSPC, with ρ_{dCH} = 7.07 × 10^{-6} Å^{-2}, ref.[100]) is (1 - f). For the distal monolayer, we therefore have $\rho_{CH,D}$ = $f\rho_{hCH}$ + (1 - f)ρ_{dCH} and for f = 10% we

numerically obtain $\rho_{CH,D} = 6.326 \times 10^{-6}$ Å^{-2}. The headgroup SLD was set to $\rho_{HG} = 1.75 \times 10^{-6}$ Å^{-2} [100]. These SLD values are calculated from chain and headgroup volumes of DSPC (and of the DSPE portion of PEG-lipid to good approximation) are $v_{CH} = 980$ Å^3 and $v_{HG} = 344$ Å^3, respectively[100]. The headgroup amount per area in terms of the equivalent thickness is therefore coupled to the corresponding chain equivalent thickness via $D_{HG} = D_{CH}v_{HG}/v_{CH} = 0.35 D_{CH}$. For a given D_{HG}, the water fraction in the headgroup slab then follows as $\Phi_w^{HG} = 1 - d_{HG}/D_{HG}$ (compare Eq. 7 below). In the distal lipid monolayer, all roughnesses (between water/headgroup, headgroup/chain and chain/air) are assumed to be identical and described by a single parameter ζ_D. This approximation is justified when the roughness is dominated by the interfacial fluctuations, which are conformal. The SLDs of the proximal and distal PEG brushes are set to the literature values of hydrogenous PEG ($\rho_{hPEG} = 0.6 \times 10^{-6}$ Å^{-2}, ref. [101]) or deuterated PEG ($\rho_{dPEG} = 7.0 \times 10^{-6}$ Å^{-2}), respectively: $\rho_{PEG} = \rho_{hPEG}$ (in Eq. 3), $\rho_{PEG,D} = \rho_{hPEG}$ (in Eq. 4), and $\rho_{PEG,P} = \rho_{dPEG}$ (Eq. 4). These SLD values imply an ethylene glycol monomer volume of $v_{EG} = 69$ Å^3. The PEG amount per area in terms of the equivalent thickness is therefore also coupled to the corresponding chain equivalent thickness via $D_{PEG} = D_{CH}fNv_{EG}/v_{CH}$. For the single uncompressed brush, the nominal values of ρ_W for D$_2$O, 4MW, SMW, and H$_2$O are used, however allowing for small variations around these nominal values to account for imperfect exchange during the rinsing process. For interacting brushes exposed to H$_2$O-based humidity ρ_W is fixed to the nominal value of H$_2$O.

The profile of the PEG brushes is based on a truncated power law description:

$$\Phi_{PEG}(z) = I(z)\Phi_0 \left(1 - \left(\frac{z}{H_{PEG}}\right)^n\right). \ z \leq H_{PEG} \qquad (6)$$

$I(z)$ represents the smearing of the profile at the rough grafting surface which has the shape of an error function with roughness ζ (see above). H_{PEG} and Φ_0 denote the brush extension and the maximal PEG volume fraction at the grafting surface, respectively. For the single uncompressed PEG brush, the exponent is set as $n = 2$ to generate the parabolic profiles (Fig. 1 D) predicted by analytical SCF theory[102] and confirmed experimentally[99]. For the interacting brushes under compression, $\Phi_{PEG,P}$ is described by Eq. 6 while $\Phi_{PEG,D}$ is described by a mirrored version of Eq. 6 shifted along the z-axis by the grafting surface separation d (Fig. 1 E). Moreover, n is allowed to vary when the brushes get compressed, as previously suggested [86]. Both profiles are truncated at the opposing brush grafting surface in cases when $H_{PEG} \gtrsim d$. Finally, the water profile followed from the requirement

$$\sum_j \Phi_j(z) \equiv 1,$$

$$(7)$$

which in our model for the interacting brushes only holds for all z-values up to the water-free chain layer of the distal lipid monolayer, because we do not account for the air volume fraction explicitly (see Eq. 4). Most of the model parameters are plausibly assumed to be independent of the surface separation d: The SLDs of all components, the proximal and distal lipid and PEG amounts, as well as the roughness, thicknesses, and water fractions of SiO$_2$, OTS, and proximal lipid chain and headgroup slabs. However, the most interesting quantities, namely those concerning the brush conformation and the configuration of the distal lipid monolayer, are allowed to vary with d. The d-dependence of the brush extension H_{PEG} is modeled with an exponential saturation function

$$H_{PEG}(d) = H_{PEG}^{\infty} \cdot [1 - exp(-d/\tau_H)],$$

$$(8)$$

where H_{PEG}^{∞} is the brush extension in the limit of infinite d and is set equal to the value of H_{PEG} obtained for the uncompressed brush. This is justified, because the grafting density of the proximal PEG brush is highly reproducible and because the brush extension exhibits only weak dependence on the grafting density[103]. The adjustable parameter τ_H denotes the characteristic length scale of the saturation. Similarly, the d-dependence of power law exponent n is modeled such that its value converges to that of the unperturbed brush ($n = 2$) for large separations:

$$n(d) = n_0 + (2 - n_0) \cdot [1 - exp(-d/\tau_n)],$$

$$(9)$$

where τ_n denotes the saturation length and h_0 by construction is the extrapolated value of n for $d = 0$. The d-dependence of the roughness (or fluctuation amplitude) ζ_D of the distal lipid layer, is modeled in a more generic manner using a second-order polynomial:

$$\zeta_D(d) = b_0 + b_1 d + b_2 d^2 \tag{10}$$

with adjustable parameters b_0, b_1, and b_2. To simultaneously fit the adjustable parameters of the common model to a set of experimental reflectivity curves (see Figs. 3A and 5A), we followed our previous approach[99] and utilized a procedure specified in the Supporting Information. Estimates of the statistical parameter errors, corresponding to the 95% (two-

sigma) confidence interval are presented in Tables 1-3 in square brackets. Note, however, that these estimates are valid only within the framework of a "perfect model", characterized by a reduced chi-square close to unity ($\chi^2_{red} \approx 1$). In view of significant additional contributions due to systematic errors, alternative error estimates are provided in the tables next to the parameter values. They approximately reflect the variation of the obtained parameters throughout the evolution and refinement of the above-described model description, i.e., they reflect the robustness of the parameters with respect to the model, and we therefore consider them more meaningful.
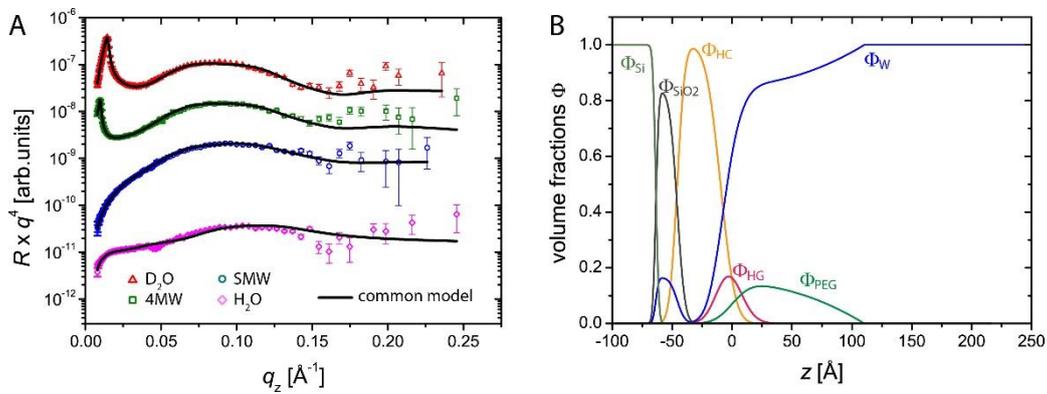
Figure 3: (A) Neutron reflectivity curves (symbols) of a single, uncompressed brush with f = 10% and N = 114 obtained with the four water contrasts D_2O, 4MW, SMW, and H_2O (see Methods section). Solid lines indicate the theoretical reflectivity curves according to the best-matching parameters in the common model. The reduced chi-square deviation is χ^2_{red} = 5.1. (B) Corresponding volume fraction profiles Φ of Si, SiO_2, hydrocarbon chains of OTS and lipids (HC), lipid headgroups (HG), PEG, and water (W).

3. Results and Discussion

3.1. Structure of a Single Uncompressed Brush

Fig. 3 A shows reflectivity curves (symbols) from a single, uncompressed brush (see Fig. 1B) with N = 114 and f = 10%, in D_2O, 4MW, SMW, and H_2O. Solid lines represent simulated intensities for the best matching model parameters. The corresponding volume fraction profiles $\Phi(z)$ of Si, SiO_2, hydrocarbon chains ($\Phi_{HC} = \Phi_{OTS} + \Phi_{CH}$), headgroups, PEG, and water are shown in Fig. 3 B. Apart from the roughness parameters ζ, which are no larger than 12 Å

and given in the Supporting Information, all important model parameters are summarized in Table 1. The thickness of the oxide layer ($d_{SiO2} \approx 18$ Å), the significant fraction of hydration species in the oxide ($\Phi_w^{SiO2} \approx 0.16$), and the thickness of the combined hydrocarbon layer ($d_{HC} = d_{OTS} + d_{CH} \approx 35$ Å) are consistent with earlier studies using similar preparation protocols[98, 99]. The thickness of the hydrated headgroup layer, which was neglected in our previous studies, is $d_{HG} \approx 10$ Å. The extension of the uncompressed brush ($H_{PEG}^{\infty} = 110$ Å), is similar to the 103 Å reported previously for the same sample formulation[99]. Altogether, the agreement between obtained results and earlier reports demonstrates the reproducibility of the sample preparation procedure described in the methods section. The grafting density σ follows from D_{PEG} as $\sigma = D_{PEG}/(N v_{EG}) \approx 13 \times 10^{-4}$ Å^{-2}, where D_{PEG} is the PEG amount per area obtained using Eq. 5.

parameter	d_{SiO2}	Φ_w^{SiO2}	d_{OTS}	$D_{CH} = d_{CH}$	d_{HG}	D_{HG}	D_{PEG}	H_{PEG}^{∞}
value	18 ± 2 Å [0.2 Å]	0.16 ± 0.05 [0.01]	22 ± 2 Å [0.3 Å]	13 ± 1 Å [0.1 Å]	10 ± 5 Å [1 Å]	5 ± 1 Å [0.1 Å]	11 ± 1 Å [0.1 Å]	110 ± 5 Å [1 Å]

Table 1: Best-matching model parameters obtained for a single, uncompressed brush with $N = 114$ and $f = 10$ %. Values in square brackets indicate the purely statistical parameter errors corresponding to a two-sigma confidence interval.

3.2. Pressure-Distance Curves of Interacting brushes

The interaction between extended surfaces across water is typically described in terms of pressure-distance curves, which relate the interaction pressure Π to the water layer

thickness D_w. For fixed temperature T and ambient pressure p, Π represents the derivative of the Gibbs free energy G per unit area A with respect to D_w,

$$\Pi(D_w) = -\frac{1}{A}\left(\frac{dG}{dD_w}\right)_{T,p} \tag{11}$$

Pressure-distance relations can be determined by subjecting interacting surfaces to dehydrating pressures of known magnitude[4, 24]. So-called equivalent pressures can be exerted for instance by controlling the ambient relative humidity h_{rel}, in which case

$$\Pi(h_{rel}) = -\frac{k_B T}{v_w} \ln(h_{rel}), \tag{12}$$

where v_w denotes the volume of a water molecule. Fig. 4 shows pressure-distance curves of various interacting PEG brushes in this double-monolayer architecture obtained by ellipsometry, where the interaction pressure Π was calculated from the measured relative humidity according to Eq. 12. Results are compared for various polymer lengths ($22 \leq N \leq 114$) and PEG-lipid mole fraction ($0 \leq f \leq 10\%$). The grafting densities can be estimated as $\sigma = f/A_{lip}$, where $A_{lip} = 47$ Å^2 is the area per DSPC molecule at 35 mN/m (ref.[104]). As shown previously, this approximation is relatively good for $f \lesssim 10\%$ (ref.[99]). However, for $N = 114$ and $f = 10\%$, the densest brush system studied here, the grafting density measured by NR ($\sigma = 13$ x 10^{-4} Å^{-2}, see previous subsection) is somewhat lower than $f/A_{lip} = 21$ x 10^{-4} Å^{-2}, consistent with ref.[99] and presumably due to the significant lateral repulsion of the overlapping polymer chains. Having this in mind, the relative overlaps for the studied brushes approximately span the range $0 \leq \sigma/\sigma_{OT} \leq 13$, where $\sigma_{OT} = R_F^{-2}$ is the overlap threshold and $R_F = aN^{3/5}$ the Flory radius. With that, both mushroom ($\sigma/\sigma_{OT} \ll 1$) and dilute brush ($\sigma/\sigma_{OT} \gtrsim 1$) regimes are covered. As pointed out by Szleifer[105], the AdG model[77, 78] describes brush interactions only for dense enough cases ($\sigma/\sigma_{OT} \gg 1$). Fig. 4 A shows pressure-distance curves for various N and a constant PEG-lipid mole fraction of $f = 10\%$. In panel B, f is varied for a constant polymer length $N = 114$.
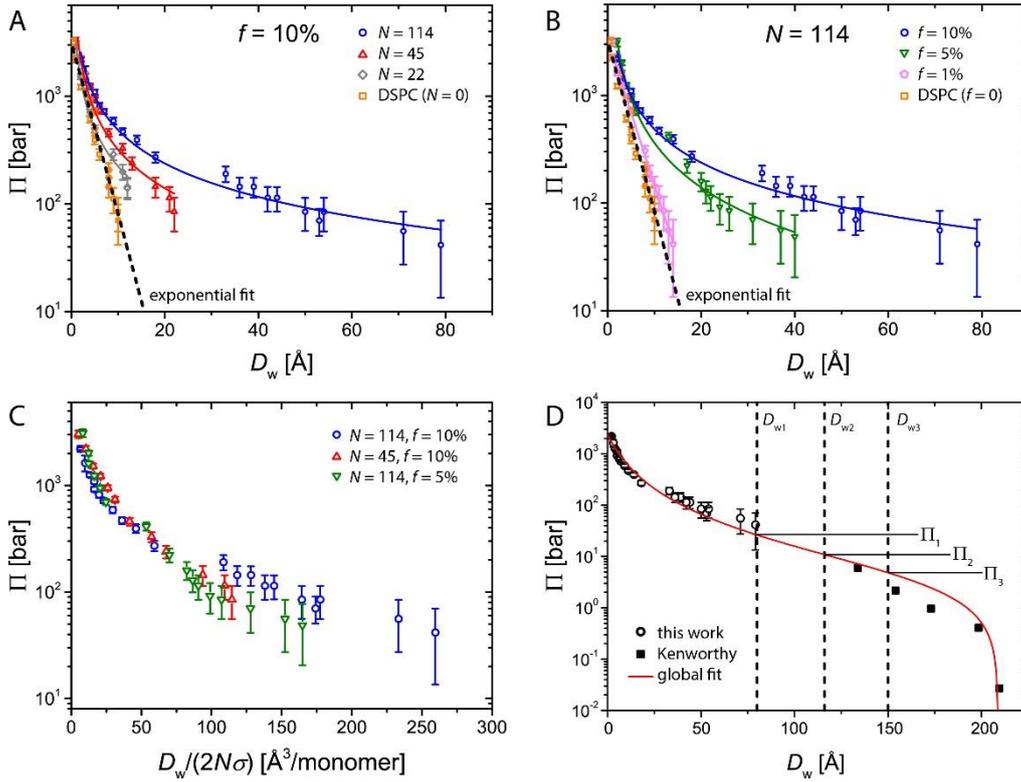
Figure 4: (A and B) Pressure-distance curves obtained by ellipsometry for interacting polymer brushes (A) with constant PEG-lipid mole fraction $f = 10\%$ and various polymerization degrees N and (B) with constant $N = 114$ and various values of f. Solid lines are empirical power-law fits that serve to guide the eye. Dashed lines indicate an exponential fit to the data points for pure DSPC, see main text. (C) Interaction pressure for brushes with $\sigma/\sigma_{OT} \gtrsim 5$ plotted versus the reduced water layer thickness $D_w/(2N\sigma)$. (D) Pressure-distance curve for brushes with $f = 10\%$ and $N = 114$ plotted together with the one obtained previously by Kenworthy et al. [16] for the same formulation in the limit of low interaction pressures. The solid line is a simultaneous fit to both data sets based on the AdG model. Vertical dashed lines indicate the water layer thicknesses D_{w1}, D_{w2}, and D_{w3} for which NR was measured. According to the fit they correspond to interaction pressures $\Pi_1 \approx 25$ bar, $\Pi_2 \approx 10$ bar, $\Pi_3 \approx 5$ bar, respectively, indicated with horizontal lines.

For all brush parameters Π is positive and increases with decreasing D_w, meaning that the interaction is repulsive and work must be performed in order to bring the surfaces closer. Pure DSPC surfaces exhibit the characteristic exponential decay of the PC lipid hydration repulsion with a decay length of about $\lambda_{hyd} = 0.3$ nm (refs.[106, 107]). The dashed straight line in Fig. 4 A and B indicates an exponential fit with $\lambda_{hyd} = 0.28$ nm. In the presence of PEG brushes a systematic increase of the repulsion with increasing N and f is observed. For

dense-enough brushes ($\sigma/\sigma_{OT} \gtrsim 5$), for which the repulsion is dominated by the polymers and the hydration repulsion between the grafting surfaces becomes negligible, all pressure distance curves nearly overlap when they are plotted versus a reduced water layer thickness, $D_w/(2N\sigma)$, which is normalized by the overall grafted PEG amount (Fig. 4 C). This result indicates that in the pressure range covered by the ellipsometry measurements the PEG layer jointly formed by the two interacting brushes approximately behaves like an ideal osmotic medium in which only the monomer density matters irrespective of the polymer connectivity. Deviations from this behavior become significant at larger hydration levels ($D_w/(2N\sigma) \gtrsim 100$ Å^3/monomer). It should be noted that h_{rel} can only be measured and controlled reliably with a certain precision (see Methods section), which in the present study poses a lower detection limit for interaction pressures of $\Pi \gtrsim 50$ bar. A very similar system, composed of self-assembled DSPC/PEG-lipid mixed multilayers in water, has been previously investigated by Kenworthy et al.[16]. They obtained pressure distance curves in the limit of low interaction pressures by the addition of hydrophilic polymers that compete for the hydration water. In Fig. 4 D we plot our data points for f = 10% and N = 114 together with the data points of Kenworthy for the same formulation as a function of D_w. For this purpose, the equivalent thickness of the dry double monolayers, which was measured in the present work by NR as $D_{2ML} \approx 58$ Å (see further below), was subtracted from the lamellar periodicities reported in their work. It is seen that the data points of Kenworthy et al. virtually constitute a continuous extension of our data points to larger separations, i.e., lower pressures. This indicates that the self-assembled multilayers studied by Kenworthy et al. locally exhibit architectures similar to the well-defined monolayer structures characterized here. Lyngs Hansen et al.[108] have scrutinized the applicability of the AdG model to PEG brushes of various parameters and concluded that the brush densities corresponding to the data by Kenworthy et al. in Fig. 4 D are marginally high enough for the AdG model:

$$\Pi(D) = \alpha \left[\left(\frac{L_0}{D/2} \right)^{9/4} - \left(\frac{D/2}{L_0} \right)^{3/4} \right], D < 2L_0 \tag{13}$$

where α is a temperature-dependent pre-factor, L_0 is the uncompressed brush thickness in the AdG approximation, and D is the interaction distance. The solid curve in Fig. 4 D represents a simultaneous fit of Eq. 13 to our data points and to those by Kenworthy et al. To empirically account for the dry volume of PEG, which becomes important at low

hydration, the interaction distance is not set equal to the surface separation, but as $D = D_w + \Delta d$, with an adjustable parameter Δd. The fit yields $\Delta d = 13$ Å and $L_0 = 111$ Å, where the latter is remarkably close to the unperturbed brush extension determined above, $H_{PEG}^{\infty} = 110$ Å. While this result is reassuring, the obtained simultaneous fit to all data points also yields an empirical description of the interaction pressure in the entire hydration range. This is useful especially because our NR results include very highly hydrated states (indicated in Fig. 4 D with dashed vertical lines, see next section), which are not covered by the present ellipsometry measurements.

3.3. Distance-Dependent Structures of Interacting Brushes

Fig. 5 A shows neutron reflectivity curves of interacting lipid-anchored PEG brushes (see Fig. 1C) with $f = 10\%$ and $N = 114$ for various humidity levels. The dehydrating pressure Π depends on h_{rel} according to Eq. 12. As pointed out above, h_{rel} can be measured only to certain precision, so that there is a lower detection limit for Π. Nonetheless, much lower (albeit immeasurable) dehydration pressures can be realized in a humidity chamber using suitable bath temperatures, at least transiently. The corresponding extremely high values of h_{rel}, which come close to the condensation limit, lead to very strong water uptake of the interacting brushes, i.e. to large grafting surface separations d. The latter, in turn, are precisely encoded in the q_z-positions of the minima in the reflectivity curves (see Fig. 5 A). With that, NR puts us in the position to investigate the structure of the interacting brushes in a wide separation range. The sold lines in Fig. 5 A indicate the simulated reflectivity curves corresponding to the best-matching simultaneous model in terms of the d-independent and d-dependent parameters specified in the methods section. Fig. 5 C and D show the corresponding sample structures at humidity 3 (the highest) and 1 (the lowest), respectively, in terms of the volume fraction profiles $\Phi_j(z)$. It is seen immediately that the sample exhibits a highly ordered, layered, and symmetrical structure with the double-monolayer architecture "as intended". Fig. 5 B shows the obtained SLD profiles at humidities 3 and 1. We recall that the proximal brush is deuterated, so that NR can distinguish between the PEG distributions belonging proximal and distal brushes. In particular, the measurements are very sensitive to the brush interpenetration. Namely, the SLD gradient around the midplane

is much sharper for weakly interpenetrating brushes than for strongly penetrating ones. In the following, the best-matching model parameters will be discussed.
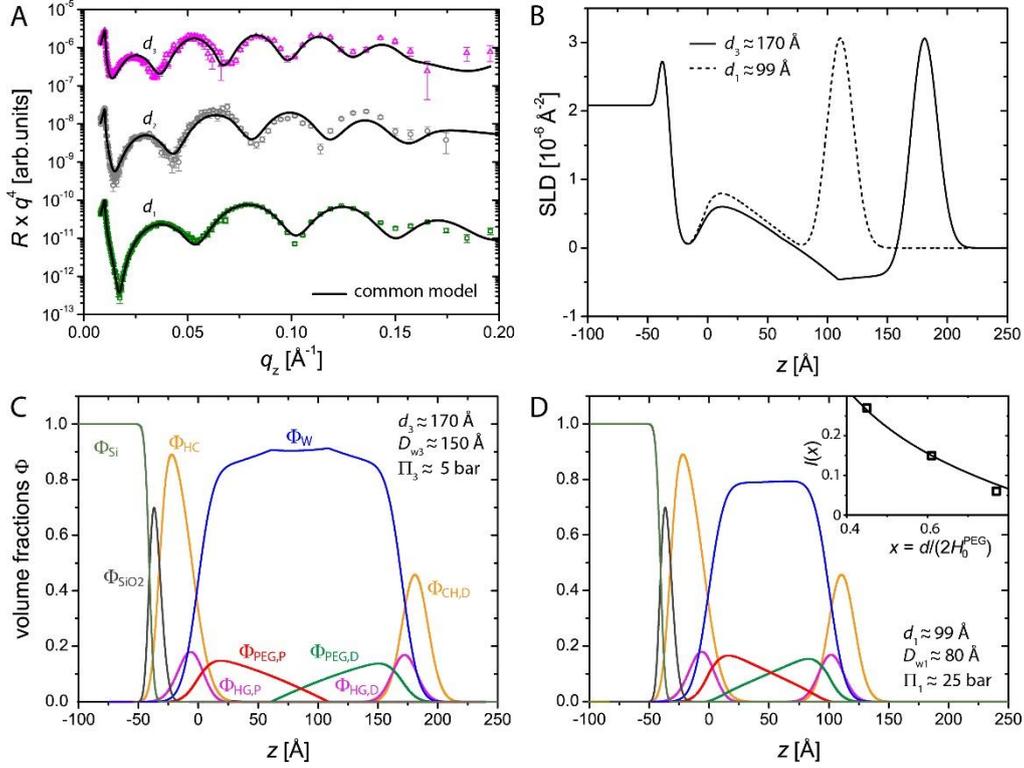
Figure 5: (A) Neutron reflectivity curves (symbols) of interacting two brushes with $f = 10\,\%$ and $N = 114$ obtained for various relative humidities corresponding to grafting surface separations of $d_1 = 99\,\text{Å}$, $d_2 = 135\,\text{Å}$, and $d_3 = 170\,\text{Å}$. Solid lines indicate the theoretical reflectivity curves according to the best-matching parameters in the common model. The reduced chi-square deviation is $\chi^2_{red} = 4.9$. (B) Corresponding scattering length density (SLD) profiles for d_1 and d_3, respectively. (C and D) Corresponding volume fraction profiles for d_3 and d_1, respectively. Inset in panel D: Brush interpenetration as a function of the reduced surface separation x. The solid line represents a scaling law proposed by Murat and Grest[81].

The grafting surface separation d plays a distinct role as it acts as "reaction coordinate" of the interaction. For humidities 1, 2, and 3, respectively, $d_1 = 101\,\text{Å}$, $d_2 = 136\,\text{Å}$, and $d_3 = 171\,\text{Å}$ are obtained. According to Eq. 5, the corresponding water layer thicknesses via the respective water distribution profiles follow as $D_{w1} = 82\,\text{Å}$, $D_{w2} = 117\,\text{Å}$ and $D_{w3} = 152\,\text{Å}$, indicated in Fig. 4 D as dashed vertical lines. The corresponding interaction pressures

according to Eq. 13 with the best-matching parameters of α, L_0 and Δd (solid line in Fig. 4 D) are $\Pi_1 \approx 25$ bar, $\Pi_2 \approx 10$ bar, $\Pi_3 \approx 5$ bar, respectively.

parameter	d_{SiO2}	Φ_w^{SiO2}	d_{OTS}	$d_{CH,P} = D_{CH,P} \approx D_{CH,D} = d_{CH,D}$	$D_{HG,P} \approx D_{HG,D}$	$D_{PEG,P} \approx D_{PEG,D}$
value	8 ± 4 Å [2 Å]	< 0.10 [< 0.05]	14 ± 1 Å [0.5 Å]	13 ± 1 Å [0.3 Å]	5 ± 1 Å [0.1 Å]	11 ± 1 Å [0.3 Å]

Table 2: Best-matching separation-independent model parameters obtained for two interacting brushes with $N = 114$ and $f = 10$ %. Values in square brackets indicate the purely statistical parameter errors corresponding to a two-sigma confidence interval.

The d-independent parameters characterizing SiO$_2$, OTS, as well as proximal and distal monolayers (Table 2) are in satisfactory agreement with those obtained for the single, uncompressed brush (Table 1) and those reported previously for the same preparation protocol [99]. Differences can be attributed to the history of the silicon blocks and to ensuing differences in the efficacy of the OTS deposition. As perceptible already from the overall symmetrical shape of the profiles shown in Fig. 5 C and D and as encoded in $D_{CH,P} \approx D_{CH,P} \approx 13$ Å, the obtained lipid and brush amounts in the proximal and distal monolayers are almost identical. This implies that the transfer ratio for the distal monolayer during preparation was similar to the one for the proximal monolayer, which is known to be close to 100 % (see Methods section). The same by construction also holds for $D_{HG,P}$ and $D_{HG,D}$, as well as for $D_{PEG,P}$, and $D_{PEG,D}$. This result confirms the quality of the employed LS/LB transfer involving a 90° rotation (See Methods section) and justifies the application of theoretical models assuming symmetrical interaction scenarios. The overall equivalent thickness of the two brush-decorated monolayers is $D_{2ML} = D_{HC,P} + D_{HC,D} + D_{HG,P} + D_{HG,D} + D_{PEG,P} + D_{PEG,D} \approx 2(D_{HC,P} + D_{HG,P} + D_{PEG,P}) \approx 58$ Å.

The best-matching d-dependent model parameters are summarized in Table 3. We first have a look at the roughness of the distal lipid surface, $\zeta_D(d)$. The obtained parameters b_0, b_1, and b_2 (Eq. 10) correspond to a virtually d-independent roughness of $\zeta_D \approx 10$ Å throughout the entire separation range $d_1 < d < d_3$. The obtained roughness is somewhat larger than that of a typical lipid monolayer at an air/water interface; however this result is in line with the observation that lipopolymers systematically increase the roughness of lipid monolayers[21]. As seen in Fig. 5 B, the roughness has its manifestation in a significant broadening of the of the lipid headgroup and chain volume fraction profiles $\Phi_{hg,D}(z)$ and $\Phi_{ch,D}(z)$, whose full-widths at half maximum (FWHM) would be as low as $d_{hg} \approx 5$ Å and $d_{ch} \approx 13$ Å, respectively, without roughness. The power law exponent of the PEG brushes, $n(d)$, according to the obtained parameters τ_n and n_0 (Eq. 9) exhibits a weak separation-dependence resulting in $n(d_1) \approx 1.1$, $n(d_2) \approx 1.3$, and $n(d_3) \approx 1.4$. Such a change from a parabolic shape ($n = 2$) to a more linear shape ($n = 1$) upon compression is in qualitative agreement with simulations results by Grest[82] and the experiments by Mulder & Kuhl[86]. The interpenetration of the opposing PEG brushes strongly increases with decreasing surface separation (see Fig. 5 D). The amount of interpenetration, $I(d)$, is determined as[81]:

$$I(d) = \frac{1}{D_{PEG,P}} \int_{d/2}^{\infty} \Phi_{PEG,P}(z,d)dz = \frac{1}{D_{PEG,D}} \int_{-\infty}^{d/2} \Phi_{PEG,D}(z,d)dz.$$

(15)

The resulting values, $I(d_1) \approx 0.27$, $I(d_2) \approx 0.15$, and $I(d_3) \approx 0.06$ are plotted in the inset of Fig. 5 D as a function of the reduced surface separation $x = d/(2H_{PEG}^{\infty})$. Based on an estimation for the brush overlap range by Witten et al.[109], Murat & Grest[81] proposed a scaling law for $I(x)$,

$$I(x) \propto x^{-4/3}(1 - x^3).$$

(16)

The solid line in the inset of Fig. 5 D indicates this scaling law for a suitable pre-factor, and it is seen that it roughly describes our experimental results. Because of the pronounced interpenetration, the compression of the brushes with decreasing separation is weak. This behavior is encoded in the weak d-dependence of the brush extension $H_{PEG}(d)$. The best-matching saturation length is as low as $\tau_H \approx 60$ Å and according to Eq. 8 coincides with $H_{PEG}(d_1) \approx 102$ Å, $H_{PEG}(d_2) \approx 107$ Å, and $H_{PEG}(d_3) \approx 109$ Å. Brush compression is commonly quantified in terms of the compression parameter[80], $\xi(d) = h_{rms}(d)/h_{rms}(\infty)$, where

$$h_{rms}^2(d) = \frac{1}{D_{PEG,P}} \int_{-\infty}^{\infty} z^2 \Phi_{PEG,P}(z,d)dz = \frac{1}{D_{PEG,D}} \int_{-\infty}^{\infty} (d-z)^2 \Phi_{PEG,D}(z,d)dz$$

(14)

is the separation-dependent second moment of the single-sided PEG distributions. For d_1, d_2, and d_3 we obtain $\xi(d_1) \approx 0.85$, $\xi(d_2) \approx 0.91$, and $\xi(d_3) \approx 0.95$, respectively. This level of compression is much weaker than that predicted by analytical SCF theory, which does not account for interpenetration ($\xi_{SCF}(d_1) = 0.57$, $\xi_{SCF}(d_2) = 0.74$, and $\xi_{SCF}(d_3) = 0.89$). While numerical SCF calculations predict significant interpenetration close to the overlap threshold ($\sigma/\sigma_{OT} \gtrsim 1$) (ref.[80]), strong interpenetration comparable to our experimental results as well as the corresponding weak compression are reported only in simulation-based theoretical studies[81-83].

d	D_w	x	ζ_D	H_{PEG}	n	ξ	I
99 ± 2 Å [0.4 Å]	80 ± 2 Å [0.3 Å]	0.45 ± 0.05	10 ± 1 Å [0.1 Å]	102 ± 10 Å [2 Å]	1.1 ± 0.2 [0.1]	0.85 ± 0.5	0.27 ± 0.05
135 ± 2 Å [0.4 Å]	116 ± 2 Å [0.3 Å]	0.61 ± 0.05	10 ± 1 Å [0.1 Å]	107 ± 5 Å [1 Å]	1.3 ± 0.2 [0.1]	0.91 ± 0.5	0.15 ± 0.02
170 ± 2 Å [0.2 Å]	150 ± 2 Å [0.1 Å]	0.77 ± 0.05	10 ± 1 Å [0.1 Å]	109 ± 5 Å [1 Å]	1.4 ± 0.2 [0.1]	0.95 ± 0.5	0.06 ± 0.02

Table 3: Best-matching separation-dependent model parameters obtained for two interacting brushes with $N = 114$ and $f = 10\%$. Values in square brackets indicate the purely statistical parameter errors corresponding to a two-sigma confidence interval. They are not available for the secondary quantities x, ξ, and I.

3.4. Discussion

The AdG model, despite making strong approximations describes the experimentally determined pressure-distance curve in Fig. 4 D surprisingly well over several orders of

magnitude both in pressure and distance, when introducing an empirical, effective interaction distance. In contrast, analytical descriptions like AdG and SCF are less powerful in predicting conformations of interacting brushes. Interpenetration comparable to our experimental results is only observed with rigorous, simulation-based theoretical approaches. Accurate theoretical prediction of brush interpenetration is important because it has strong impact on adhesion forces in chemically dissimilar brushes and on shear friction[79]. Our work therefore motivates further simulation work, especially on dilute brushes and on strongly dehydrated brushes where conformations are no longer governed by a maximization of configurational entropy alone, but also by their molecular-level interaction with water. The latter will require refined treatments of monomer-monomer interactions but may more accurately reproduce pressure-distance curves in the limit of low hydration. In the future, valuable experimental data on brush conformations can be expected from element-specific structural investigations[57], which are sensitive, for instance, to the endpoint-distributions in interacting brushes[88].

4. Conclusions

We have prepared pairs of planar hydrophilic polymer brushes with well-defined parameters in terms of polymerization degree and grafting density. They interact across thin water layers while the grafting surface separation can be adjusted via the application of defined dehydrating pressures. We have demonstrated that this architecture enables the determination of interaction forces and of the separation-dependent internal structures of the interacting brushes at high resolution by neutron reflectometry. The combination of pressure-distance curves and brush conformations in terms of interpenetration and compression yields the most comprehensive experimental description of interacting polymer brushes so far. The results may therefore serve as comparison for refined theoretical models and computer simulations. The presented approach is not limited to polymer brushes but generally applicable to interacting soft interfaces.

Acknowledgements

Neutron Reflectometry Yields Distance-Dependent Structures of Nanometric Polymer Brushes Interacting across Wate

Supporting information

1.) Dry thicknesses of organic layers as obtained by ellipsometry

Tables S1 and S2 summarize the dry thicknesses D_{org} of various organic layers deposited on solid SiO_2 surfaces as determined by ellipsometry. Monolayers (MLs, Table S1) were deposited by LB at 35 mN/m onto non-functionalized hydrophilic surfaces. The organic layer thickness D_{org} therefore directly corresponds to the monolayer thickness d_{ML}. For a pure DSPC ML, the value obtained, $d_{DSPCML} = 25$ Å, is indicative of a dense ML. For DSPC incorporating 10 mol% PEG-lipid with polymerization degree (or monomer number) $N = 114$ the layer is significantly thicker, by 17 Å, owing to the additional PEG material. Double monolayers (DLs, Table S2) were transferred onto OTS-functionalized surfaces using the LS/LB transfer combination described in the main text. The DL thickness D_{DL} therefore follows from D_{org} as $D_{DL} = D_{org} - D_{OTS}$, where D_{OTS} was found to be highly reproducible ($D_{OTS} = 23 \pm 1$ Å). The obtained double layer thicknesses exhibit clearly systematic behavior and are consistent with the monolayer results in Table S1:

1.) Double monolayers are approximately twice as thick as single monolayers ($D_{DL} \approx 2D_{ML}$) when the same formulations are compared.

2.) D_{DSPCDL} is in good agreement with the period $d \approx 60$ Å of dehydrated DSPC multilayers at similar conditions [106].

3.) The layer thickness increases systematically with the incorporated PEG amount. In fact, the PEG thickness D_{PEGDL}, which is obtained by subtracting D_{DSPCDL} from D_{DL}, scales approximately linearly with N. Finally, PEG thicknesses in ML and DL are found to be consistent, $D_{PEGDL} \approx 2D_{PEGML}$ for the same formulation.

In summary, all these observations demonstrate both effectiveness and reproducibility of the LS/LB sample preparation procedures used in the present work.

System	$D_{org} = D_{ML}$	$D_{PEGML} = D_{ML} - D_{DSPCML}$	$2D_{PEGML}$
pure DSPC Monolayer (ML)	$D_{DSPCML} = 25$ Å	-	-
DSPC with PEG-lipid ($f = 10\%$, $N = 114$)	42 Å	17 Å	34 Å

Table S1: Monolayer and sub-layer thicknesses as obtained by ellipsometry.

System	D_{org}	$D_{DL} = D_{org} - D_{OTS}$	$D_{PEGDL} = D_{DL} - D_{DSPCDL}$
OTS	$D_{OTS} = 23 \pm 1$ Å	-	-
OTS + DSPC Double monolayer (DL)	79 Å	$D_{DSPCDL} = 56$ Å	-
OTS + DSPC DL with PEG-lipid ($f = 10\%$, $N = 22$)	87 Å	64 Å	8 Å
OTS + DSPC DL with PEG-lipid ($f = 10\%$, $N = 45$)	92 Å	69 Å	13 Å
OTS + DSPC DL with PEG-lipid ($f = 10\%$, $N = 114$)	114 Å	91 Å	35 Å

Table S1: Double monolayer and sub-layer thicknesses as obtained by ellipsometry.

2) Initial parameter values of the simultaneous fits

Initial values for all parameters concerning the layered structure of the functionalized solid surface and the proximal lipid layer, as well as for the uncompressed brush were taken from the best-matching results obtained in reference [99]. For the interacting brushes under compression the packing density of the distal brush-decorated lipid monolayer was initially set identical to that of the proximal one. The surface separation d was initially adjusted manually to approximately match the overall sample thickness encoded in the hydration-dependent q_z-positions of the reflectivity minima (see Fig. 5 A). In Eq. 7, τ_H was initially set as $H_{PEG}^{\infty}/2$, $\{n_0, \tau_n\}$ in Eq. 8 as $\{2, H_{PEG}^{\infty}/2\}$, and $\{b_0, b_1, b_2\}$ in Eq. 9 as $\{5.0$ Å$, 0, 0\}$.

3) Details of the parameter fitting procedure

To simultaneously fit the adjustable parameters of the common model to a set of experimental reflectivity curves, we utilized the following procedure. Starting from initial parameter values specified in the supporting material, we first calculated the interfacial SLD profiles $\rho(z)$ corresponding to each condition, i.e. for each contrast fluid in case of single uncompressed brush and for each humidity level for the brushes under compression. In the next step, we calculated the reflectivity curves corresponding to the $\rho(z)$ profiles using dynamical reflection theory. To this end the profiles were discretized into hundreds of thin slabs of 1 Å thickness and of constant SLD. The q_z-dependent intensities were then calculated via application of Fresnel's reflection laws at each slab/slab interface using the iterative procedure of Parratt [110]. The procedure was implemented in a self-written fitting program based on the IDL software package (www.harrisgeospatial.com). To optimally constrain all parameters, we simultaneously fit all curves in a set by minimizing the chi-square deviation χ^2 between the entire sets of calculated and experimental reflectivity curves. The best parameter set, with minimal χ^2 was found iteratively using Powell's method[111]. The results were confirmed to be independent of the initial parameter values when they were taken from a physically plausible range. Estimates of the statistical parameter errors, corresponding to the 95% (two-sigma) confidence interval, were derived from the diagonal elements of the corresponding parameter covariance matrix[112].

4) Reflectivity curves from interacting brushes prepared via double LB transfer

Fig. S1 compares reflectivity curves obtained at two hydration levels with (A) the sample prepared by a combination of LS and LB transfers (as in the main text) and with (B) a sample prepared via double LB transfer. It is seen that in (B) the characteristic Kiessig fringes are (i) shifted to higher q_z values, indicating thinner layers and (ii) less pronounced, indicating a weaker SLD contrast. These two observations indicate a poorer transfer ratio and a higher degree of structural disorder.
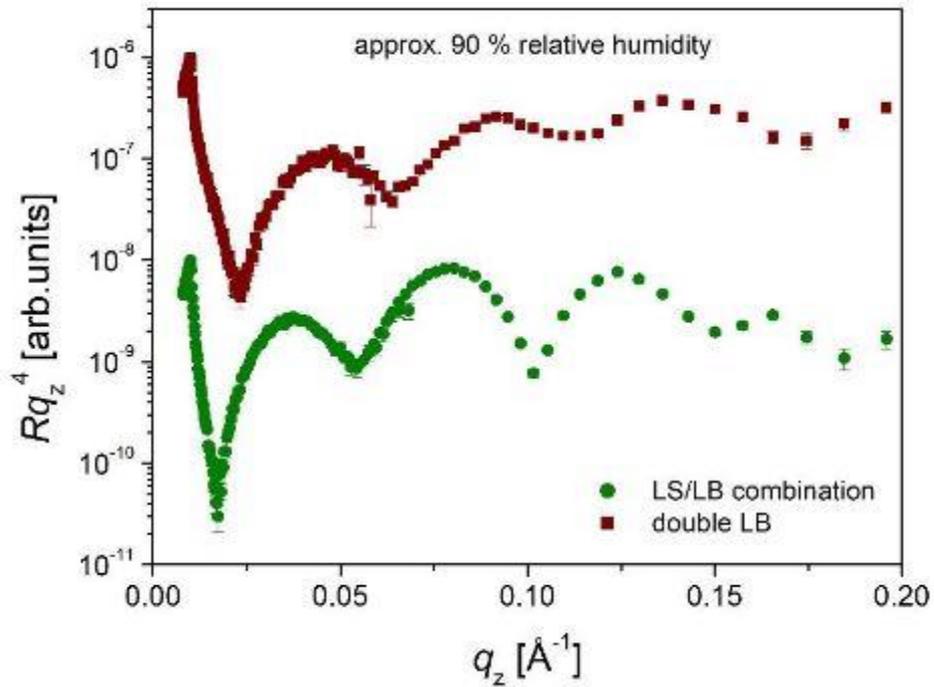
Figure S1: Neutron reflectivity curves at two hydration levels from interacting brushes prepared by a combination of LS and LB transfers (A) and via double LB transfer (B).

5) Best-matching roughness parameters ζ between the slabs describing the substrate and the proximal monolayer

a) Single brush

Si/SiO$_2$	SiO$_2$/ hydrocarbon chain	hydrocarbon chain/ lipid headgroup	lipid headgroup/ water
2 Å	5 Å	7 Å	12 Å

b) Interacting brushes

Si/SiO$_2$	SiO$_2$/ hydrocarbon chain	hydrocarbon chain/ lipid headgroup	lipid headgroup/ water
2 Å	7 Å	12 Å	10 Å

Manuscript 2. Element-Specific Density Profiles in Interacting Biomembrane Models

Emanuel Schneck[a,*], Ignacio Rodriguez-Loureiro[a], Luca Bertinetti[a], Egor Marin[b], Dmitri Novikov[c], Oleg Konovalov[d], and Georgi Gochev[a,e].

[a]Max Planck Institute of Colloids and Interfaces, Am Mühlenberg 1, 14476 Potsdam, Germany

[b]Moscow Institute of Physics and Technology (MIPT), 141700 Dolgoprudniy, Russia

[c]Deutsches Elektronen-Synchrotron (DESY), 22607 Hamburg, Germany

[d]European Synchrotron Radiation Facility, 71 avenue des Martyrs, 38000 Grenoble, France

[e]Institute of Physical Chemistry, Bulgarian Academy of Sciences, 1113 Sofia, Bulgaria

[*]Corresponding author: schneck@mpikg.mpg.de, Phone: +49-331567-9404, Fax: +49-331567-9402

Abstract

Surface interactions involving biomembranes, such as cell-cell interactions or membrane contacts inside cells play important roles in numerous biological processes. Structural insight into the interacting surfaces is a prerequisite to understand the interaction characteristics as well as the underlying physical mechanisms. Here, we work with simplified planar experimental models of membrane surfaces, composed of lipids and lipopolymers. Their interaction is quantified in terms of pressure-distance curves using ellipsometry at controlled dehydrating (interaction) pressures. For selected pressures, their internal structure is investigated by standing-wave x-ray fluorescence (SWXF). This technique yields specific density profiles of the chemical elements P and S belonging to lipid headgroups and polymer chains, as well as counter-ion profiles for charged surfaces.

1. Introduction

Nanometric layers formed by molecular assemblies in two-dimensional architectures are major components of soft and biological matter [1, 3]. Their structural organization and biological or technological functions are highly sensitive to the mutual interactions of their surfaces in the aqueous environment [3, 113]. Important examples in biology are the membranes of cells and organelles, which are typically found under rather crowded conditions [5], so that membrane-membrane interactions play a key role for their functions. The character of the interaction in terms of magnitude and range, as well as whether it is mainly attractive or repulsive, affects cell adhesion [114, 115], vesicle release, the spontaneous formation of membrane stacks [116] and the properties of bacterial biofilms [7]. It in general involves spatially extended (generic) and specific ligand-receptor contributions and is determined by the chemical composition of the membrane surfaces comprising neutral and charged lipid head groups and membrane-bound saccharides, polypeptides, and macromolecules. Similarly, the interaction between technological interfaces also plays an important role in a multitude of applications such as liquid purification and separation chemistry [10], or lubrication [11]. Liquid/liquid interfaces, for example, are commonly stabilized by self-assembled amphiphilic molecules including surfactants, proteins, and polymers, with the aim of rendering their mutual interaction predominantly repulsive thus providing stability of ("soft") colloids [117].

The interaction between two surfaces across water is typically described in terms of pressure-distance curves, which relate the interaction (or: disjoining) pressure Π to the surface separation or (equivalent) water layer thickness D_w. For fixed temperature T and ambient pressure p, Π represents the derivative of the Gibbs free energy G per unit area A with respect to D_w [118],

$$\Pi(D_w) = -\frac{1}{A}\left(\frac{dG}{dD_w}\right)_{T,p}. \tag{1}$$

Pressure-distance relations are commonly determined by subjecting multilamellar stacks of interacting surfaces to dehydrating pressures of known magnitude [24]. So-called equivalent pressures can be exerted either by bringing the multilayers into contact with osmotically active polymer solutions, or by controlling the ambient relative humidity h_{rel}, in which case

$$\Pi(h_{rel}) = -\frac{k_B T}{v_w} ln(h_{rel}), \hspace{4cm} (2)$$

where v_w denotes the volume of a water molecule and k_B is the Boltzmann constant. For biologically or technologically relevant "soft" interfaces, the interaction characteristics are often closely related to molecular conformations and charge distributions [113]. For instance, forces between surfaces displaying charged chemical moieties depend on the exact location of the charges and on their ability to spatially rearrange upon the surfaces' mutual approach. Similarly, electrostatic interactions between charged surfaces are sensitive to the distribution of counterions on the axis perpendicular to the surface plane [13]. Polymer-decorated surfaces, on the other hand, interact differently if the opposing polymer layers are able to overlap [15]. In other words, structural aspects like molecular conformations or element distributions are indicative of the interaction mechanisms and thus of great relevance. However, insight into structures "buried" between two surfaces is difficult to obtain experimentally. X-ray and neutron scattering are among the very few techniques that can probe such structures with the required sub-nanometer spatial resolution. Specular reflectometry reveals matter density profiles perpendicular to an interface [17, 18]. The latter can then be interpreted in terms of interfacial distributions of chemical components [99, 119]. This approach has been taken also to investigate the structure of lipid layers incorporating lipopolymers [120, 121] and of interacting soft interfaces [25, 86, 122]. However, it is not always possible to deduce the relevant structural features from such "global" density profiles. In contrast, x-ray fluorescence allows determining element-specific density profiles across an interface [67]. The technique is based on the characteristic fluorescence induced by the illuminating x-rays via photoelectric ionization and has commonly been used to study element distributions at gas/liquid interfaces [64, 123, 124]. Ångstrom resolution perpendicular to the interface can be achieved with x-ray fluorescence under Bragg diffraction or mirror reflection conditions. In particular, planar nanometer-thick multilayers allow to create strongly modulated standing x-ray waves above the multilayer surface, whose period can be adjusted to match the typical length scales of the objects investigated [59, 60]. Such standing-wave x-ray fluorescence (SWXF) studies have so far dealt with the fluorescence of comparatively heavy elements, often used as labels [67]. Only recently we have established a label-free implementation of SWXF, which is suited to directly localize lighter and biologically relevant chemical elements like P and S with atom scale precision [57].

In the present work, we utilize this technique for the label-free element-specific structural investigation of interacting layers approximately mimicking the surfaces of distinct types of biological membranes. Measurements were carried out at varying humidity corresponding to different equivalent interaction pressures and surface separations. The results are discussed with respect to the pressure-distance curves of the same systems, which were determined in the present work by ellipsometry.
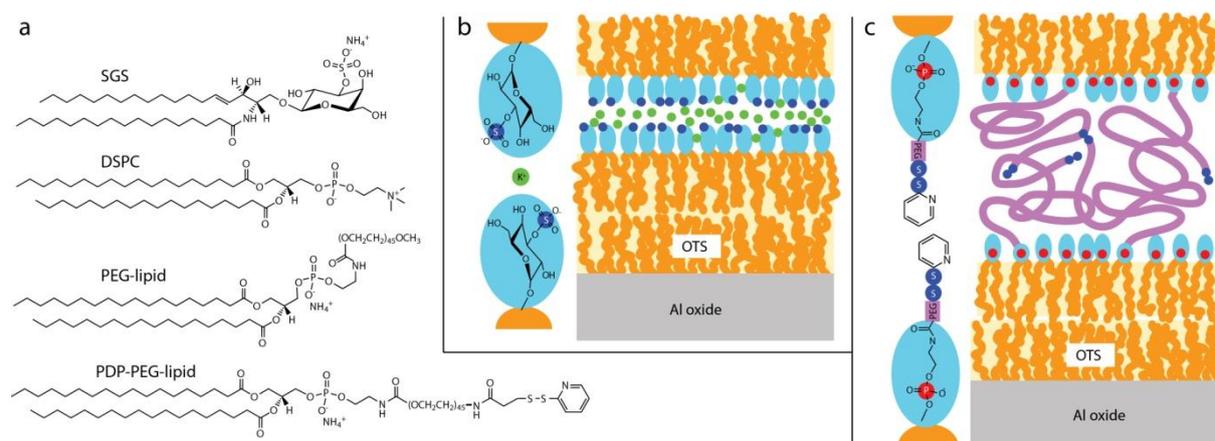
Figure 1: (a) Chemical structures of the amphiphilic molecules SGS (3-O-sulfo-D-galactosyl-ß1-1'-N-heptadecanoyl-D-erythro-sphingosine), DSPC (1,2-distearoyl-*sn*-glycero-3-phosphocholine), PEG-lipid (1,2-distearoyl-sn-glycero-3-phosphoethanolamine-N-[methoxy(polyethylene glycol)-2000]), and PDP-PEG-lipid (1,2-distearoyl-sn-glycero-3-phosphoethanolamine-N-[PDP(polyethylene glycol)-2000]). (b and c) Schematic illustration of the double-monolayer samples investigated in the present study. (b) Interacting SGS surfaces bearing S atoms (dark blue dots) in the lipid headgroups. Green dots indicate K$^+$ counter ions. (c) Interacting lipid-anchored PEG brushes bearing P atoms (red dots) in the lipid headgroups and S atoms at the end of the PEG chains. The solid surfaces are hydrophobically functionalized with octadecyltrichlorosilane (OTS).

2. Results

Fig. 1 b and c schematically illustrate the studied double monolayer samples composed of the amphiphilic molecules shown in Fig. 1 a. They act as defined models of interacting membrane surfaces with known composition. Interacting surfaces composed of the glycolipid (SGS) (Fig. 1 b) represent interacting membranes that contain significant densities of negatively charged sulfoglycolipids, like photosynthetic membranes [125]. Each SGS molecule (Fig. 1 a) comprises one S atom that can be targeted by SWXF. These highly charged models of membrane surfaces are also suited to study the behavior of counterions. Here, the samples were prepared such that the counterions are K^+ ions (see Methods section) that can also be localized with the SWXF settings employed. Interacting lipid-anchored PEG brushes (formed by 10 mol% lipopolymers anchored into a DSPC matrix, see Fig. 1 c) in a generic way represent interacting membrane surfaces displaying hydrophilic macromolecules, such as cell glycocalyx [30], or the outer LPS surfaces of Gram-negative bacteria [7]. SWXF allows localizing the P atoms in DSPC and the lipopolymers (PEG-lipid or PDP-PEG-lipid) and the S atoms in the labeled polymer endpoints of PDP-PEG-lipid (Fig. 1 a). With that, this system is uniquely suited for the simultaneous localization of the grafting surface (via its P content) and the endpoints of the brush (via its S content). Such architectures are therefore interesting also in context with a validation of theoretical models describing the conformation of interacting polymer brushes [81].

Double-monolayer architectures like the ones illustrated in Fig. 1 b and c have similarities with commonly studied supported membranes (the solid support [126]) and lipid monolayers at the air/water interface (the vapor phase [120]). Importantly, they enable the controlled interaction of well-defined surfaces and the simultaneous hydration-dependent structural investigation. Since the amphiphilic monolayers are flexible, a homogeneous surface separation on the planar substrate is always realized, even if impurities, for example dust particles, locally perturb the interaction. This is in contrast to approaches involving two planar solids, where creation of a defined interaction distance is generally challenging [19]. Moreover, double monolayers can be used also for the study of non-symmetrical interaction scenarios and for molecular compositions that do not lead to the spontaneous formation of lamellar phases. This is in contrast to the classical multilayer swelling approach [106]. The interaction strength can be quantified in terms of the equivalent interaction pressure, which is dictated by the humidity (see Eq. 2). The absence of bulk water serves for the controlled dehydration and is therefore desired. For high humidities close to saturation ($h_{rel} \rightarrow 100\%$),

the samples are highly swollen and comprise a large amount of water corresponding to a large equivalent water layer thickness $D_w = v_w N_w / A$, where N_w is the number of water molecules per unit area A. Under this condition the surfaces are further apart than for low humidities, where the samples are less swollen and D_w is smaller.

2.1. Pressure-distance curves

Fig. 2 shows the pressure-distance curves of interacting SGS surfaces and lipid-anchored PEG brushes as determined by ellipsometry (see Methods section). For both systems the interaction pressures are repulsive, meaning that work has to be performed in order to reduce D_w. Close to completely dehydrated conditions ($D_w \rightarrow 0$) the pressures reach magnitudes of several kbars. Upon reducing the equivalent pressure (i.e., increasing the humidity) to the lowest levels achieved in the present work, both systems take up a substantial amount of water, $D_w > 2$nm. But despite these similarities, the repulsion mechanisms leading to water uptake upon releasing the equivalent pressure have to be considered totally different: The repulsion between the negatively charged SGS surfaces is mainly of electrostatic nature. As was shown recently, the range of the repulsive force between glycolipid surfaces increases substantially when negatively charged sulfoglycolipids are incorporated [125]. In contrast, charges play only a minor role for the repulsion between the lipid-anchored PEG brushes. Instead, the hydration of the polymer chains, as well as steric forces related to their configurational entropy are more important. While pure DSPC surfaces like other phosphatidylcholine (PC) lipid surfaces merely experience short range hydration repulsion [106, 127], the incorporation of PEG-lipid was shown to induce additional steric repulsion that systematically increases with polymer length and grafting density [16].
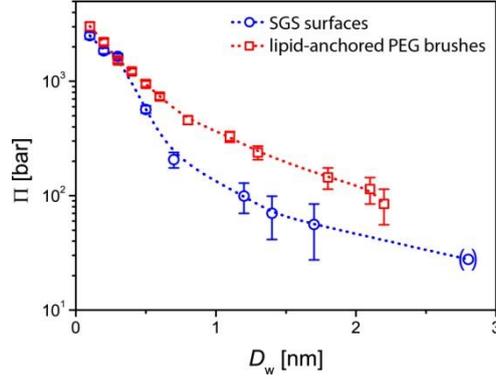
Figure 2: Pressure-distance curves of interacting SGS surfaces (circles) and lipid-anchored PEG brushes (squares). Error bars represent the uncertainty of the humidity sensor. For the data point in brackets the error in Π is comparable to its value. Dashed lines serve to guide the eye.

2.2. Element concentration profiles

Fig. 3 a illustrates the geometry of the SWXF experiments. The technique is based on the element-characteristic fluorescence induced via photoelectric ionization by a standing x-ray wave. The angle of incidence is denoted with θ. Close to the Bragg angle θ_B of the multilayer substrate (here: $\theta_B = 1.13°$), strong reflection occurs, giving rise to a highly modulated standing wave (SW) intensity pattern. Fig. 3 b (symbols) shows the intensity of the reflected beam in a narrow interval of $\pm 0.08°$ around θ_B. The solid line represents the theoretically modeled reflectivity based on a suitable layer representation of the electron density profile of the periodic Al/Ni layers (see Methods section). The θ-dependent fluorescence intensity of a target element j, $I_j(\theta)$, scales with a spatial integral containing the elemental concentration profile perpendicular to the interface, $c_j(z)$, and the θ-dependent SW intensity $\Phi(\theta, z)$:

$$I_j(\theta) = A \int_{-\infty}^{\infty} \Phi(\theta, z)\, c_j(z) dz,$$

$$(3)$$

where A is a pre-factor that involves, among others, fluorescence yield, beam footprint, and detector field-of-view, and therefore weakly depends on θ in general [57]. According to Eq. 3, $c_j(z)$ can thus be deduced from $I_j(\theta)$, if $\Phi(\theta, z)$ is known. The latter was computed via

the phase-correct summation of all reflected and transmitted partial waves [64] from the layer representation mentioned above. For illustration, calculated SW intensity patterns $\Phi(\theta, z)$ above the solid surface are shown in Fig. 3 c for $\theta = \theta_B$ and for $\theta = \theta_B \pm 0.02°$ (see vertical lines in Fig. 3 b). As θ is increased through the Bragg condition, the nodes and antinodes of the SW intensity shift towards the solid surface by approximately half a multilayer period.
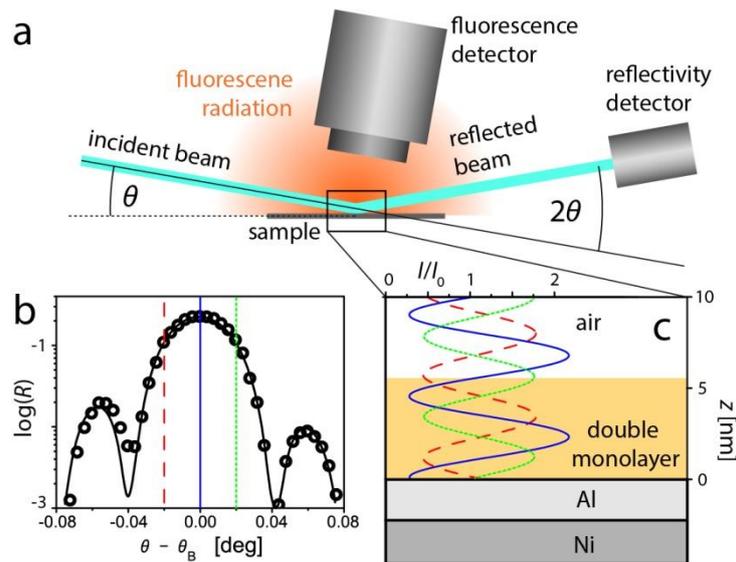
Figure 3: (a) Sketch of the SWXF measurement setup. Incident and reflected x-ray beams are indicated with bright blue lines. The isotropically emitted x-ray fluorescence radiation is indicated in red. The incident angle is denoted with θ. (b) Measured reflectivity curve (symbols) in the vicinity of the first Bragg angle θ_B of the solid multilayers and theoretical model (solid black line). (c) Standing wave intensity patterns $\Phi(\theta, z)$ above the solid surface computed for $\theta = \theta_B$ (solid dark blue line) and for $\theta = \theta_B \pm 0.02°$ (dotted green and dashed red lines, respectively), corresponding to the vertical lines in panel b. The axis perpendicular to the planar solid surface is denoted with z. The region shaded in orange schematically represents the supported monolayer architectures.

Fluorescence spectra were measured for various incident angles in θ-scans around the Bragg angle. Fig. 4 shows a representative spectrum of interacting lipid-anchored PEG brushes (see Fig. 1 c), recorded exemplarily for $\theta = \theta_B$. The spectrum exhibits the characteristic fluorescence peaks of P and S (see inset) together with peaks of Al and other chemical

elements found in the multilayer substrates and in the sample environment (Ar, Ti, and Cr). Ni does not emit fluorescence because the incident beam energy is below the K-shell edge of Ni. The fluorescence intensities of the target elements were extracted from the spectra for each incident angle. For this purpose, from the sample spectra the corresponding reference spectra of the substrates in the absence of the interacting monolayers were subtracted. The peaks of the target elements in the resulting difference spectra were then modeled with Gaussian functions, and the obtained amplitudes were used to build for each element its θ-dependent fluorescence intensity curves $I_j(\theta)$. In the last step, based on the known shape of $\Phi(\theta, z)$, the intensities curves were modeled according to Eq. 3 using a suitable parameterization of the element profiles $c_j(z)$. The weak angle-dependence of the pre-factor A in the equation was approximated linearly with an adjustable parameter for the slope, as was done in ref [57].
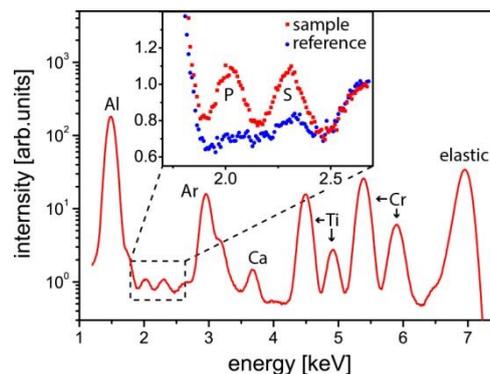
Figure 4: X-ray fluorescence spectrum of interacting lipid-anchored PEG brushes (see Fig. 1 c) recorded exemplarily for $\theta = \theta_B$. The spectrum comprises characteristic peaks of Al and other chemical elements found in the multilayer substrates and in the sample environment (Ar, Ti, and Cr). Inset: Characteristic fluorescence peaks of P and S. Unlike the main panel the inset also shows the comparison with the reference spectrum obtained in the absence of the P and S loaded double monolayer.

2.2.1. Interacting SGS surfaces

Fig. 5 a (bottom curve, symbols) shows the angle-dependent S fluorescence, $I_S(\theta)$, of interacting SGS surfaces (Fig. 1 b) at a low humidity of $h_{rel} \approx 50\%$, corresponding to

$\Pi \approx 1$ kbar (Eq. 2). As suggested by the pressure distance curve (Fig. 2, circles), under strongly dehydrating conditions the water layer between the two sulfur-bearing surfaces is only few Å thick, comparable to the surface roughness. The S distributions belonging to the two surfaces are therefore expected to strongly overlap, resulting in an overall S distribution with only one maximum. The S concentration profile $c_S(z)$ was accordingly modeled as a unimodal distribution,

$$c_S(z) = c - (z - z_S)^2/(2\sigma_S^2)_{max}.$$

     (4)

In this Gaussian representation, the amplitude c_{max}, the center position z_S and the width σ_S are adjustable fitting parameters. While c_{max} merely acts as a scaling parameter, z_S is linked to the angular positions of the extrema in $I_S(\theta)$ and the total form of the curve. The width σ_S is mostly defined by the relative amplitude of the modulation of $I_S(\theta)$ with respect to the "baseline" further away from θ_B. The solid line superimposed to the data points represents the theoretical S fluorescence curve, calculated according to Eq. 3 for the best matching parameters, $z_S = 72$ Å and $\sigma_S = 12$ Å. It is seen that the unimodal distribution reproduces the experimental data points well. The obtained center of mass position, $z_S = 72$ Å above the solid surface is based on the assumption that all the metal layers are 24 Å thick, as calculated from the reflectivity data (see section 4.5), including the uppermost Al and Ni layers. One should expect, however, that the terminal layers are at least partially oxidized and therefore significantly thicker [128, 129], so that the actual surface is shifted along the z-axis. In a previous study in which the surface position had been calibrated on an absolute scale, the center of mass distribution of S in a similar sample at uncontrolled humidity was found at around 58 Å above the surface [57]. In order to be consistent with this value, a thickening of the terminal metal layers of 14 Å by oxidation has to be assumed, which appears plausible. With this definition of the z-axis, which will be used in the following, $z_S = 58$ Å is obtained. The corresponding concentration profile is shown in Fig. 5 c as a solid line. The obtained width of the distribution, $\sigma_S = 12$ Å, at first sight seems to reflect the topographic roughness of solid substrate ($\sigma_{top} \approx 11$ Å, see Methods section). In that case the S distribution could be interpreted as a negligibly thin layer ideally following the corrugations of the solid surface. However, the topographic roughness effectively "seen" by SWXF corresponds to mesoscopic in-plane length scales and can thus be significantly smaller than the one probed by AFM on

the micrometer scale. Moreover the deformable organic layers do not necessarily fully follow these corrugations. Instead, they can have lower topographic roughness due to their considerable interfacial tension. In both cases σ_S would additionally reflect the intrinsic width of the S distribution, also in terms of its bimodal nature. The upper curve in Fig. 5 a (symbols) shows the angle-dependent K fluorescence, $I_K(\theta)$, under the same low-humidity conditions. It exhibits the essentially identical angle dependence as $I_S(\theta)$, and can thus be described satisfactorily with the same parameters (see solid line superimposed to the data points), apart from the trivial scaling parameter c_{max}. In other words, S and K distributions almost perfectly overlap, so that the solid line in Fig. 5 c also describes the K distribution. This co-localization indicates that the counter-ions are always found in the immediate vicinity of the negatively-charged sulfate groups of SGS.
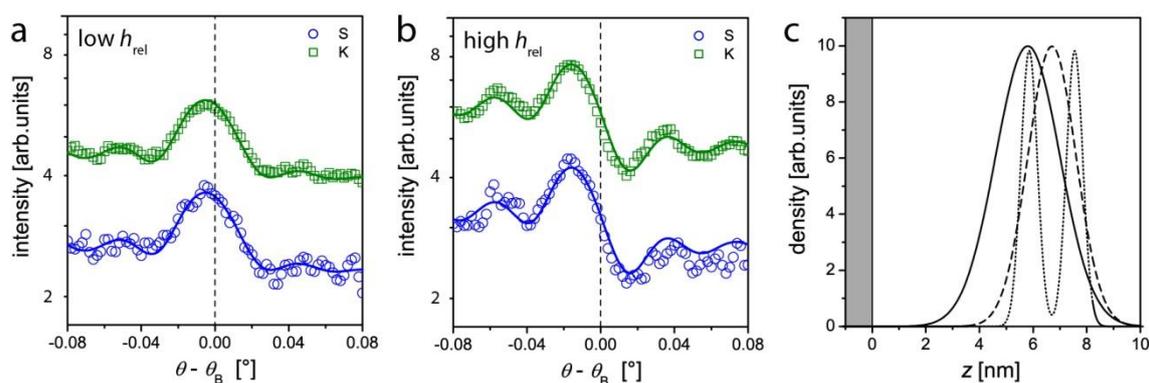
Figure 5: (a) Angle-dependent S and K fluorescence (symbols) from interacting SGS surfaces (see Fig. 1 b) at low humidity. (b) S and K fluorescence from the same sample but at high humidity. Solid lines in (a and b) indicate calculated theoretical intensities corresponding to the best-matching model parameters for the S distributions at low and high humidity. (c) S distributions at low humidity (solid line) and at high humidity when assuming unimodal shape (dashed line). The dotted line indicates a bimodal distribution that would result in approximately the same fluorescence signals (see text). The K distributions at low and high humidity are undistinguishable from the respective S distributions, so that the curves in panel c apply to both S and K.

Fig. 5 b (bottom curve, symbols) shows $I_S(\theta)$ for interacting SGS surfaces at a high humidity of $h_{rel} \approx 93\,\%$, corresponding to $\Pi \approx 100$ bar (Eq. 2). Its angle-dependence is very different from that observed at low humidity, reflecting a significant shift of the S distribution further away from the solid surface. In fact, the data points for high humidity can still be described satisfactorily with a unimodal distribution (Eq. 4), see superimposed solid line for $z_S = 67$ Å and $\sigma_S = 9$ Å. The corresponding concentration profile is shown in Fig. 5 c as a dashed line. This is at first surprising, because the S distributions belonging to the two sulfur-bearing surfaces are expected to separate for thicker water layers, resulting in a bimodal overall S distribution. The unimodal description however still works, because SWXF is sensitive mainly to the first and second moments of a narrow elemental distribution, $z_j = \langle z \rangle$ and $\sigma_j^2 = \left\langle \left(z - z_j\right)^2 \right\rangle$, respectively [57], an aspect that will be discussed further below. First we notice that the shift in z_S when going from low to high h_{rel} is $\delta z = 9$ Å. Assuming that the center of the S distribution belonging to the proximal SGS monolayer is hydration-independent, the S distribution belonging to the distal monolayer would have to shift by $2\delta z = 18$ Å to give the same effect. This extent of swelling upon changing the equivalent pressure from $\Pi \approx 1$ kbar to $\Pi \approx 100$ bar is in rough agreement with the pressure-distance curve of interacting SGS monolayers (Fig. 2). Coming back to the precise shape of the S distribution at high humidity, we note that the S fluorescence data in Fig. 5 b are also consistent with a more plausible, bimodal distribution, provided that it exhibits approximately the same first and second moments of the unimodal distribution used to fit the data. As shown in the supporting information, deviations from this approximation are negligible. A symmetrical bimodal distribution, centered around z_j and comprising two Gaussian peaks of individual width σ_{ind}, separated by a distance Δz, has the same first moment as the unimodal distribution. For the second moment we have $\sigma_{bimod}^{2} = (\Delta z/2)^2 + \sigma_{ind}^2$. When σ_{bimod} is set equal to the width σ_S obtained for the unimodal distribution, we can solve for Δz, which is then only a function of σ_{ind}, $\Delta z = 2\sqrt{\sigma_S^2 - \sigma_{ind}^2}$. The dotted line Fig. 5 c shows an exemplary bimodal distribution with compatible first and second moments as obtained for a very low value of the individual peak width, $\sigma_{ind} = 3$ Å. The upper curve in Fig. 5 b (symbols) shows the angle-dependent K fluorescence, $I_K(\theta)$, under the same high-humidity conditions. Again, it has the same angle dependence as $I_S(\theta)$, indicating perfect overlap of S and K distributions. This result suggests

that, even under highly hydrated conditions the counterions reside closely to the negatively charged surfaces, rather than being evenly distributed in the aqueous phase.

Both the shift in z_S and z_K upon increasing the humidity and the agreement of a bimodal distribution with the experimental data are consistent with the expected swelling behavior of the architecture illustrated in Fig. 1 b. However, it is difficult to rationalize why the second moment of the S distribution does not become larger with increasing hydration level. This behavior may have to do with a more effective healing of the corrugations of the solid surface by the organic layers when they are highly hydrated. In addition one may expect that the saccharide headgroups of SGS undergo significant reorientation with increasing hydration, such that the S atoms get more directed towards the center of the aqueous layer. Alternatively, our experimental results may suggest that the SGS double-monolayers undergo more substantial architectural changes with changing hydration level.

2.2.2. Interacting lipid-anchored PEG brushes

Fig. 6 a (bottom curve, symbols) shows the angle-dependent P fluorescence, $I_P(\theta)$, of interacting lipid-anchored PEG brushes at a low humidity of $h_{rel} \approx 40\,\%$, corresponding to $\Pi \approx 1.3$ kbar (Eq. 2). Even under such dehydrating conditions we expect a clearly bimodal P distribution due to the presence of the PEG layer between the surfaces of the phosphorus-bearing lipid matrix (Fig. 1 c). Moreover, the maxima of the distribution may exhibit a separation comparable to the SW period above the solid surface $\Lambda = 45$ Å (due to refraction effects Λ is not exactly identical to the multilayer period of 48 Å). In this case more than one oscillation of the SW contributes to the fluorescence, an effect that imparts some ambiguity to the data. In fact, $I_P(\theta)$ can readily be reproduced with a unimodal Gaussian distribution with $z_P = 57$ Å and $\sigma_P = 10$ Å, as indicated with the solid line superimposed to the data points. But due to the discrete translational invariance of the SW, the same theoretical curve is obtained for a bimodal distribution with an additional, identical Gaussian peak at $z_P' = z_P + \Lambda = 102$ Å. This bimodal P distribution, which qualitatively is a plausible description of the sample architecture, is shown in Fig. 6 c (upper part, solid line). We remark, however, that on top of this two-fold ambiguity there is also another level of ambiguity with respect to details of the individual Gaussian distributions. Namely, the effective width, $\sigma_P = 10$ Å,

obtained when assuming a unimodal distribution would also result from a bimodal distribution of sharper peaks that are separated by few Å more or less than Λ. However, since the width obtained (σ_P = 10 Å) is already rather low, about as low as σ_{top}, we assume that this ambiguity is of minor relevance and the P distribution plotted in Fig. 6 c provides a satisfactory description of the sample structure. This conclusion is also corroborated by the fact that the position of the proximal P peak in the interacting PEG brushes (z_P = 57 Å) is consistent with the center of the S distribution of the dehydrated SGS double-monolayer (z_S = 58 Å) in light of the similar sample architecture up to the proximal lipid monolayer.

The upper curve in Fig. 6 a (symbols) shows the angle-dependent S fluorescence, $I_S(\theta)$, under the same low-humidity conditions. The fluorescence, originating from S atoms in the PDP-labeled end-points of the PEG chains (Fig. 1 a), assumes a maximum at a significantly larger angle than $I_P(\theta)$ in the same plot, reflecting that P and S have strongly dissimilar distributions. $I_S(\theta)$ is well reproduced for a slightly broader, unimodal distribution with σ_S = 13 Å, located between the two peaks of the P distribution. The best match with the data points is achieved with z_S = 88 Å, see superimposed solid line. The corresponding S distribution is shown in Fig. 6 c (upper part) as a dashed line. The P and S distributions in Fig. 6 c, representing brush grafting surfaces and polymer endpoints, obviously do not match the expected symmetry of the sample architecture, where z_S would ideally coincide with the center between the two P peaks at z = 80 Å. In view of the above-discussed considerable uncertainties in the interpretation of the fluorescence intensities, it is difficult to conclude whether the observed asymmetry is significant, in which case it could reflect, for instance, differences in the packing densities of proximal and distal monolayers.
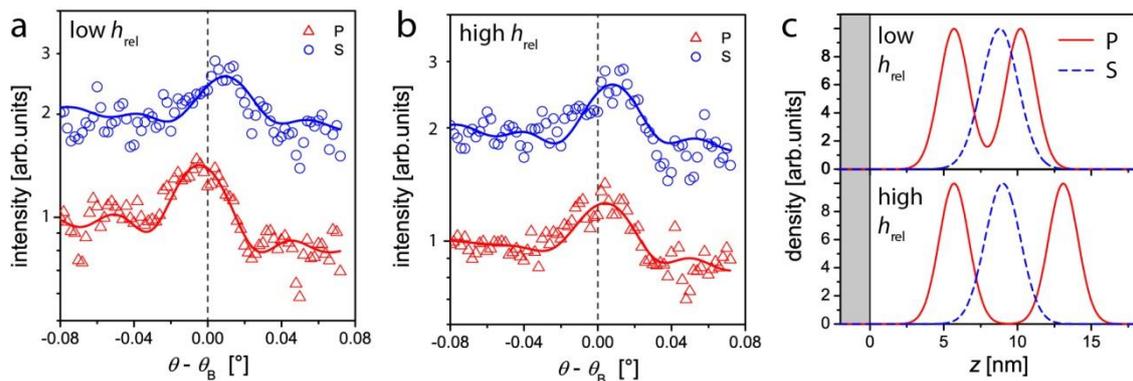
Figure 6: (a) Angle-dependent P and S fluorescence (symbols) from interacting lipid-anchored PEG brushes (see Fig. 1 c) at low humidity. (b) P and S fluorescence from the same sample but at high humidity. Solid lines in (a and b) indicate calculated theoretical intensities corresponding to the respective model parameters for P and S distributions at low and high humidity. (c) P (solid line) and S (dashed line) distributions at low humidity (upper part) and at high humidity (lower part).

Fig. 6 b (bottom curve, symbols) shows $I_P(\theta)$ for the interacting PEG brushes at a high humidity of $h_{rel} \approx 94\,\%$, corresponding to $\Pi \approx 80\,\text{bar}$ (Eq. 2). According to the pressure-distance curve in Fig. 2, swelling by $\gtrsim 2\,\text{nm}$ is expected when reducing the equivalent pressure to this level. A significant change in the P distribution is also evidenced by $I_P(\theta)$, in which the feature-to-baseline level is significantly reduced while the maximum is shifted almost exactly to θ_B at high humidity. An angle dependence like the one obtained for the P fluorescence at high humidity is characteristic for element profiles that are rather equally distributed over the nodes and antinodes of the SW, indicating that the distance between the peaks in a bimodal distribution is closer to an odd than to an even multiple of $\Lambda/2$. Indeed, as indicated with the solid line superimposed to the data points, $I_P(\theta)$ is well reproduced when the distal peak in the bimodal P distribution is shifted to $z_P' = 131\,\text{Å}$ by $29\,\text{Å}$, which is only a fraction of Λ. This shift is also roughly consistent with the swelling observed in the pressure-distance curve of the PEG brushes. The corresponding P distribution is shown as a solid line in the lower part of Fig. 6 c. We remark that the experimental data are reproduced even slightly better when the position of the proximal peak is also allowed to move, in which case it moves towards the solid surface by $2\,\text{Å}$ (not shown). The upper curve in Fig. 6 b (symbols) shows the angle-dependent S fluorescence, $I_S(\theta)$, under the same high-humidity conditions. Within the statistical noise of the data points there are no significant differences between $I_S(\theta)$ at low and high humidity, respectively. The best-matching unimodal S distribution at high humidity, corresponding to the solid line superimposed to the data points, has $\sigma_S = 12\,\text{Å}$ and $z_S = 90\,\text{Å}$, the latter being close to the center between the two P peaks at $z = 94\,\text{Å}$. The corresponding S (or end-point) distribution is shown as a dashed line in the bottom part of Fig. 6 c. The P and S distributions suggest that the symmetry of the double-monolayer architecture is recovered at higher humidity.

Significant differences in the packing densities of proximal and distal monolayers, as speculated above, are therefore not likely the reason for the asymmetry observed at low humidity. The end-point distribution in a single layer of tethered polymers has previously been determined by SWXF [58]. To our knowledge the present results constitute the first determination of the end-point distribution of confined, interacting polymer brushes.

3. Discussion and Conclusions

In the preceding section we have demonstrated that double-monolayer architectures like the ones illustrated in Fig. 1 b and c are well suited for a comprehensive investigation of interacting well-defined surfaces. Namely, such architectures enable the simultaneous determination of pressure-distance curves and of structural details, for example by using x-ray or neutron scattering techniques. We have further demonstrated that SWXF is suited for the label-free and element specific structural investigation of interacting layers. When resolved with high resolution, elemental distributions can yield accurate insight into the molecular configuration of interacting surfaces and its response to changes in the surface separation. In fact, our results suggest that such information is conveniently obtained when elemental distributions are unimodal, for instance when the interacting surfaces have different composition. In many configurations, like the ones described in the present work, the relevant elemental distributions are however multimodal. In these cases detailed molecular conformations are only accessible when the shape of the multimodal distributions can be determined unambiguously. To this end, the topographic roughness of the solid surface poses a limitation, because it leads to a smearing out of the elemental profiles, thus reducing the structural detail. Secondly, ambiguity occurs especially when the distances between the distribution maxima are comparable to the SW period. As a consequence, the structural information obtained from the particular set of measurements presented here does not go much beyond what one could also obtain using conventional reflectometry. Nonetheless, our results constitute a proof-of-concept and clearly demonstrate the potential of SWXF when the crucial parameters are optimized: The roughness-induced smearing out of elemental distributions can be avoided by using multilayer substrates with very smooth surfaces [57]. Ambiguities related to multimodal distributions can be overcome by involving ab-initio information about the sample structure, as well as by a suitable choice of multilayer

periods or by working with multiple angle ranges, e.g., in total reflection and with two sufficiently intense Bragg peaks. One can also consider an experiment with similar samples on two ML substrates of different period. Even in the most unfavorable case of a ML period matching exactly the peak distance in a bi-modal distribution the results stay very sensitive to the changes in the key distribution parameters. Finally, x-ray reflectivity measurements, carried out in parallel on samples of identical composition but supported by simple solids like sapphire or silicon can yield valuable complementary structural information facilitating the interpretation of the x-ray fluorescence data. With that, SWXF may reveal distinct structural aspects not only of generic interactions between soft interfaces but also of specific membrane-membrane interactions for which only the forces have been quantified so far [130, 131].

4. Materials and methods

4.1. Materials

Unless stated otherwise, all chemicals were purchased from Sigma (St. Louis, MO, USA) and used without further purification. Water was purified and double-deionized (MilliQ, Molsheim, France). Sulfoglycolipids (SGS), phospholipids (DSPC), and lipopolymers (PEG-lipid and PDP-PEG-lipid) were purchased from Avanti Polar Lipids (Alabaster, AL, USA). As Illustrated in Fig. 1 a, SGS (3-O-sulfo-D-galactosyl-ß1-1'-N-heptadecanoyl-D-erythro-sphingosine) has two hydrophobic fatty acid tails and a sulfated galactose monosaccharide headgroup. At neutral pH the sulfate carries one negative charge. DSPC (1,2-distearoyl-sn-glycero-3-phosphocholine) has two all-saturated C_{18} chains and a zwitterionic phosphocholine headgroup which carries one P atom. PEG-lipid (1,2-distearoyl-sn-glycero-3-phosphoethanolamine-N-[methoxy(polyethylene glycol)-2000]) is similar to DSPC but a PEG chain comprising 46 monomers is covalently attached to the headgroup. In PDP-PEG-lipid (1,2-distearoyl-sn-glycero-3-phosphoethanolamine-N-[PDP(polyethylene glycol)-2000]), the terminus of the PEG chain is covalently functionalized with a pyridyldithiopropionate (PDP) moiety containing two S atoms. Multilayer substrates were purchased from X'scitech (Helsinki, Finland) and had 25 repetitions of Al(2.4 nm)/Ni(2.4 nm) alternating layers on top of sapphire single crystal wafers with dimensions 8 mm x 8 mm x 1 mm. The terminal Al layer forms amorphous aluminum oxide at the outer surface. Atomic force microscopy

(AFM) was used to reveal the topography of the outer surface and in particular its root-mean-square (rms) roughness, $\sigma_{top} \approx 11$ Å. Silicon wafers (150 mm diameter, 625 µm thickness) with a thermal oxide of defined thickness were purchased from SIEGERT Wafer GmbH (Aachen, Germany).

4.2. Sample preparation

Silicon wafers were cut into pieces of 17 mm x 12 mm. Multilayer substrates and silicon substrates were cleaned by washing with chloroform, acetone, ethanol, and water, followed by UV-ozone treatment. The surfaces were then rendered hydrophobic via covalent functionalization with octadecyltrichlorosilane (OTS) by immersion in 1 mM OTS solutions in anhydrous hexadecane for 1 h and subsequent rinsing in hexadecane and ethanol. SGS, DSPC, and the lipopolymers PEG-lipid and PDP-PEG-lipid were dissolved in chloroform at 2mg/mL. To obtain DSPC / lipopolymer mixtures at a lipopolymer mole fraction of 10mol%, DSPC solution was mixed with PEG-lipid or PDP-PEG-lipid solution, respectively. Double monolayers of SGS or DSPC / lipopolymer on the surfaces multilayer substrates or silicon substrates were prepared using a combination of the Langmuir-Schaefer (LS) and Langmuir-Blodgett (LB) transfer methods [89]. For this purpose, chloroform solutions of SGS or DSPC / lipopolymer mixtures were first spread at the air/water interface in a Langmuir trough (Nima Technology, Coventry, UK; or Riegler & Kirstein GmbH, Potsdam, Germany) containing 1mM KBr aqueous solution (for SGS) or pure water (for DSPC / lipopolymer mixtures). The amphiphilic molecules immobilized at the interface were then compressed to a monolayer with a lateral pressure of 35 ± 1 mN/m. A first lipid layer was deposited onto the hydrophobically functionalized surfaces via LS transfer, i.e., with the solid surface facing the water surface. This procedure reproducibly yields transfer ratios close to 100%, as evidenced from the negligibly small variation of the surface pressure upon the initial contact and as previously confirmed by neutron reflectometry [99]. In the next step the solid substrate was rotated under water by 90°, so that its surface ended up perpendicular to the water surface. The remaining lipid monolayer at the air/water interface was then removed and replaced with a fresh monolayer at the same lateral pressure. This second monolayer was then transferred on top of the first layer by LB, i.e., by pulling the solid substrate upwards. The LB

transfer was confirmed to be effective and reproducible by ellipsometry (see section 4.3. and supporting material).

4.3. Ellipsometry measurements

Ellipsometry enables the characterization of interfacial layers in terms of refractive indices and thicknesses. The method is based on the change in the polarization state of light upon reflection from the surface. For a given refractive index n, the change depends on the layer thickness and is quantified in terms of the phase difference Δ and the amplitude ratio Ψ encoded in the ratio between the complex reflection coefficients R_s and R_p for s and p polarizations, respectively [90]:

$$R_p/R_S = tan\,\Psi\,e^{-i\Delta} \tag{1}$$

For ellipsometry measurements, silicon chips with thermal oxide were used as substrates for the double monolayers. Silicon has the complex refractive index n_{Si} = 3.885 - 0.018i [91]. Measurements were conducted at an incident angle of 70°, with an Optrel Multiskop ellipsometer working with a wavelength λ_{elli} = 632.8 nm. For the known refractive index of SiO$_2$, n_{SiO2} = 1.456 [92], the obtained measurement values (Δ = 79.3°, Ψ = 44.3°) correspond to an oxide layer thickness of 105.5 nm, close to the nominal value of 100 nm. In the next step, the measurement values obtained for the fully dehydrated (h_{rel} < 5 %) samples were modeled with an additional single layer for the organic film comprising OTS and the two deposited monolayers in order to obtain their thicknesses in the absence of water. In this procedure, the refractive index of the organic film was assumed as n_{org} = 1.46, a typical value for organic materials [93-95]. The obtained layer thicknesses exhibit excellent proportionality to the nominal material amount deposited, see supporting material. In the last step, the measurement values obtained at controlled humidity were modeled with an additional water layer (n_{wat} = 1.33) while accounting for the known optical parameters of oxide and dry organic layers. In this way, the humidity-dependent equivalent thickness of the water layer $D_w(h_{rel})$ was determined. Humidity was controlled by placing the samples inside a closed chamber through which humidified N$_2$ was streamed. The gas was humidified by letting it pass through a temperature-controlled water bath in the form of mm-sized bubbles. High humidities were realized by elevating the water temperature to close to or

even slightly above the sample temperature. Low humidities were realized either by lowering the bath temperature or by mixing the humidified N_2 stream with dry N_2. The humidity at the sample position was measured with a calibrated humidity sensor (SHT75, Sensirion AG, Staefa, Switzerland) measurement uncertainty $\Delta h_{rel} = \pm 2\%$), placed close to the sample surface. The equivalent dehydrating pressure follows from h_{rel} according to Eq. 2.

4.4. X-ray experiments

X-ray specular reflectometry and SWXF experiments were carried out at the ID10 beamline of ESRF (Grenoble, France). The sample surface was oriented vertically. The beam was focused in vertical direction while its angular divergence was kept low in horizontal direction in order to obtain a near-parallel incident x-ray wave in the scattering plane. The latter is required to scan the Bragg reflection condition of the periodic metal multilayers with high angular resolution. The beam diameter was 40 µm horizontally and 500 µm vertically. For an illumination close to $\theta_B = 1.13°$, the size of the beam footprint on the surface thus was 500 µm vertically and ≈ 2 mm horizontally. The beam energy was 7.0 keV, corresponding to a wavelength of $\lambda = 1.77$ Å. The fluorescence radiation was measured using a silicon drift detector (Vortex-EM, SII NanoTechnology) placed perpendicular to the beam direction and about 3 mm from the surface. To improve measurement statistics without beam damage to the samples, the angular scans were repeated several times with vertically shifted beam position on the sample surface. In fact, when for test purposes the same position was scanned several times, no significant change in the signals was observed, suggesting that beam damage is negligible.

4.5. Layer representation of the periodic Al/Ni layers

Specular reflectometry from the bare multilayer substrates was measured in order to determine their layered structure, the latter being a prerequisite for accurately modeling the angle dependent SW intensity $\Phi(\theta, z)$. The reflectivity $R(\theta)$ denotes the θ-dependent ratio between the intensities of reflected and incident beams, respectively, and contains information on the electron density distribution perpendicular to an interface. Fig. 7 shows $R(\theta)$ of a multilayer substrate in air, measured in θ-2θ scans with a point detector placed at 2θ (see Fig. 2 a). The substrate was functionalized with OTS, which owing to its weak

electron density contrast (when compared to the solid metal layers) could be safely neglected in the reflectivity analysis. Experimental data (symbols) are corrected for the θ-dependent size of the beam footprint on the sample surface. The red solid line represents the theoretically modeled reflectivity based on a suitable layer representation of the periodic Al/Ni layers. It was computed from the layer representation via application of Fresnel's reflection laws at each interface and a phase-correct summation using the iterative recipe of Parratt [54]. The model assumes 25 periodic repetitions of alternating Al and Ni layers on top of a sapphire (Al_2O_3, electron density 1.19 e⁻/Å³). Thickness and electron density of Al and Ni layers (d_{Al}, d_{Ni}, ρ_{Al}^{el}, and ρ_{Ni}^{el}, respectively) as well as their interfacial roughness were adjustable fitting parameters. The best-matching model parameters were obtained in a minimum χ^2 fit to the experimental data using the programs Motofit [132] and a web-based tool by Sergey Stepanov for reflectivity analysis [133]. The best match was obtained for $d_{Al} \approx d_{Ni} \approx 24$ Å and ρ_{Al}^{el} = 1.23 e⁻/Å³ and ρ_{Ni}^{el} = 2.09 e⁻/Å³. All roughness parameters were found to be no larger than 10 Å. It should be noted that ρ_{Al}^{el} as obtained is about 50% higher than the literature value for pure Al (0.80 e⁻/Å³), while ρ_{Ni}^{el} is slightly lower (about 9 %) than the literature value for pure Ni (2.29 e⁻/Å³), indicating that significant intermixing between Al and Ni layers occurs.
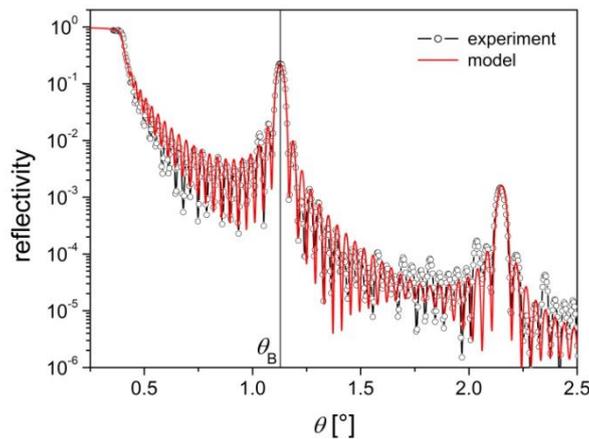
Figure 7: Measured reflectivity curve of a solid multilayer substrate (symbols) together with theoretical reflectivity (solid red line) calculated using a suitable electron density layer model of the periodic Al/Ni structure. The vertical straight line indicates the Bragg angle θ_B.

Acknowledgements

Element-Specific Density Profiles in Interacting Biomembrane Models

Supporting Information

1.) Fluorescence curves from unimodal and bimodal distributions with identical first and second moments

Fig. S1 (solid black line) shows the modeled S fluorescence curve from a unimodal distribution with $\sigma_S = 9$ Å at $z_S = 67$ Å (see main text). The curve is perfectly reproduced for bimodal distribution with $\sigma_{ind} = 3$ Å at $z_{S1} = z_S + \Delta z/2$ and $z_{S2} = z_S - \Delta z/2$, when $\Delta z = 15$ Å (see dashed red line in Fig. S1). This value of Δz is very close to the one predicted if the SWXF technique were only sensitive to the first and second moment of a distribution, in which case $\Delta z = 2\sqrt{\sigma_S^2 - \sigma_{ind}^2} = 17$ Å.

Figure S1: Comparison of modeled fluorescence curves from unimodal (solid black line) and bimodal (dashed red line) distributions.

2.) Dry thicknesses of organic layers as obtained by ellipsometry

Tables S1 and S2 summarize the dry thicknesses d_{org} of various organic layers deposited on solid SiO_2 surfaces as determined by ellipsometry. Monolayers (MLs, Table S1) were deposited by LB at 35 mN/m onto the non-functionalized hydrophilic surfaces. The organic laye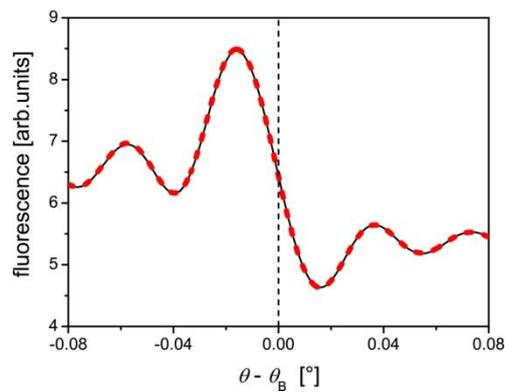r thickness d_{org} therefore directly corresponds to the monolayer thickness d_{ML}. For a pure DSPC ML, the value obtained, $d_{DSPCML} = 25$ Å, is indicative of a dense ML. For DSPC incorporating 10 mol% lipopolymer with polymerization degree (or monomer number) $N = 114$ the layer is significantly thicker, by 17 Å, owing to the additional PEG material. Double monolayers (DLs, Table S2) were transferred onto OTS-functionalized surfaces using the LS/LB transfer combination described in the main text. The DL thickness d_{DL} therefore follows from d_{org} as $d_{DL} = d_{org} - d_{OTS}$, where d_{OTS} was found to be highly reproducible ($d_{OTS} = 23 \pm 1$ Å). The obtained double layer thicknesses exhibit clearly systematic behavior and are consistent with the monolayer results in Table S1:

1.) Double monolayers are approximately twice as thick as single monolayers ($d_{DL} \approx 2d_{ML}$) when the same formulations are compared.

2.) DSPC and SGS Double layers have similar thicknesses, as suggested by their chemical structures. Moreover, d_{DSPCDL} is in good agreement with the period $d \approx 60$ Å of dehydrated DSPC multilayers at similar conditions [106].

3.) The layer thickness increases systematically with the incorporated PEG amount. In fact, the PEG thickness d_{PEGDL}, which is obtained by subtracting d_{DSPCDL} from d_{DL}, scales approximately linearly with N. Finally, PEG thicknesses in ML and DL are found to be consistent, $d_{PEGDL} \approx 2d_{PEGML}$ for the same formulation.

In summary, all these observations demonstrate both effectiveness and reproducibility of the LS/LB sample preparation procedures used in the present work.

System	$d_{org} = d_{ML}$	$d_{PEGML} = d_{ML} - d_{DSPCML}$	$2d_{PEGML}$
pure DSPC Monolayer (ML)	d_{DSPCML} = 25 Å	-	-
DSPC with lipopolymer (f = 10%, N = 114)	42 Å	17 Å	34 Å

Table S1: Monolayer and sub-layer thicknesses as obtained by ellipsometry.

System	d_{org}	$d_{DL} = d_{org} - d_{OTS}$	$d_{PEGDL} = d_{DL} - d_{DSPCDL}$
OTS	d_{OTS} = 23 ± 1 Å	-	-
OTS + DSPC Double monolayer (DL)	79 Å	d_{DSPCDL} = 56 Å	-
OTS + DSPC DL with lipopolymer (f = 10%, N = 22)	87 Å	64 Å	8 Å
OTS + DSPC DL with lipopolymer (f = 10%, N = 45)	92 Å	69 Å	13 Å
OTS + DSPC DL with lipopolymer (f = 10%, N = 114)	114 Å	91 Å	35 Å
OTS + SGS DL	81 Å	d_{SGSDL} = 58 Å	-

Table S1: Double monolayer and sub-layer thicknesses as obtained by ellipsometry.

Manuscript 3. Conformation of Single and Interacting Lipopolysaccharide Surfaces Bearing O-Side Chains

Ignacio Rodriguez-Loureiro[1], Victoria M. Latza[1], Giovanna Fragneto[2], and Emanuel Schneck[1,*]

[1]Max Planck Institute of Colloids and Interfaces, Am Mühlenberg 1, 14476 Potsdam, Germany

[2]Institut Laue-Langevin, 71 avenue des Martyrs, 38000 Grenoble, France

[*]Corresponding author: schneck@mpikg.mpg.de, Phone: +49-331567-9404, Fax: +49-331567-9402

Abstract: The outer surfaces of Gram-negative bacteria are composed of lipopolysaccharide (LPS) molecules exposing oligo- and polysaccharides to the aqueous environment. This unique, structurally complex biological interface is of great scientific interest as it mediates the interaction of bacteria with antimicrobial agents as well as with neighboring bacteria in colonies and biofilms. Structural studies on LPS surfaces, however, have so far dealt almost exclusively with rough mutant LPS of reduced molecular complexity and limited biological relevance. Here, by using neutron reflectometry, we structurally characterize planar monolayers of wild-type LPS from *Escherichia Coli O55:B5* featuring strain-specific O-side chains in the presence and absence of divalent cations and under controlled interaction conditions. The model used for the reflectivity analysis is self-consistent and based on the volume fraction profiles of all chemical components. The saccharide profiles are found to be bimodal, with dense internal oligosaccharides and more dilute, extended O-side chains. For interacting LPS monolayers we establish the pressure-distance curve and determine the distance-dependent saccharide conformation.

1. Introduction

Lipopolysaccharides (LPSs) are the main constituents of the outer monolayer of the Gram-negative bacterial outer membrane [32, 33]. Apart from their structural role, LPS surfaces mediate the interaction of bacteria with their surroundings and act as protection against harmful molecules. LPS molecules consist of a vastly invariant part, constituted by the fundamental building block LipidA and the 'core' oligosaccharide. LipidA possesses four to seven hydrocarbon chains and two phosphorylated, negatively charged glucosamines. The core oligosaccharide is composed of eight to twelve sugar units and carries additional negative charges in the form of phosphate and carboxyl groups. A variable fraction of LPS molecules (called 'smooth' LPS) possess strain-specific O-antigens (O-side chains) in the form of repetitive oligosaccharide motifs [34, 35]. However, the largest LPS fraction (called 'rough' LPS) lacks these O-side chains. The structure of LPS molecules from *Escherichia Coli O55:B5* is presented in Fig. 1. Several *in vivo* studies [36-38] showed that Gram-negative bacteria are resistant against the intrusion of cationic antimicrobial peptides in the presence of divalent cations like Ca^{2+} or Mg^{2+}. Conversely, the outer membrane can be permeabilized with chelating agents like EDTA, which deplete the solution of divalent cations [38, 39]. This phenomenon has been drawing attention due to its fundamental importance for the mode of action of a class of antibacterial drugs [40]. Computer simulations have been used to quantify the interaction of divalent cations with the negatively charged phosphate and carboxyl groups in particular present in the LPS inner core. Coarse-grained simulations involving cationic antimicrobial peptides suggested that divalent cations are able to suppress the penetration of the peptides into the LPS layers and therefore reduce antimicrobial activity [134]. A more recent simulation study further indicated that divalent cations rigidify the outer membrane [135], which was later confirmed also experimentally using interfacial shear rheometry on LPS monolayers [136].

Lipopolysaccharides also largely govern the mutual interaction between neighboring bacteria. This is of particular importance for bacteria in colonies and (undesired) biofilms, where the bacteria are situated side by side [41]. In fact, structure and mechanics of biofilms were shown to be affected by the LPS chemistry [7].

The broad biomedical relevance of Gram-negative bacterial outer surface interactions with ions and drugs as well as of their mutual interactions in colonies have motivated numerous experimental studies on LPS layers. The latter are meaningful model systems because LPS

molecules cover ≈ 75% of the area of bacterial outer surfaces, which additionally contain phospholipids and proteins [32, 33]. Molecular scale structural insight, as required for a mechanistic understanding, is essentially provided only by x-ray and neutron scattering techniques. To this end, rough mutant LPS monolayers at air/water interfaces have been structurally investigated, where the term 'rough mutant' refers to LPS molecules that lack O-side chains and, depending on the degree of mutation, also parts of the core saccharides. Grazing incidence x-ray diffraction (GIXD) revealed the in-plane ordering of such monolayers in the presence and absence of divalent cations or during exposure to antimicrobial peptides [137-139]. Complementary x-ray and neutron reflectometry measurements further revealed the density profiles perpendicular to the interface under various ion conditions [137-140]. Finally, grazing-incidence x-ray fluorescence (GIXF) allowed determining excess ion amounts and distributions in rough mutant LPS surfaces. It was found that divalent cations largely displace monovalent cations from the core oligosaccharide region [64]. More realistic mimics of the Gram-negative bacterial outer membrane have been created at the solid/liquid interface and characterized with x-ray and neutron reflectometry [42, 141-143], some featuring the naturally asymmetric membrane architecture [42, 141, 142], and one incorporating also smooth LPS featuring the strain-specific O-side chains of wild-type bacteria [143]. Concerning the interaction of bacterial surfaces, experimental models have mostly relied on self-assembled rough mutant LPS membrane multilayers [144, 145]. The only study on the structure of interacting wild-type LPS membrane multilayers displaying O-side chains suggested a great importance of divalent cations for the membrane structural integrity [146].

While almost all structural studies on LPS surfaces have so far dealt with rough mutant LPSs missing important features of most bacterial surfaces, those few studies involving wild-type LPSs [143, 146, 147] provided a limited detail of structural insight. Here, we investigate solid-supported monolayers of wild-type LPSs from *Escherichia Coli O55:B5* featuring strain-specific O-side chains (see Fig. 1 B and D). They are structurally characterized by neutron reflectometry (NR) in the presence and absence of calcium and under controlled interaction conditions, using a recently established double-monolayer architecture [148] (see Fig. 1 C and E). With the help of contrast variation, NR provides unambiguous insight into the distributions of the molecular components perpendicular to the interface with high resolution. The saccharide distributions are found to be bimodal, featuring a compact

saccharide layer accommodating the saccharides of LipidA as well as the core saccharides and a more dilute, extended region accommodating the O-side chains. The volume fraction profiles of hydrocarbon chains and saccharides are significantly affected by the depletion of calcium. For interacting LPS monolayers we establish pressure-distance curves and determine the distance-dependent saccharide conformation using a self-consistent model reproducing simultaneously the reflectivity curves obtained for the different distances.
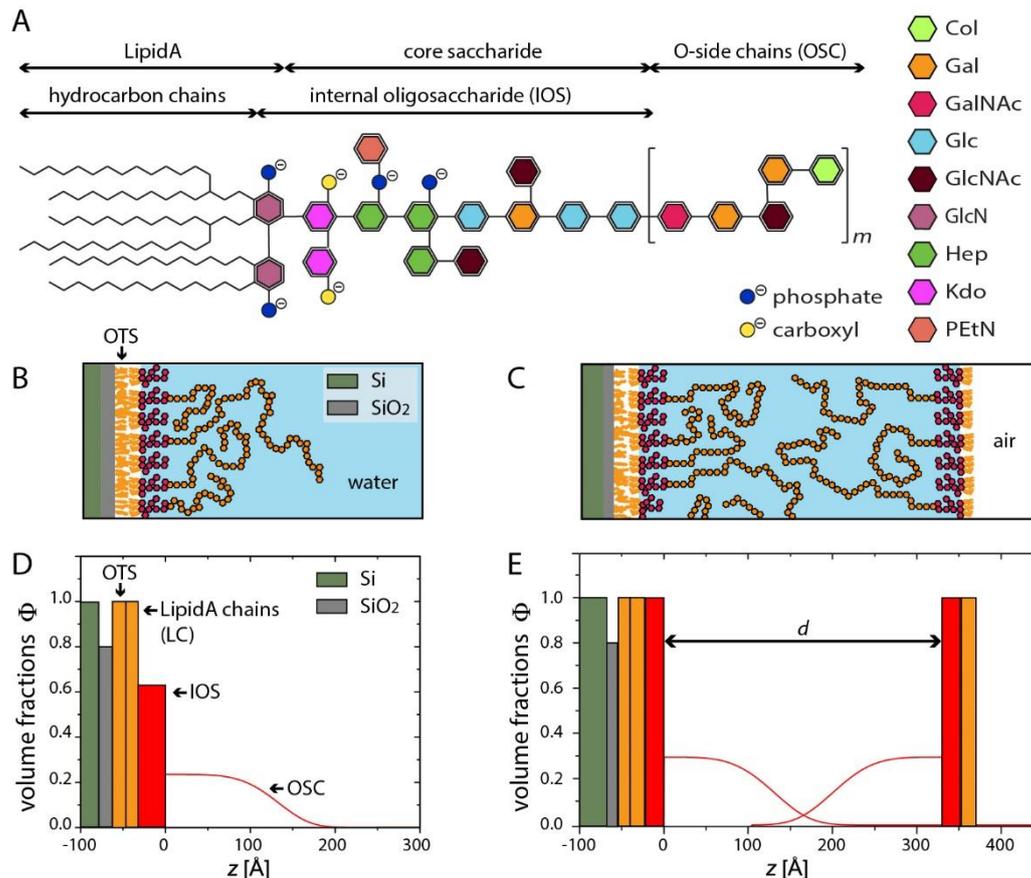
Figure 1: (A) Chemical structure of LPS molecules from *Escherichia Coli O55:B5*, featuring two main units: the LipidA hydrocarbon chains (LC) and a headgroup formed by the internal oligosaccharide (IOS). A certain fraction of the molecules additionally display O-side chains (OSC) consisting of pentasaccharide repeat units. Abbreviations: GlcN = glucosamine, KdO = keto-deoxyoctulosonate, PEtN = phosphorylethanolamine, Hep = L-glycero-D-manno-heptose, Glc = glucose, GlcNAc = N-acetyl-glucosamine, Gal = galactose, GalNAc = N-acetylgalactosamine, Col = colitose. (B) Schematic illustration of a single, solid-supported LPS monolayer in aqueous buffer. The solid surface is hydrophobically functionalized with octadecyltrichlorosilane (OTS). (C) Schematic illustration of two interacting LPS monolayers in a double-monolayer configuration. (D and E) Simplified (roughness-free) representations

of the volume fraction profiles $\Phi(z)$ of all components (Si, SiO$_2$, OTS, LC, IOS, and OSC) in panels B and C, respectively.

2. Materials and Methods

2.1. Materials and sample preparation

Wild-type LPS from *Escherichia Coli O55:B5* (Fig. 1A) and octadecyltrichlorosilane (OTS) were purchased from Sigma (St. Louis, MO, USA) and used without further purification. D$_2$O was pure (99%) and H$_2$O was ultrapure Milli-Q water. *Ca^{2+}-free buffer* contained 150 mM NaCl and 20 mM Tris at pH 7; *Ca^{2+}-loaded buffer* additionally contained 20 mM CaCl$_2$. Silicon single (111) crystal blocks of 50 mm x 50 mm x 10 mm or 50 mm x 40 mm x 10 mm size, polished on one large face, were purchased from Synchrotronix (Annemasse, France). The polished surface was covered with a thin layer of native amorphous silicon oxide (SiO2). Silicon wafers (150 mm diameter, 625 µm thickness) of which the polished surface was covered with a 105 nm layer of thermal silicon oxide were purchased from SIEGERT Wafer GmbH (Aachen, Germany) and cut into rectangular pieces of 20 mm x 10 mm. Silicon blocks and pieces were cleaned by washing with organic solvents (chloroform, acetone, and ethanol) and 20 min UV-ozone treatment. They were then rendered hydrophobic via covalent functionalization with OTS by immersion in freshly prepared solutions of OTS in hexadecane at a concentration of 1 mM for 1 h and subsequent rinsing in hexadecane and ethanol. LPS solutions were prepared following the protocol described by Abraham et al. [147]: liquid phenol (9:1 phenol:water v:v) was mixed with chloroform and petroleum ether in a volume ratio of 2:5:8. A bulk solution of 2 mg LPS per mL was prepared and all subsequent experiments were performed with this stock solution. LPS monolayers were deposited onto the functionalized substrates utilizing a combination of the Langmuir-Schaefer (LS) and Langmuir-Blodgett (LB) techniques [89]. For this purpose, the LPS solution was spread at the air-water interface in a Teflon Langmuir trough (Nima Technology, Coventry, UK) containing 20 mM CaCl$_2$ in H$_2$O. Monolayers were compressed to a lateral pressure of Π_{lat} = 35 mN/m, mimicking biologically relevant membrane densities [149]. A first monolayer was transferred onto the hydrophobic OTS by LS, i.e., with the solid surface facing the water surface. This procedure results in single LPS monolayers exposed to bulk water (see Fig. 1B). No significant change in Π_{lat} upon substrate/monolayer contact was

observed, evidencing a transfer ratio close to 100 %, which is typical for the LS technique. Selected samples were characterized structurally by NR already at this stage (see Results section). In other cases, the Si block was then rotated under water by 90°, so that its surface ended up perpendicular to the water surface. The second monolayer was subsequently transferred by LB, i.e., by pulling the block upwards. As a result, the LPS monolayers face each other as schematically illustrated in Fig. 1C.

2.2 Chemical structure of lipopolysaccharides from *E. Coli O55:B5*

For our purposes, the structure of lipopolysaccharide molecules (Fig. 1A) can be divided into three main moieties: (i) the hydrocarbon chains (CH) of the basic LipidA molecule, (ii) an inner oligosaccharide (IOS) jointly formed by the two phosphorylated and thus negatively charged GlcN moieties of LipidA together with the highly conserved core saccharide of rough mutant LPS, and (iii) the strain-specific O-antigen or O-sidechain (OSC). *E. coli* LipidA typically has four C_{14} hydroxy acyl chains attached to its saccharides and one C_{14} and one C_{12} chain attached to the beta hydroxy groups [150]. The core saccharide of *E. Coli* serotype *O55:B5* is of type R3 [151, 152]. It can be divided into inner and outer core comprising together twelve monosaccharides. At pH 7 the IOS carries six negative charges. The OSC is a polydisperse polymer of an uncharged linear pentasaccharide [151, 153]. Further details on the saccharide composition are given in the Supporting Information.

2.3. Determination of the pressure-distance curve by ellipsometry

Ellipsometry enables the characterization of interfacial layers in terms of refractive indices and thicknesses. The method is based on the change in the polarization state of light upon reflection from the surface [90]. Silicon chips with thermal oxide were used as substrates for the double monolayers. Silicon has the complex refractive index n_{Si} = 3.885 - 0.018i [91]. Measurements of the ellipsometric angles Δ and ψ were performed at an incident angle α_i of 70 deg, with an Optrel Multiskop ellipsometer working with a wavelength λ_{elli} = 632.8 nm. Taking the literature value for the SiO₂ refractive index (n_{SiO2} = 1.457) [92] resulted in a measured SiO₂ layer thickness of 105.5 nm. In the next step, the measurement values obtained for fully dehydrated samples (h_{rel} < 5 %, achieved by streaming with dry N₂) were

modeled while accounting for the above-defined oxide layer properties, to obtain the thickness D_{org} of the dry organic layer jointly formed by OTS and the two LPS monolayers. In this procedure, a refractive index of n_{org} = 1.46 was used, consistent with earlier reports on organic materials [93-95]. The organic layer thickness obtained was D_{org} = 19.1 nm. In the last step, the ellipsometric angles obtained at controlled humidity h_{rel} were modeled while accounting for the known optical parameters of oxide and dry organic layers. The humidity-dependent equivalent thickness (see Eq. 4 below) of the water layer, $D_w(h_{rel})$, was then determined assuming n_w = 1.33 for the refractive index of water. Humidity was controlled by placing the samples inside a closed chamber through which humidified N_2 was streamed. The humidity at the sample position was measured with a calibrated humidity sensor (Sensirion SHT75, measurement uncertainty Δh_{rel} = ± 2%), placed close to the sample surface. Further details are given in reference [148].

2.4. Structural investigation by neutron reflectometry

2.4.1: Setup and experiments

Neutron reflectometry (NR) measurements were performed on the D17 time-of-flight (TOF) reflectometer at the Institut Laue-Langevin (ILL, Grenoble, France). The intensity of the reflected neutron beam relative to the intensity of the incident beam was recorded as a function of the component of the scattering vector normal to the interface, $q_z = (4\pi/\lambda)\sin\theta$, where λ is the neutron wavelength and θ the incident angle. Measurements were carried out at two fixed angles of incidence, θ_1 = 0.8 deg and θ_2 = 3.0 deg (for single LPS monolayers exposed bulk aqueous medium) or θ_2 = 3.2 deg (for interacting LPS monolayers), using a wavelength range of 2.5 Å < λ < 16 Å. The relative resolution in q_z, $\Delta q_z/q_z$, defined via the *full width at half maximum* (FWHM) was q_z-dependent and varied in the range 2% < $\Delta q_z/q_z$ < 11%. While modeling experimental reflectivity curves this was accounted for by convolution. The reflectivity curves displaying the reflected intensity as a function of q_z (see Figs. 2 and 4) depend on the depth profiles of the neutron scattering length density (SLD), $\rho(z)$, across the interface between the two bulk media, Si on one side and water or humidified air, respectively, on the other side. The SLD of a homogeneous medium depends on the number density of the constituting nuclides and on their coherent scattering lengths b_i:

$$\rho = \sum_i \frac{n_i}{v} b_i, \tag{1}$$

where n_i is the number of nuclides i in a volume v. Single LPS monolayers exposed to bulk aqueous medium (see Fig. 1B) were characterized in up to three contrast fluids obtained by mixing H_2O-based and D_2O-based buffers (*Ca²⁺-free* or *Ca²⁺-loaded*, see above) in ratios leading to distinct SLDs. H_2O and D_2O have SLDs of $\rho_w = -0.56 \times 10^{-6}$ Å^{-2} and $\rho_w = 6.36 \times 10^{-6}$ Å^{-2}, respectively. In addition, we used an H_2O/D_2O mixture having $\rho_w = 2.07 \times 10^{-6}$ Å^{-2}, known as *silicon-matched water* or SMW since its SLD matches that of the silicon substrate. For interacting LPS monolayers (see Fig. 1C) the relative humidity was H_2O-based or D_2O-based and was varied using the newest generation humidity cells of D17 [154] using Peltier elements to warm up the sample and a water reservoir thermally isolated from the sample, and a temperature-controlled water bath to cool down. High humidities were realized by elevating the water temperature close to or even slightly above the sample temperature. Since extreme humidities are difficult to maintain over longer periods [96, 97], reflectivity curves were measured in loops of 5 min acquisitions.

2.4.2: Reflectivity data analysis

The reflectivity data were analyzed in the spirit of our recent work on interacting polymer brushes [148]: The samples are described by common models accounting for all measurement conditions. For single solid-supported LPS monolayers in aqueous medium (see Fig. 1B) the corresponding model comprises measurements in all contrast fluids. For interacting LPS monolayers subject to controlled dehydration (see Fig. 1C), the corresponding model accounts for all hydration levels (in both H_2O and D_2O vapor) characterized by their respective surface separations d. Each model describes the volume fractions Φ_i of all compounds, i.e., silicon (i = "Si"), silicon oxide (i = "SiO2"), OTS (i = "OTS"), LipidA chains (i = "LC"), internal oligo saccharides (i = "IOS"), O-side chains (i = "OSC"), and water (i = "W") as functions of the depth coordinate z. It incorporates several adjustable parameters that are fitted simultaneously to the results obtained under different conditions. Simplified schematic illustrations of single and interacting LPS monolayers are presented in Fig. 1 D and E.

The SLD profile for a single solid-supported LPS monolayer is given by:

$$\rho(z) = \Phi_{Si}(z)\rho_{Si} + \Phi_{SiO2}(z)\rho_{SiO2} + \Phi_{OTS}(z)\rho_{OTS} + \Phi_{LC}(z)\rho_{LC}$$
$$+\Phi_{IOS}(z)\rho_{IOS} + \Phi_{OSC}(z)\rho_{OSC} + \Phi_W(z)\rho_W \qquad (2)$$

where z denotes the distance measured along the normal to the planar sample surface. The surface supported by the solid substrate is at $z = 0$ and coincides with the interface between the IOS layer and the aqueous region accommodating the O-side chains (Fig. 1D). When a second LPS monolayer is deposited on top of the first one then the second surface in the analogous definition is located at $z = d$ (Fig. 1E) and the corresponding SLD profile is described as

$$\rho(z) = \Phi_{Si}(z)\rho_{Si} + \Phi_{SiO2}(z)\rho_{SiO2} + \Phi_{OTS}(z)\rho_{OTS} + \left(\Phi_{LC,P}(z) + \Phi_{LC,D}(z)\right)\rho_{CH} + \Phi_W(z)\rho_W$$

$$+ \left(\Phi_{IOS,P}(z) + \Phi_{IOS,D}(z)\right)\rho_{IOS} + \left(\Phi_{OSC,P}(z) + \Phi_{OSC,D}(z)\right)\rho_{OSC} \qquad (3)$$

where we also distinguish between proximal and distal LipidA chains (i = "LC,P" and i = "LC,D", respectively), proximal and distal IOS (i = "IOS,P" and i = "IOS,D", respectively) and proximal and distal O-side chains (i = "OSC,P" and i = "OSC,D", respectively), although they have the same SLD. To quantify the amount per area of each component (except the bulk media) it is convenient to introduce the equivalent thickness

$$D_i = \int_{-\infty}^{\infty} \Phi_i(z)dz, \qquad (4)$$

which can be considered the thickness of an equivalent layer entirely composed of component i. The SLDs of silicon and silicon oxide are fixed at the literature values, ρ_{Si} = 2.07 × 10^{-6} Å^{-2} and ρ_{SiO2} = 3.4 × 10^{-6} Å^{-2}, respectively. The SLD of OTS is allowed to vary between -0.5 × 10^{-6} Å^{-2} and 0, and ρ_{LC} is set to the value for hydrogenous chains, ρ_{LC} = -0.4 × 10^{-6} Å^{-2} [99]. For the calculation of ρ_{IOS} and ρ_{OSC} we consider the partial molecular volumes of the individual constituent sugars of IOS and OSC ([2 GlcN + 3 Hep + 3 Glc + 2 GlcNAc + 1 PEtN + 1 Gal + 2 KdO] per IOS and [2 Gal + 1 Col + 1 GlcNAc + 1 GalNAc] per OSC repeat unit, see Fig. 1A). Further details are given in the Supporting Information. Because of the dynamic exchange of labile hydrogens with the solvent, the resulting SLDs depend on the H_2O/D_2O ratio of their aqueous environment (with SLD ρ_W), and we obtain $\rho_{IOS} \approx$ 2.08 x 10^{-6} Å^{-2} + 0.41ρ_W and $\rho_{OSC} \approx$ 1.77 x 10^{-6} Å^{-2} + 0.34ρ_W.

The volume fraction profile of the crystalline silicon is described as semi-infinite continuum. The profiles of SiO_2, OTS, LipidA chains, and IOS are represented as homogeneous slabs (Fig. 1 D and E). To account for interfacial roughness, the profiles of all slabs are modulated by error functions with adjustable roughness parameters ζ_i. All slab thicknesses, i.e., d_{SiO2},

d_{OTS}, d_{LC}, and d_{IOS}, are adjustable parameters. A finite water fraction is allowed not only in the IOS layer (Φ_w^{IOS}), but also in the SiO$_2$ and LipidA chain layers (Φ_w^{SiO2} and Φ_w^{LC}, respectively), according to earlier reports [99, 146]. Under *Ca^{2+}-loaded* conditions Φ_W^{LC} is however fixed at zero, because the model reproduces the corresponding experimental data without allowing for a finite water fraction in the LipidA chain layer. The water fraction in the hydrophobic OTS layer is always set to zero. For two interacting LPS monolayers, all roughnesses in the distal LPS layer, i.e., roughnesses associated with water/IOS, IOS/LC and LC/air interfaces, are assumed to be identical and described by a single parameter ζ_D. This approximation is justified when the roughness is dominated by the interfacial fluctuations, which are conformal. The O-side chain volume fraction profile of a single, uncompressed LPS surface is modeled as stretched exponential function:

$$\Phi_{OSC}(z) = I(z)\Phi_0 e^{-|z/\Lambda|^n}. \tag{5}$$

$I(z)$ represents the smearing of the profile at the rough grafting surface which has the shape of an error function with roughness ζ (see above). Λ and Φ_0 denote the OSC extension and the maximal OSC volume fraction at the surface, respectively. The exponent n is an adjustable parameter. The stretched exponential description is used because it can describe a wide spectrum of shapes, depending on the stretching exponent. It is therefore well suited to describe empirically the volume fraction profile of polydisperse polysaccharide brushes, for which no reliable prediction exists. For a given OSC amount per unit area, D_{OSC}, which is an adjustable parameter, Φ_0 is not an independent parameter but follows from Λ, n, and the normalization condition (Eq. 4). For two interacting LPS surfaces under compression the OSC profile belonging to the proximal monolayer, $\Phi_{OSC,P}(z)$, is described by Eq. 5 while the one belonging to the distal monolayer, $\Phi_{OSC,D}(z)$, is described by a mirrored version of Eq. 5 shifted along the z-axis by the surface separation d (Fig. 1 E). Both profiles are truncated at the opposing brush grafting surface in cases when $\Lambda \gtrsim d$, which occurs at low hydration. Concerning the LPS amounts in the inner and outer monolayers, a high level of symmetry is found, as in our earlier work on lipid-anchored polymer brushes utilizing the same sample preparation method [148]. It is therefore not necessary to involve independent parameters of D_{LC}, D_{IOS}, and D_{OSC} for the proximal and distal LPS layers. In fact, near-perfect symmetry is obtained, when independent parameter sets are used (see Supporting Information). Consequently, also d_{LC}, d_{IOS}, Λ, and n are assumed to be identical in the proximal and distal

layers for reasons of symmetry. Finally, the water profile between the surfaces follows from the requirement

$$\sum_j \Phi_j(z) \equiv 1.$$

(6)

Most of the model parameters are plausibly assumed to be independent of the surface separation d: The SLDs of all components, the amounts of IOS, OSC, and of the proximal and distal LipidA chains, as well as the thicknesses, roughnesses, and water fractions of SiO_2, OTS, and proximal LipidA chain layers. Moreover, it was not necessary to account for a hydration dependence of the thicknesses of the core saccharide slabs. In contrast, all quantities concerning the O-side chain conformation as well as the roughness of the distal LPS monolayer, are allowed to vary with d.

The d-dependence of the O-side chain extension is modeled with an exponential saturation function

$$\Lambda(d) = \Lambda_0 + (\Lambda_\infty - \Lambda_0) \cdot [1 - exp(- d/\tau_\Lambda)],$$

(7)

where Λ_∞ is the brush extension in the limit of infinite d and is set equal to the value of Λ obtained for the single uncompressed LPS monolayer. The adjustable parameter τ_Λ denotes the characteristic length scale of the saturation. Similarly, the d-dependence of the stretching exponent is modeled such that its value converges to that of the unperturbed O-side chains, n_∞, for large separations:

$$n(d) = n_0 + (n_\infty - n_0) \cdot [1 - exp(- d/\tau_n)],$$

(8)

where τ_n denotes the saturation length. The d-dependence of the roughness (or fluctuation amplitude) ς_D of the distal lipid layer is modeled with an exponential saturation function, too, but with a saturation value ς_∞ that is not specified a priori:

$$\zeta_D(d) = \varsigma_0 + (\varsigma_\infty - \varsigma_0) \cdot [1 - exp(- d/\tau_\varsigma)].$$

(9)

To simultaneously fit the adjustable parameters of the common model to a set of experimental reflectivity curves (see Figs. 2 and 4), we followed our previous approach [99, 148] and utilized a procedure specified in the Supporting Information. The fitting results

were independent of the initial parameter values when they were taken from a physically plausible range. Estimates of the purely statistical parameter errors, corresponding to the 95% (two-sigma) confidence interval are presented in Tables 1 in square brackets. As pointed out previously [148], they typically underestimate substantially the true parameter uncertainties. Therefore, more meaningful error estimates, approximately reflecting the robustness of the parameters with respect to the model, are given in the main text.

Single, solid-supported LPS monolayer in *Ca²⁺-loaded buffer*

d_{SiO2} [Å]	Φ_w^{SiO2}	$d_{HC} = d_{OTS} + d_{LC}$ [Å]	d_{IOS} [Å]	D_{IOS} [Å]	D_{OSC} [Å]	Λ_∞ [Å]	n
17 ± 2 [0.2]	0.2 ± 0.05 [<0.01]	31 ± 2 [1]	31 ± 4 [1.5]	20 ± 3 [1]	30 ± 3 [1]	145 ± 10 [2]	2.5 ± 0.4 [0.2]

Single, solid-supported LPS monolayer in *Ca²⁺-free buffer*

d_{SiO2} [Å]	Φ_w^{SiO2}	Φ_w^{LC}	D_{LC} [Å]	D_{LC} [Å]	d_{IOS} [Å]	D_{IOS} [Å]	D_{OSC} [Å]	Λ_∞ [Å]	n
21 ± 2 [0.4]	0.2 ± 0.05 [<0.01]	0.32 ± 0.05 [0.01]	10 ± 2 [0.2]	15 ± 2 [0.3]	38 ± 4 [1]	17 ± 2 [0.2]	22 ± 2 [0.2]	139 ± 10 [2]	2.7 ± 0.4 [0.3]

Two interacting LPS monolayers

d_{SiO2} [Å]	Φ_w^{SiO2}	d_{OTS} [Å]	$D_{LC,P}$, $D_{LC,D}$, $d_{LC,p}$, $d_{LC,D}$ [Å]	$d_{IOS,P}$, $d_{IOS,D}$ [Å]	$D_{IOS,P}$, $D_{IOS,D}$ [Å]	$D_{OSC,P}$, $D_{OSC,D}$ [Å]
15 ± 2 [0.8]	0.2 ± 0.05 [<0.01]	14 ± 4 [0.5]	17 ± 4 [0.7]	24 ± 4 [0.5]	23 ± 3 [2]	37 ± 5 [4]

Table 1: Best-matching model parameters obtained for a single, solid-supported LPS monolayer in in *Ca²⁺-loaded buffer* (top) and *Ca²⁺-free buffer* (middle) and for two interacting LPS monolayers (bottom). Values in square brackets indicate the purely statistical parameter errors corresponding to a two-sigma confidence interval. Parameters are defined in the text.

3. Results and Discussion

3.1. Structure of a single LPS surface in *Ca²⁺-loaded buffer*

Fig. 2A shows reflectivity curves (symbols) from a single, solid-supported LPS monolayer (see Fig. B) in *Ca²⁺-loaded* buffers based on D_2O, SMW, and H_2O. The approximative chemical equivalence of light and heavy hydrogen is the fundamental assumption underlying the principle of (solvent) contrast variation in neutron scattering. The calcium concentration in *Ca²⁺-loaded buffer* (20 mM) was chosen to be well above the physiological concentration of around 1-2 mM [155], in order to assure LPS layer stability, which is known to be improved in the presence of sufficient concentrations of divalent cations [142], and for better comparability with earlier studies which commonly involved elevated calcium concentrations [137, 146]. Solid lines represent the simulated reflectivities according to the best-matching parameters in the volume fraction profile model. The corresponding profiles $\Phi(z)$ of Si, SiO_2, hydrocarbon chains ($\Phi_{HC} = \Phi_{OTS} + \Phi_{LC}$), IOS, OSC, and water are shown in Fig. 2B. Apart from the roughness parameters ζ, which are no larger than 12 Å and given in the Supporting Information, all relevant model parameters are summarized in Table 1 (top). The thickness of the oxide layer ($d_{SiO2} \approx 17$ Å) and the significant fraction of hydration in the oxide ($\Phi_w^{SiO2} \approx 0.2$) are consistent with earlier studies using similar preparation protocols [99, 156]. In general, the characteristics of silicon oxide layers can be altered by annealing and are sensitive to the annealing conditions [157]. The thickness of the hydrocarbon chain (HC) layer jointly formed by OTS and the LipidA chains (LC) is $d_{HC} \approx 31$ Å. This value is in good agreement with our earlier reports on the OTS layer thickness ($d_{OTS} \approx 17$ Å) [99] and the LipidA chain layer thickness ($d_{LC} \approx 14 - 18$ Å) reported in a NR study by Clifton et al. for rough mutant LPS monolayers [141]. The thickness of the IOS layer is $d_{IOS} \approx 31$ Å, again consistent with the value reported by Clifton et al. for the saccharide headgroup layer ($\approx 28 - 30$ Å). For the amount of IOS per unit area we obtain $D_{IOS} \approx 20$ Å. This result agrees well with the theoretical prediction $D_{IOS} = V_{IOS}/A_{LPS} \approx 19$ Å, based on the total IOS volume ($V_{IOS} \approx 3000$ Å³, see Supporting Information) and the estimated area per molecule ($A_{LPS} \approx 160$ Å², according to Snyder et al. [158]). This accordance suggests that, for an uncompressed LPS monolayer in *Ca²⁺-loaded buffer*, the IOS slab of our model indeed accommodates essentially the saccharides identified in the chemical structure (Fig. 1A). We move on with the analysis of

the O-side chain profile. With the aim to estimate the lateral density of O-side chains (i.e., the fraction of LPSs bearing an O-side chain) as well as the average O-side chain length, we employ self-consistent field (SCF) brush theory for end-grafted non-charged polymers [159]. Even though SCF theory strictly applies to monodisperse polymer brushes while our O-side chains are polydisperse, this description appears to be suitable because $\Phi_{OSC}(z)$ approximately exhibits a parabolic shape as theoretically predicted. As described in the methods section, *E. Coli O55:B5* O-side chains are polymers of linear pentasaccharides. Considering each OSC sugar unit as a monomer, the average volume per monomer is $V_m \approx 200$ Å^3. The linear dimension of a monomer is $a = V_m^{1/3} \approx 6$ Å. Λ defines the decay of the distribution to 1/e. Applying this criterion to the profile of a parabolic brush with height H_0 yields $H_0 = \Lambda/\sqrt{1 - e^{-1}} \approx 180$ Å. The plateau volume fraction is $\Phi_0 \approx 0.22$ (see Fig. 2B). With that, the SCF equations

$$\Phi_0 = \frac{3}{2}\left(\frac{\pi^2}{8p\tau}\right)^{\frac{1}{3}}(a^2\sigma)^{2/3} \qquad \text{and} \qquad (10)$$

$$H_0 = \left(\frac{8p\tau}{\pi^2}\right)^{\frac{1}{3}} aN(a^2\sigma)^{1/3} \qquad (11)$$

can be solved for the grafting density, σ, and the polymerization degree, N, up to an unknown value of $p\tau$. Here, τ is a reduced temperature defined for polymers by the Flory free energy and p is the number of monomers in a persistent segment. An average number of $m \approx 18$ pentasaccharide repeat units (see Fig. 1A for the definition of m), as estimated by Peterson and McGroarty [160] for the same strain using gel filtration chromatography, corresponds to $N \approx 90$ and $p\tau \approx 1.0$. With these values, σ is obtained as 1.5 x 10^{-3} Å^{-2}, corresponding to an approximate 25 % fraction of LPS bearing an O-side chain, somewhat higher than the fraction of charged O-side chains in *Pseudomonas aeruginosa* estimated earlier [143]. In summary, sample architecture and conformation, as obtained here, are in good overall agreement with what can be expected from the chemical structure of the LPS molecules and from earlier estimates of the length and density of the strain specific O-side chains. The observed bimodal saccharide distribution has the characteristics of a two-level filter: The sparse yet extended uncharged 'polymer brush' formed by the O-side chains acts as size-selective filter against large molecules like globular proteins [99]. In contrast, the dense, negatively charged IOS layer can be considered a barrier against harmful small

molecules. It should be noted, however, that this feature is not necessarily the primary function of the bimodal saccharide distribution.

To our knowledge, the present study represents the so-far most detailed structural characterization of a surface composed of wild type bacterial lipopolysaccharides featuring strain-specific O-side chains. It therefore motivates further NR studies on wild type LPS surfaces from different bacterial strains.
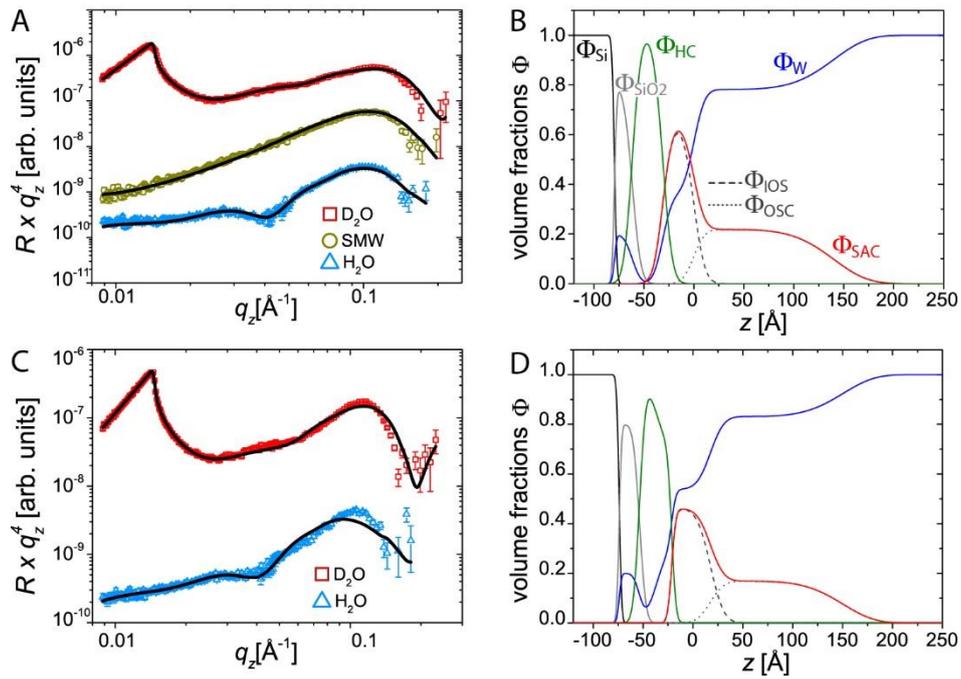
Figure 2: (A) Neutron reflectivity curves (symbols) of a single, solid-supported LPS monolayer in *Ca²⁺-loaded buffer* obtained with three water contrasts, D_2O, SMW, and H_2O (see Methods section). Solid lines indicate the simulated reflectivity curves according to the best-matching parameters in the common model. The reduced chi-square deviation is χ^2_{red} = 4.4. (B) Corresponding volume fraction profiles $\Phi(z)$ of Si, SiO_2, HC (hydrocarbon chains of OTS and LPS combined), IOS, OSC, SAC (saccharides of IOS and OSC combined), and W (water). (C) Neutron reflectivity curves (symbols) and simulated reflectivity curves (lines) of a single, solid-supported LPS monolayer in *Ca²⁺-free buffer* obtained with two water contrasts, D_2O and H_2O. The reduced chi-square deviation is χ^2_{red} = 7.5. (D) Corresponding volume fraction profiles.

3.2. Structure of a single LPS surface in *Ca²⁺-free buffer*

Divalent cations were shown to have a substantial impact on conformation [140, 143], structural organization [137, 138, 142, 146], and mechanics [136, 144] of LPS layers and on the vulnerability of Gram-negative bacteria to antimicrobial peptides [39]. Here, we are in the position to elucidate for the first time the effect of Ca^{2+} depletion on the volume fraction profiles of all chemical components in wild-type LPS surfaces. Fig. 2C shows reflectivity curves (symbols) from a single, solid-supported LPS monolayer in D_2O and H_2O contrasts after replacing *Ca²⁺-loaded buffer* with *Ca²⁺-free buffer*. Solid lines represent the simulated reflectivities according to the best-matching parameters in the volume fraction profile model. The corresponding profiles $\Phi(z)$ of all chemical components are shown in Fig. 2D. The model parameters are summarized in Table 1 (middle), apart from the roughness parameters (all below 12 Å, see Supporting Information). In agreement with earlier work on LPS multi-bilayers [146], reproducing the experimental data requires allowing for a finite water fraction in the LipidA chain region. In the model this is realized by fixing the thickness of the water-impermeable OTS layer to a pre-defined value of d_{OTS} = 17 Å (see Section 3.1.). The water fraction in the LipidA chains is then obtained as $\Phi_W^{LC} \approx 0.3$. The chain amount per unit area is reduced accordingly to $D_{LC} \approx 10$ Å from the value in the presence of divalent cations, $D_{LC} = d_{LC} \approx 14 - 18$ Å, when the water fraction is zero. This result demonstrates that the lateral LPS packing is significantly reduced in the absence of divalent cations. Consistently, the IOS and OSC amounts per unit area decrease by similar percentages, from D_{IOS} = 20 Å and D_{OSC} = 30 Å in *Ca²⁺-loaded buffer* to D_{IOS} = 17 Å and D_{OSC} = 22 Å in *Ca²⁺-free buffer*. This behavior can be rationalized in terms of significant lateral (i.e., in-plane) electrostatic repulsion between the negatively charged IOS, which is much less effectively screened by the monovalent ions alone. Similarly, the increase of the thickness of the IOS layer from $d_{IOS} \approx 31$ Å (*Ca²⁺-loaded*) to $d_{IOS} \approx 38$ Å (*Ca²⁺-free*) suggests an electrostatically driven IOS stretching under conditions of weaker screening, as reported earlier for rough mutant LPS [140]. The expansion of the core saccharides in both in-plane and out-of-plane directions in the absence of calcium results in a considerable reduction of their volume density, as reflected in the reduction of the maximal IOS volume fraction from $\approx$ 0.62 to

≈ 0.46 (Fig. 2 B and D). Under these conditions the intrusion of harmful molecules will be facilitated, in line with the common assumption of a weakening of the LPS barrier function through calcium depletion. This picture is corroborated by the observation of water in the LipidA chain region discussed above, which further points towards the loss of a uniform hydrophobic barrier. The shape of the OSC profile is not significantly affected by Ca^{2+} depletion (see Fig. 2 B and D), as encoded in the similar values of Λ and n (Tables 1 top and middle), apart from the lower plateau volume fraction ($\Phi_0 \approx 0.17$, see Fig. 2D). This result obtained with charge-neutral O-side chains is in contrast to an earlier study on LPS from *Pseudomonas aeruginosa* with negatively charged O-side chains, whose conformation exhibited pronounced Ca^{2+}-dependence [143]. Based on the documented strong effect of even very low calcium concentrations on the behavior of negatively charged membranes [161], we speculate that physiological conditions are more closely represented by the *Ca^{2+}- loaded* case discussed above than by *Ca^{2+}-free* conditions.

3.3. Pressure-distance curve of interacting LPS surfaces

The interaction between two surfaces in water can be described in terms of pressure-distance curves[24], which relate the interaction pressure Π to the water layer thickness D_w. Equivalent interaction pressures can be exerted for instance by controlling the ambient relative humidity h_{rel}, in which case

$$\Pi(h_{rel}) = -\frac{k_B T}{v_w} ln(h_{rel}), \qquad (12)$$

where v_w denotes the volume of a water molecule. Fig. 3 shows the pressure-distance curve $\Pi(D_w)$ of interacting LPS monolayers obtained by ellipsometry measurements at controlled humidities. In dehydrated state ($D_w \approx 0$, achieved with a stream of dry N_2 gas), the measured thickness of the organic layer is $D_{org} = D_{OTS} + D_{2LPS} \approx 190$ Å. The interaction pressure $\Pi(D_w)$ was calculated according to Eq. 12. It is positive and increases with decreasing D_w, meaning that the interaction is repulsive, and work must be performed in order to bring the LPS surfaces closer. In the humidity range covered by the ellipsometry measurements, the water layer thickness increases up to $D_w = 194$ Å. This swelling range is significantly larger than the one reported recently for interacting PEG brushes of comparable grafting density and contour length [148]. It should be noted that h_{rel} can only be measured and controlled

reliably with a certain precision (see Methods section), which in the present study poses a lower detection limit for interaction pressures of $\Pi \gtrsim 50$ bar. To interpret the shape of the experimentally obtained pressure-distance curve in Fig. 3, we use the Alexander-de Gennes (AdG) model [77, 78]

$$\Pi(D) = \alpha \left[\left(\frac{L_0}{D/2} \right)^{9/4} - \left(\frac{D/2}{L_0} \right)^{3/4} \right], \quad D < 2L_0 \qquad (13)$$

which already provided a surprisingly good description of the interaction pressure between opposing PEG brushes when empirically accounting for the dry polymer volume [148]. In Eq. 13, α is a temperature-dependent pre-factor, L_0 is the uncompressed brush thickness in the AdG approximation, and D is the interaction distance. The solid curve in Fig. 3 represents a fit of Eq. 13 to our data points, where L_0 is set equal to the value of H_0 (see previous section) as an approximation suggested in our earlier study [148]. To account for the O-side chain dry volume, the interaction distance is not set equal to the surface separation, but as $D = D_w + \Delta d$, where Δd is an adjustable parameter. The empirical fit yields $\Delta d \approx 30$ Å and provides a good description of the experimental data points. Moreover, the fit also provides a reasonable estimate of the interaction pressure at the highest hydration levels reached in the NR measurements (see vertical dashed lines in Fig. 3), which are not covered by the experimental pressure distance curve.

Within the experimental data range and within the theoretical framework applied, the interaction between the two LPS surfaces is purely repulsive. This result is non-trivial, because favorable interactions between neutral membrane-bound saccharides exist and can lead to attraction [162]. For long, flexible sugar polymers like the OSC in the present study, however, significant attractive saccharide-saccharide interactions can be excluded, because they would induce a self-collapse of the OSC brush. Mutual adhesion between bacteria in a colony will therefore likely always require additional crosslinking by specific, protein-based mechanisms [163], against the generic polymer repulsion afforded by the O-side chains.
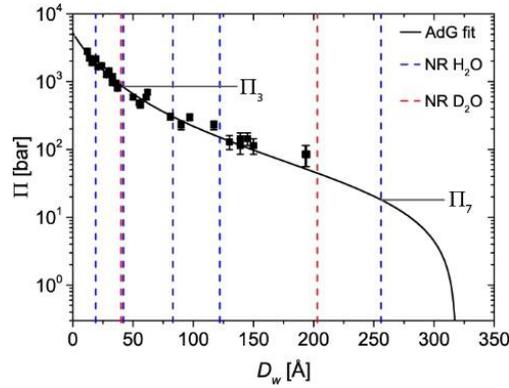
Figure 3: Pressure distance curve (symbols) of two interacting LPS monolayers as obtained by ellipsometry. The solid line is a fit to the data points based on the AdG model with the boundary condition $L_0 = H_0$ (see Eq. 13 and associated text). Vertical dashed lines indicate the water layer thicknesses D_w for which NR measurements were performed in H_2O (D_{w1}, D_{w3}, D_{w4}, D_{w5}, D_{w7}, see Table 2) and D_2O (D_{w2}, D_{w6}) vapor. Π_3 and Π_7 indicate the approximate interaction pressures corresponding to the structures at D_{w3} and D_{w7} shown in Fig. 4 C and D, respectively.

3.4. Distance-dependent structures of interacting LPS surfaces

Fig. 4A shows neutron reflectivity curves of two interacting LPS surfaces (see Fig. 1C) for various humidity levels h_{rel}. The dehydrating pressure Π depends on h_{rel} according to Eq. 12. As pointed out above, h_{rel} can be measured only to a certain precision, so that there is a lower detection limit for Π. Dehydration pressures below the detection limit can nevertheless be realized transiently in a humidity chamber using suitable bath temperatures. The corresponding extremely high values of h_{rel}, almost reaching the condensation limit, lead to very strong water uptake into the interacting LPS surfaces, i.e. to large grafting surface separations d. The latter, in turn, are precisely encoded in the q_z-positions of the minima in the reflectivity curves. With that, NR puts us in the position to investigate the structure of the interacting LPS surfaces in a wide separation range. The solid lines in Fig. 4A indicate the simulated reflectivity curves corresponding to the best-matching model in terms of the d-independent and d-dependent parameters specified in the methods section. Note that a single global model of the d-dependent structure simultaneously reproduces all seven reflectivity curves obtained with both H_2O and D_2O contrasts (Footnote 1). This is remarkable in view of the complexity of the sample regarding chemistry and architecture.

Fig. 4B shows the SLD profiles in H_2O contrast at the highest humidity corresponding to a surface separation of $d \approx 328$ Å ($d = d_7$, see Table 2) and at a lower humidity corresponding to $d \approx 113$ Å ($d = d_3$). Panels C and D of Fig. 4 show the corresponding sample structures at the same hydration levels in terms of the volume fraction profiles $\Phi_j(z)$. It is seen that the sample exhibits a highly ordered, layered, and symmetrical structure consistent with the double-monolayer architecture depicted in Fig. 1C. In the following, the best-matching model parameters will be discussed.

surface separation	water layer thickness	interaction pressure
$d_1 = 91 \pm 5$ Å [0.6 Å]	$D_{w1} = 19 \pm 5$ Å	$\Pi_1 \approx 1900$ bar
$d_2 = 111 \pm 5$ Å [0.3 Å]	$D_{w2} = 40 \pm 5$ Å	$\Pi_2 \approx 900$ bar
$d_3 = 113 \pm 5$ Å [0.5 Å]	$D_{w3} = 42 \pm 5$ Å	$\Pi_3 \approx 800$ bar
$d_4 = 155 \pm 5$ Å [0.9 Å]	$D_{w4} = 83 \pm 5$ Å	$\Pi_4 \approx 300$ bar
$d_5 = 194 \pm 5$ Å [1.4 Å]	$D_{w5} = 122 \pm 5$ Å	$\Pi_5 \approx 150$ bar
$d_6 = 275 \pm 5$ Å [0.7 Å]	$D_{w6} = 203 \pm 5$ Å	$\Pi_6 \approx 50$ bar
$d_7 = 328 \pm 5$ Å [1.3 Å]	$D_{w7} = 256 \pm 5$ Å	$\Pi_7 \approx 20$ bar

Table 2: Obtained surface separations and water layer thicknesses as well as the corresponding interaction pressures according to the AdG model (solid line in Fig. 3). Values in square brackets indicate the purely statistical parameter errors corresponding to a two-sigma confidence interval.

The surface separation d plays a distinct role as "reaction coordinate" of the interaction. For humidities 1 to 7, surface separations between $d_1 = 91$ Å and $d_7 = 328$ Å are obtained (see Table 2). According to Eq. 4, the corresponding water layer thicknesses via the respective

water distribution profiles range between $D_{w1} = 19$ Å and $D_{w7} = 256$ Å (Table 2). They are indicated in Fig. 3 as dashed vertical lines. The approximate interaction pressures according to Eq. 13 with the best-matching parameters of α and Δd (solid line in Fig. 3) range between $\Pi_1 \approx 1900$ bar and $\Pi_7 \approx 20$ bar (Table 2). The d-independent parameters are summarized in Table 1 (bottom). The parameters characterizing SiO_2 and OTS are in satisfactory agreement with those obtained for the single LPS surface. Differences can be attributed to the history of the silicon blocks and to ensuing differences in the oxide layer thickness and the efficacy of the OTS deposition. The obtained equivalent thickness of the organic layers is $D_{org} = D_{OTS} + D_{2LPS} = D_{OTS} + D_{LC,P} + D_{IOS,P} + D_{OSC,P} + D_{LC,D} + D_{IOS,D} + D_{OSC,D} \approx 168$ Å, in reasonable agreement with the respective value obtained by ellipsometry, $D_{org} \approx 190$ Å (see previous section). The $\approx 10\%$ difference can be attributed to uncertainties in the choice of the LPS refractive index in the ellipsometry analysis. The total saccharide amount per LPS monolayer and unit area, $D_{SAC,P} = D_{SAC,D} = (D_{IOS,P} + D_{OSC,P} + D_{IOS,D} + D_{OSC,D})/2 \approx 60$ Å, is slightly larger than the one obtained for the single LPS surface in bulk Ca^{2+}-loaded buffer ($D_{SAC} \approx 50$ Å). This discrepancy can be attributed to (i) uncertainties in the area per molecule before and during the LS/LB transfer and (ii) the potential response of the area per molecule to dehydration, which is well documented for phospholipids[24]. The ratio between IOS and OSC amounts ($D_{OSC}/D_{IOS} \approx 1.6$) shows satisfactory agreement with the single LPS surface ($D_{OSC}/D_{IOS} \approx 1.5$).
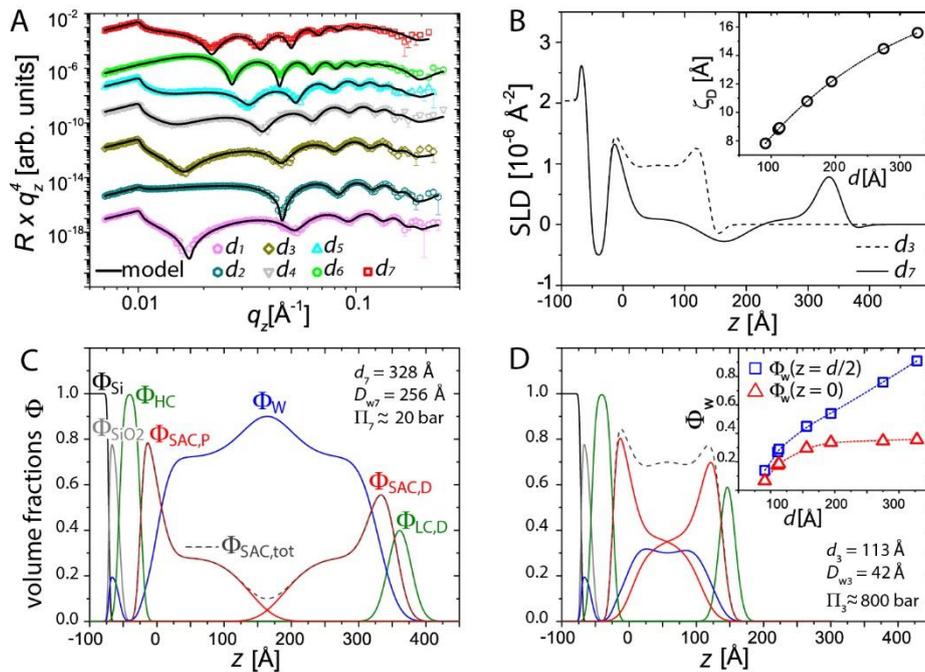
Figure 4: (A) Neutron reflectivity curves (symbols) of interacting LPS monolayers obtained for various relative humidities corresponding to grafting surface separations of d_1 = 91 Å (H_2O), d_2 = 111 Å (D_2O), d_3 = 113 Å (H_2O), d_4 = 155 Å (H_2O), d_5 = 194 Å (H_2O), d_6 = 275 Å (D_2O), and d_7 = 328 Å (H_2O). Solid lines indicate the theoretical reflectivity curves according to the best-matching parameters in the common model. The reduced chi-square deviation is χ^2_{red} = 3.6. (B) SLD profiles for d_3 and d_7 (both H_2O). Inset: Roughness of the distal monolayer as a function of the surface separation according to the best-matching parameters b_0, b_1, and b_2 in Eq. 10. (C and D) Corresponding volume fraction profiles for d_7 and d_3, respectively. The individual volume fraction profiles of proximal and distal saccharides are not unique in lack of SLD contrast. The measurements are only sensitive to the combined profile $\Phi_{SAC,tot}(z)$ = $\Phi_{SAC,P}(z)$ + $\Phi_{SAC,D}(z)$. Inset panel (D): Water volume fraction at the midplane ($z = d/2$) and at the surface ($z = 0$) as a function of the surface separation.

Regarding the d-dependent parameters we first have a look at the roughness of the distal lipid surface, $\zeta_D(d)$. The obtained values of ς_0, ς_∞, and τ_ς in Eq. 9 correspond to an increase of the roughness from $\zeta_D \approx 8$ Å to $\zeta_D \approx 16$ Å with increasing separation (see inset in Fig. 4B). This result appears to reflect a decrease in the confinement of the distal LPS monolayer with the solid substrate, allowing for stronger thermal fluctuations. Moving on with the OSC profiles, we note that, in contrast to our earlier study utilizing selective deuteration[148], the measurements are sensitive to the total saccharide profile, $\Phi_{SAC,tot}(z) = \Phi_{SAC,P}(z)$ + $\Phi_{SAC,D}(z)$, rather than to the individual profiles belonging to each of the two monolayers. Nevertheless, visual inspection of $\Phi_{SAC,tot}(z)$ at the highest hydration level (see Fig. 4C), where OSC overlap at the midplane (i.e., at $z = d/2$) is weak, reveals that the individual profiles at this separation still closely resemble the one of a single LPS surface in bulk aqueous medium, although the plateau volume fraction is already slightly elevated. The absence of a "kink" at the midplane further suggests that there is significant interpenetration, but its extent cannot be quantified in lack of SLD contrast. As a robust result we find that, at large separations, the water fraction is maximal at the midplane (Fig. 4C). In fact, the peak water fraction reaches $\gtrsim 91\%$ at $z = d/2$ at the highest hydration. This is clearly seen from the pronounced central minimum in the H_2O contrast SLD profile (solid line in Fig. 4B) and in contrast to the essentially constant water profile observed for interacting monodisperse PEG brushes [148]. This behavior can be rationalized in terms of

the polydispersity of the O-side chains in combination with their longer persistence length compared to PEG (see Section 3.1): the longer the persistence length the more is the polymer connectivity manifested in the conformation of a brush. At small separation the water fraction is highest closer to the surfaces, which may be qualitatively rationalized in terms of the electric charges associated with the core saccharides, since charged groups do not get dehydrated and collapsed onto each other as easily as uncharged ones. The substantially different d-dependence of the water fraction at the midplane and at the OSC/IOS interfaces ($z = 0$ and $z = d$) is shown in the inset of Fig. 4D. The IOS layer in the interacting system is slightly compressed ($d_{IOS} \approx 24$ Å) with respect to the non-interacting case in the presence of calcium ($d_{IOS} \approx 31$ Å). Overall, the measurements yield considerable structural insight into the response of the saccharide conformation to the approach of two LPS surfaces. Further details on the mutual interpenetration of the O-side chains can be expected from future experiments employing one ordinary LPS surface and one surface composed of perdeuterated LPS molecules.

The low saccharide fraction ($\lesssim 10\%$) at the midplane even at considerable compressive forces of ≈ 20 bar (see Fig. 4C) indicates that a liquid-like aqueous layer of even lower saccharide content exists between neighboring bacteria when they are situated side-by-side, both in the absence of dehydrating pressures and when subject to physiological osmotic pressures. Hydrodynamic pathways for the inter-cellular transport of small-enough molecules will therefore be sustained in colonies and biofilms. At the same time, the observed significant mutual interpenetration of adjacent OSC 'brushes' will contribute to shear friction between adjacent bacteria and, in turn, affect the viscoelastic properties of biofilms.

4. Conclusions

We have prepared single and interacting planar monolayers of wild-type (smooth) LPS from *E. Coli O55:B5.* featuring strain-specific O-side chains. These surfaces mimic the outer surface of Gram-negative bacteria as individua and when mutually interacting in a colony or biofilm. The samples were investigated by NR, providing the so-far most detailed and comprehensive structural characterization of wild-type LPS surfaces. The model used for the interpretation is based on the volume fraction profiles of all chemical components. The saccharide volume

fraction profiles exhibit a clearly bimodal distribution consistent with the picture of a dense and compact saccharide layer accommodating the negatively charged internal oligosaccharides and a more dilute, extended region accommodating the O-side chains. The structure of single solid-supported LPS monolayers is significantly affected by a depletion of calcium: the lateral packing is reduced and water appears to overlap with the hydrocarbon chain region, in line with an earlier study on wild-type LPS multilayers in humidified air[146]. At the same time the internal oligosaccharides become more extended in the perpendicular direction. Both effects can be attributed to enhanced electrostatic repulsion in the absence of divalent cations. For two opposing LPS surfaces we determined the pressure-distance relation, i.e., the dehydrating pressure required in order to bring the surfaces to a certain proximity. The data are well described by the AdG model of interacting polymer brushes for a definition of the uncompressed brush extension which is consistent with the uncompressed conformation of the O-side chains. We were able to interpret the corresponding neutron reflectivity curves obtained at various surface separations in H_2O and D_2O contrasts with a single model involving global and separation-dependent parameters describing the volume fraction profiles. The analysis reveals that the O-side chain conformation is nearly un-perturbed at the largest separation, with only a weak overlap at the midplane. The corresponding central water fraction is as high as ≈ 91 %. Upon surface approach, the water release is heterogeneous, reflecting differences in connectivity and chemical nature between the internal oligosaccharides and the O-side chains. Interacting wild-type LPS surfaces constitute a comparatively realistic model of the surfaces of adjacent Gram-negative bacteria. Even more realistic mimics of bacterial surface interactions may be studied in the future by working under weak interaction pressures and excess water conditions [156] and in the presence of other extracellular biofilm components like sugar-binding lectins [163].

Footnote 1: Closer inspection reveals that the reflectivity minima in the experimental data are not always quite as deep as in the model. This discrepancy can be understood in terms of small variations in the humidity/hydration level during the acquisition time, which leads to a slight additional smearing of the features. This minor effect was not accounted for in the model, because it has negligible influence on the interpretation of the results.

Acknowledgements

Structure and Conformation of Single and Interacting Lipopolysaccharide Surfaces Bearing O-Side Chains

Supporting Information

1) Chemical Structure of Lipopolysaccharides from *E. Coli O55:B5*

The core saccharide of *E. Coli* serotype *O55:B5* is of type R3[152, 164]. It can be divided into inner and outer core. The inner core is formed by three L-glycero-D-mannoheptose units, two 3-deoxy-D-manno-2-octulosonic acid units, one phosphorylethanolamine unit and one N-acetylglucosamine unit. The outer core is formed by one N-acetylglucosamine unit, three glucose units and one galactose unit. The O-Antigen repeat unit is composed of two galactose units, one colitose unit, one N-acetylglucosamine unit and one N-acetylgalactosamine unit [165, 166].

2) Calculation of IOS and OSC SLDs

For the calculation of the SLDs of the internal oligosaccharide (IOS) and O-side chains (OSC) the volumes of all the individual sugar monomers are summed. They were obtained from the Chemspider Database (http://www.chemspider.com/). The SLD follows then from the sum of the scattering lengths of all atoms divided by the total volume. In H_2O, all hydrogen atoms are light hydrogen, in D_2O all labile hydrogen atoms are replaced with deuterium.

IOS:

2* Glucosamine ($C_6H_{13}NO_5$/$C_6H_7D_6NO_5$) (from LipidA), volume = 114.6 mL/mol
(http://www.chemspider.com/Chemical-Structure.390201.html)

2* Dihydrogen phosphate (H_2PO_4 /D_2PO_4) (from LipidA), volume ≈ 45 mL/mol
(http://www.chemspider.com/Chemical-Structure.979.html)

1* Phosphorylethanolamine ($C_2H_8NO_4P$/$C_2H_4D_4NO_4P$), volume = 90.7 mL/mol
(http://www.chemspider.com/Chemical-Structure.990.html)

2* Dihydrogen phosphate (H_2PO_4 /D_2PO_4), volume ≈ 45 mL/mol
(http://www.chemspider.com/Chemical-Structure.979.html)

2* N-acetylglucosamine (C$_8$H$_{15}$NO$_6$/C$_8$H$_{10}$D$_5$NO$_6$), volume = 146.9 mL/mol

(http://www.chemspider.com/Chemical-Structure.74284.html)

3* Glucose (C$_6$H$_{12}$O$_6$/C$_6$H$_7$D$_5$O$_6$), volume = 104 mL/mol

(http://www.chemspider.com/Chemical-Structure.58238.html)

1* Galactose (C$_6$H$_{12}$O$_6$/ C$_6$H$_7$D$_5$O$_6$), volume = 104 mL/mol

(http://www.chemspider.com/Chemical-Structure.388480.html)

3* L-glycero-D-manno-heptose, (C$_7$H$_{14}$O$_7$/C$_7$H$_8$D$_6$O$_7$) volume = 116.1 mL/mol

(http://www.chemspider.com/Chemical-Structure.19980991.html)

2* 3-deoxy-D-manno-2-octulosonic acid (KdO) (C$_8$H$_{14}$O$_8$/C$_8$H$_8$D$_6$O$_8$), volume = 141,4 mL/mol

(http://www.chemspider.com/Chemical-Structure.106511.html)

OSC:

2* Galactose (C$_6$H$_{12}$O$_6$/C$_6$H$_7$D$_5$O$_6$), volume = 104 mL/mol

(http://www.chemspider.com/Chemical-Structure.388480.html)

1* Colitose (C$_6$H$_{12}$O$_4$/C$_6$H$_9$D$_3$O$_4$), volume = 108.4 mL/mol

(http://www.chemspider.com/Chemical-Structure.389006.html)

1* N-acetylglucosamine (C$_8$H$_{15}$NO$_6$/C$_8$H$_{10}$D$_5$NO$_6$), volume = 146.9 mL/mol

(http://www.chemspider.com/Chemical-Structure.74284.html)

1* N-acetylgalactosamine (C$_8$H$_{15}$NO$_6$/C$_8$H$_{10}$D$_5$NO$_6$), volume = 146.9 mL/mol

(http://www.chemspider.com/Chemical-Structure.76020.html)

Figs. S1 and S2 show the resulting IOS and OSC SLDs, respectively, as a function of the water SLD. The following relationships are obtained:

Total volume of the IOS: 1841.6 mL/mol, ($V_{IOS} \approx 3000$ Å^3)

Fully hydrogenated: **C$_{91}$H$_{190}$N$_5$O$_{103}$P$_5$** *SLD: 1.8463 x 10^{-6}* Å^{-2}

Fully deuterated: **C$_{91}$H$_{106}$D$_{84}$N$_5$O$_{103}$P$_5$** *SLD: 4.7071 x 10^{-6}* Å^{-2}

$\rho_{IOS} \approx 2.08$ x 10^{-6} Å^{-2} + 0.41ρ_W

Total volume per OSC repeat unit: 610.2 mL/mol

Fully hydrogenated: $C_{34}H_{66}N_2O_{28}$ *SLD: 1.5831 x 10^{-6} Å^{-2}*

Fully deuterated: $C_{34}H_{43}D_{23}N_2O_{28}$ *SLD: 3.9471 x 10^{-6} Å^{-2}*

$\rho_{OSC} \approx 1.77 \times 10^{-6}$ Å^{-2} + 0.34ρ_W
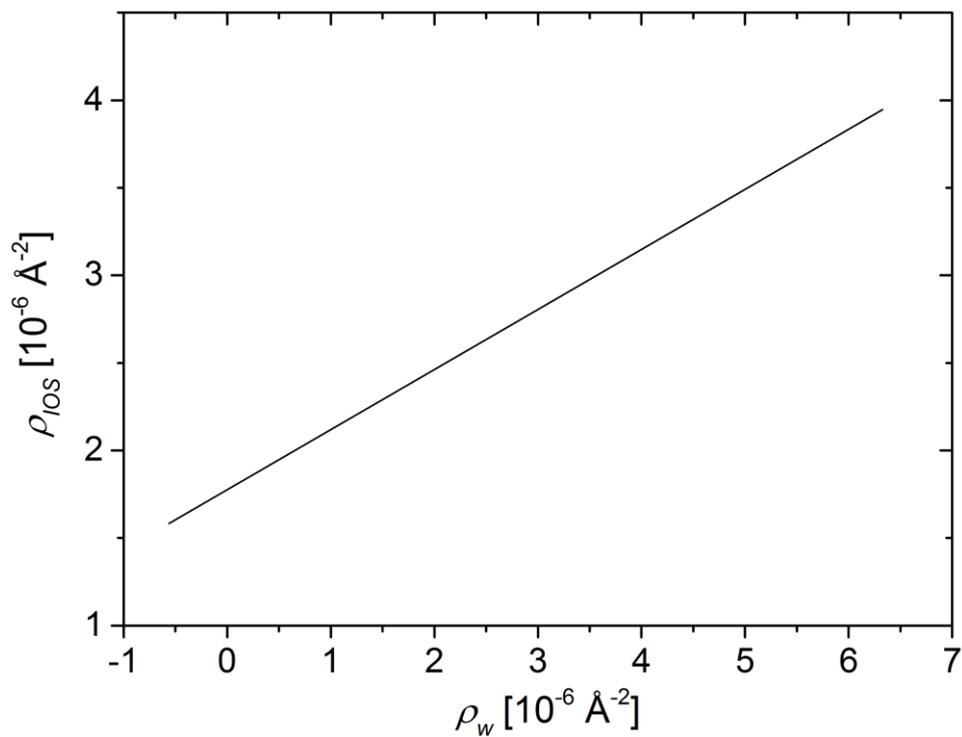
Figure S1: IOS SLD as a function of the water SLD.
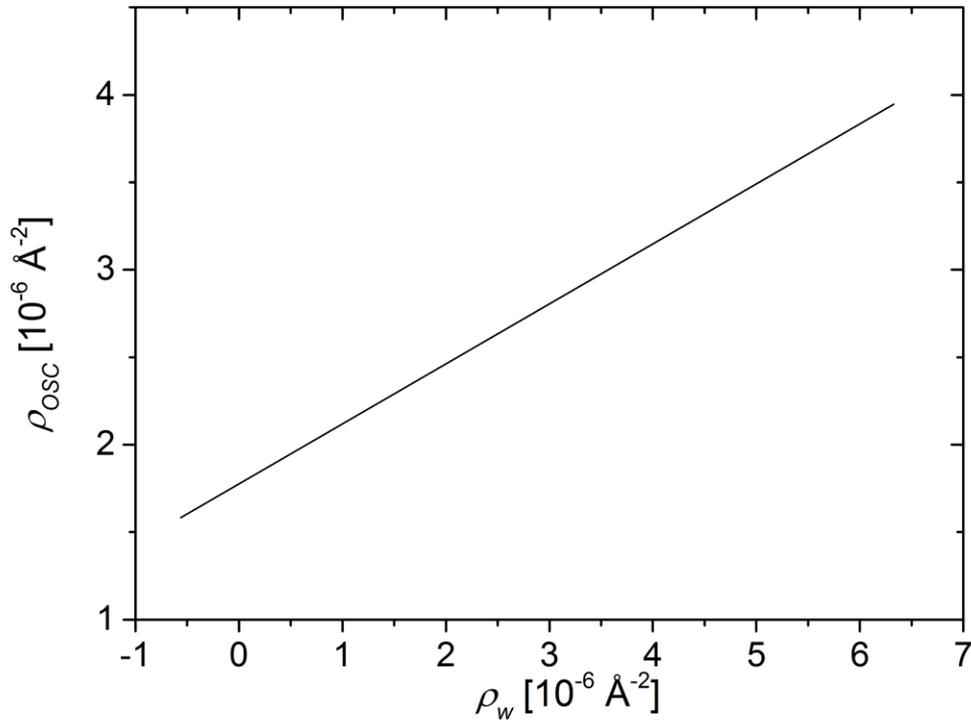
Figure S2: OSC SLD as a function of the water SLD.

3) For the interacting LPSs surfaces, the proximal and distal LPS monolayer are highly symmetric and can therefore be described with common parameters D_{LC}, D_{IOS}, and D_{OSC}

As stated in the main text, a high level of symmetry regarding the amount of material and its structure is found between the proximal and distal LPS monolayers. Figure S3 shows the volume fraction profiles obtained (for the highest grafting surface separation, d_7) after fitting our data considering independent parameters for both surfaces. This means that D_{LC}, D_{IOS}, and D_{OSC} were allowed to differ between the inner and outer layer. The obtained results show that proximal and distal monolayer have almost identical amount of material and structure. In fact, the figure ressembles Figure 4C in the main text, where both layers are described using common parameters. It is therefore not necessary to involve independent parameters for describing the two interacting surfaces.
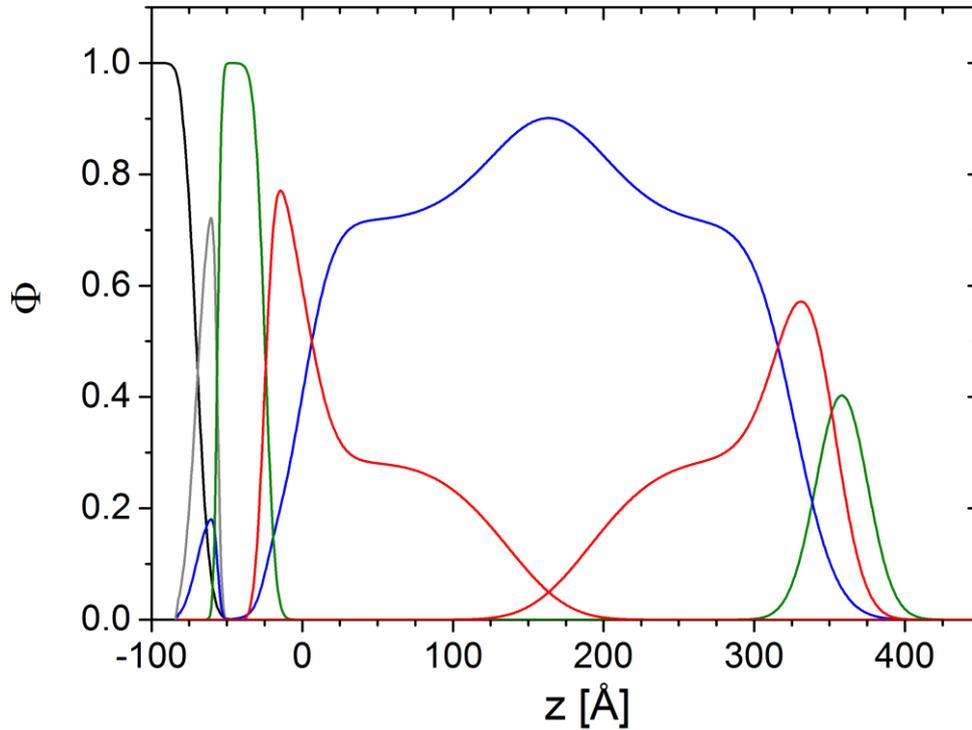
Figure S4: Volume fraction profiles obtained for d_7 considering independent parameters (D_{LC}, D_{IOS}, and D_{OSC}) for describing the proximal and distal layer. The high symmetry between the inner and outer layer allows us to describe them using common parameters.

4) Initial parameter values of the simultaneous fits

Initial values for all parameters concerning the layered structure of the functionalized solid surface were taken from the best-matching results obtained in reference[99]. For the single LPS surface, as well as for the proximal LPS layer under interacting, initial parameters for the IOS and lipid A chains (LC) were taken from reference [42]. The OSC parameters in Eq. 6, Λ and n, were initially set to 100 Å and 2, respectively. For the interacting surfaces, the surface separation d was initially adjusted manually to approximately match the overall sample thickness encoded in the hydration-dependent q_z-positions of the reflectivity minima (see Fig. 4 A). In Eq. 7, $\{\Lambda_0, \tau_\Lambda\}$ were initially set as $\{0$ Å, 100 Å $\}$. $\{n_0 , \tau_n\}$ in Eq. 8 were initially set as $\{2, 0\}$ and $\{\varsigma_0, \varsigma_\infty, \tau_\varsigma\}$ in Eq. 9 as $\{10.0$ Å, 0 Å, 0 Å$\}$.

5) Details of the parameter fitting procedure

To simultaneously fit the adjustable parameters of the common model to a set of experimental reflectivity curves, we utilized the following procedure. Starting from initial parameter values specified above, we first calculated the interfacial SLD profiles $\rho(z)$ corresponding to each condition, i.e. for each contrast fluid in case of single LPS surface and for each humidity level for the interacting LPSs. In the next step, we calculated the reflectivity curves corresponding to the $\rho(z)$ profiles using dynamical reflection theory. To this end the profiles were discretized into hundreds of thin slabs of 2 Å thickness and of constant SLD. The q_z-dependent intensities were then calculated via application of Fresnel's reflection laws at each slab/slab interface using the iterative procedure of Parratt[110]. The procedure was implemented in a self-written fitting program based on the IDL software package (www.harrisgeospatial.com). To optimally constrain all parameters, we simultaneously fit all curves in a set by minimizing the chi-square deviation χ^2 between the entire sets of calculated and experimental reflectivity curves. The best parameter set, with minimal χ^2 was found iteratively using Powell's method[111]. The results were confirmed to be independent of the initial parameter values when they were taken from a physically plausible range. Estimates of the statistical parameter errors, corresponding to the 95% (two-sigma) confidence interval, were derived from the diagonal elements of the corresponding parameter covariance matrix[112].

6) Best-matching model parameters

Single, solid-supported LPS monolayer in *Ca²⁺-loaded buffer*

d_{SiO2}	Φ_w^{SiO2}	$d_{HC} = d_{OTS} + d_{LC}$	d_{IOS}	D_{IOS}	D_{OSC}	Λ_∞	n
17 Å	0.2	31 Å	31 Å	20 Å	30 Å	145 Å	2.5

$\zeta_{Si\text{-}SiO2}$	$\zeta_{SiO2\text{-}OTS}$	$\zeta_{OTS\text{-}LC}$	$\zeta_{LC\text{-}IOS}$	$\zeta_{IOS\text{-}water}$
2 Å	7 Å	12 Å	8 Å	7 Å

Single, solid-supported LPS monolayer in *Ca²⁺-free buffer*

d_{SiO2}	Φ_w^{SiO2}	Φ_w^{LC}	D_{LC}	d_{LC}	d_{IOS}	D_{IOS}	D_{OSC}	Λ_∞	n
21 Å	0.2	0.32	10 Å	15 Å	38 Å	17 Å	22 Å	139 Å	2.7

$\zeta_{Si\text{-}SiO2}$	$\zeta_{SiO2\text{-}OTS}$	$\zeta_{OTS\text{-}LC}$	$\zeta_{LC\text{-}IOS}$	$\zeta_{IOS\text{-}water}$
2 Å	5 Å	9 Å	3 Å	11 Å

Solid-supported interacting LPS surfaces

d_{SiO2}	Φ_w^{SiO2}	d_{OTS}	$d_{LC,P},$ $D_{LC,P},$ $d_{LC,D},$ $D_{LC,D}$	$d_{IOS,P},$ $d_{IOS,D}$	$D_{IOS,P},$ $D_{IOS,D}$	$D_{OSC,P},$ $D_{OSC,D}$
15 Å	0.2	14 Å	17 Å	24 Å	23 Å	37 Å
d_1	d_2	d_3	d_4	d_5	d_6	d_7
91 Å	111 Å	113 Å	155 Å	194 Å	275 Å	328 Å
$\zeta_{Si\text{-}SiO2}$	$\zeta_{SiO2\text{-}OTS}$	$\zeta_{OTS\text{-}LC}$	$\zeta_{LC\text{-}IOS}$	$\zeta_{IOS\text{-}water}$	Λ_∞	Λ_0
2 Å	5 Å	5 Å	6 Å	16 Å	145 Å	145 Å
τ_Λ	n_∞	n_0	τ_n	ς_∞	ς_0	τ_ς
138 Å	2.5	0	150	20 Å	2 Å	230 Å

5. Conclusions

In the present thesis, soft interfaces decorated with hydrophilic polymer brushes have been investigated under controlled interaction conditions. The focus was on pressure-distance curves, determined by ellipsometry, and on the structural aspects of the interaction. The latter, despite their great importance, had so far been vastly neglected because they are inherently difficult to obtain. Here, in order to tackle this long-standing problem, an experimental toolset based on neutron and x-ray reflectometry techniques was established. To this end, dedicated sample environments, sample preparation methods, and data analysis procedures were developed. Experiments were carried out with a solid-supported double-monolayer architecture (Fig. 3, section 2) comprising of lipids and lipid-anchored macromolecules of known chemical structures. The interaction distance was adjusted by controlled osmotic dehydration with the help of a humidity chamber. The samples were investigated by neutron reflectometry, providing the so-far most detailed and comprehensive structural characterization of interacting surfaces displaying end-grafted polymers. The model used for the interpretation of the reflectivity data is self-consistent, based on the volume fraction profiles of all chemical components (Fig. 5, manuscript 1), and simultaneously describes the reflectivity curves at all surface separations (Fig. 5, manuscript 1 and Fig. 4, manuscript 3).

The developed methodology was first applied to a well-defined synthetic system composed of interacting, lipid-anchored poly[ethylene glycol] (PEG) brushes (Fig. 1, manuscript 1). This system served as a proof of principle. However, it is also of great fundamental and technological relevance because brush theories are in need of high-quality experimental data on the conformation of interacting brushes and synthetic polymer brushes are commonly used to for lubrication and biocompatible functionalization. The experimentally determined pressure-distance curves are described surprisingly well by the Alexander-de-Gennes (AdG) model of interacting polymer brushes, which makes strong simplifications (Fig. 4, manuscript 1). In contrast, the pronounced brush interpenetration observed experimentally (Fig. 5, manuscript 1) is not captured by analytical descriptions like AdG and self-consistent-field (SCF) and motivates rigorous, simulation-based theoretical approaches. For the same sample type, but with sulfur-labeled polymer end-points (Fig. 1, manuscript 2), a novel implementation of standing-wave x-ray fluorescence (SWXF) was employed in order

to determine the end-point distributions in dependence on the surface separation (Fig. 5, manuscript 2). The results demonstrate that SWXF is generally suited for the label-free and element specific structural investigation of interacting surfaces. When resolved with high resolution, elemental distributions can yield accurate insight into the molecular configuration of interacting surfaces and its response to changes in the surface separation.

In the second step, the established methodology was used to structurally characterize planar monolayers of wild-type Lipopolysaccharides of the bacterium *Escherichia Coli O55:B5* featuring strain-specific O-side chains (Fig. 1, manuscript 3) under controlled interaction conditions. These surfaces realistically mimic the outer surfaces of Gram-negative bacteria. The neutron reflectometry measurements provided the so-far most detailed and comprehensive structural characterization of wild-type LPS surfaces. The saccharide volume fraction profiles exhibit a clearly bimodal distribution consistent with the picture of a dense and compact saccharide layer accommodating the negatively charged internal oligosaccharides and a more dilute, extended region accommodating the O-side chains (Fig. 2, manuscript 3). The structure of single solid-supported LPS monolayers is significantly affected by a depletion of calcium: the lateral packing is reduced, and water appears to overlap with the hydrocarbon chain region (Fig. 2, manuscript 3). At the same time the internal oligosaccharides become more extended in the perpendicular direction. Both effects can be attributed to enhanced electrostatic repulsion in the absence of divalent cations. The neutron reflectivity curves (Fig. 4, manuscript 3) obtained at various surface separations in two isotopic water contrasts were again fitted with a single model involving global and separation-dependent parameters describing the volume fraction profiles of all chemical components. The analysis revealed that the O-side chain conformation is nearly unperturbed at the largest separation, with only a weak overlap at the midplane (Fig. 4, manuscript 3). It is thus concluded that a liquid-like aqueous layer of even lower saccharide content exists between neighboring bacteria when they are situated side-by-side, both in the absence of dehydrating pressures and when subject to physiological osmotic pressures. Hydrodynamic pathways for the inter-cellular transport of small-enough molecules will therefore be sustained in colonies and biofilms. At the same time, the observed significant mutual interpenetration of adjacent OSC 'brushes' will contribute to shear friction between adjacent bacteria and, in turn, affect the viscoelastic properties of biofilms.

Overall, a powerful toolset for the comprehensive distance-dependent structural characterization of interacting soft interfaces was established in this thesis and applied to examples of great fundamental, technological, and biological relevance. This work can thus serve as a basis for the systematic investigation of the interaction mechanisms between soft interfaces in technology and biology.

6. Outlook

The concepts and experimental methods developed in the framework of this thesis are transferable to a great variety of interacting soft interfaces of relevance in biology as well as in wet- and biotechnology. An important field of application concerns biological membranes and their mutual interaction in the congested physiological environment. As emphasized in the Introduction, membrane interactions are strongly influenced by the chemical composition of their surfaces, which display charged lipid, membrane associated polypeptides, and glycolipids, among others. In the future, the present strategy can be readily extended towards a systematic investigation of membranes with varying molecular composition. Another aspect which may be addressed, is the interaction of membrane models in the presence of co-solutes. For LPS surfaces as investigated here, this may include extracellular biofilm components like sugar-binding lectins.

Regarding standing wave x-ray fluorescence measurements, a clear conclusion drawn in the present work is that the technique is particularly powerful when applied to unimodal element distributions, which occur under fully asymmetric interaction conditions between two interfaces with different chemical compositions. Experiments with well-defined model systems in principle allow for distance-dependent structural investigation with atom-scale precision for several elements simultaneously, including chemical elements contained in the molecules forming the surfaces, as well as counter-ions and co-ions for charged systems. Such measurements, albeit without immediate application, would represent a full structural and thermodynamic description of complex interacting soft interfaces and constitute a rich set of observables for comparison with computer simulations and theory.

Also concerning the theoretical domain, the results obtained interacting synthetic polymer brushes motivates further simulation work, especially on dilute and strongly dehydrated brushes where conformations cannot be predicted by analytical descriptions like AdG and SCF, because they are not only governed by maximization of configurational entropy, but also by their molecular-level interaction with water. For this purpose, fully atomistic treatments like molecular dynamics simulations may be required.

7. Bibliography

[1] O.G. Mouritsen, Life - As a Matter of Fat, Springer2005.

[2] W. Norde, Colloids and Interfaces in Life Sciences, CRC Press, USA (2003).

[3] D.F. Evans, H. Wennerström, The Colloidal Domain - Where Physics, Chemistry, Biology, and Technology Meet, VCH, New York, 1994.

[4] E. Schneck, The Interaction between Soft Interfaces: Forces and Structural Aspects, Advanced Materials Interfaces 4 (2017) 1600349.

[5] B. Alberts, D. Bray, J. Lewis, M. Raff, K. Roberts, J.D. Watson, Molecular Biology of the Cell, 4 ed., Garland Science2002.

[6] B.F. I. Eggens, T. Toyokuni, B. Dean, M. Stroud, S. I. Hakomori, , J. Biol. Chem 264 (1989).

[7] P.C.Y. Lau, T. Lindhout, T.J. Beveridge, J.R. Dutcher, J.S. Lam, Differential lipopolysaccharide core capping leads to quantitative and correlated modifications of mechanical and structural properties in Pseudomonas aeruginosa biofilms, Journal of bacteriology 191(21) (2009) 6618-6631.

[8] L.H.B. D. Faivre, B. F. Matzanke, D. Schuler, Angew. Chem. Int. Ed. 46 (2007).

[9] S.S. A. Rosenhahn, H. J. Kreuzer, M. Grunze, 12 (2010).

[10] C. Bauer, P. Bauduin, J.F. Dufrêche, T. Zemb, O. Diat, Liquid/liquid metal extraction: Phase diagram topology resulting from molecular interactions between extractant, ion, oil and water, The European Physical Journal Special Topics 213(1) (2012) 225-241.

[11] U. Raviv, S. Giasson, N. Kampf, J.-F. Gohy, R. Jérôme, J. Klein, Lubrication by charged polymers, Nature 425(6954) (2003) 163-165.

[12] T.O. M. Yamato, Mater. Today 7(42) (2004).

[13] J.N. Israelachvili, Intermolecular and Surface Forces, 2 ed., Academic Press Inc., London, 1991.

[14] G. Van Meer, D.R. Voelker, G.W. Feigenson, Membrane lipids: where they are and how they behave, Nature reviews molecular cell biology 9(2) (2008) 112-124.

[15] C.M. Wijmans, E.B. Zhulina, G.J. Fleer, Effect of free polymer on the structure of a polymer brush and interaction between two polymer brushes, Macromolecules 27(12) (1994) 3238-3248.

[16] A.K. Kenworthy, K. Hristova, D. Needham, T.J. McIntosh, Range and magnitude of the steric pressure between bilayers containing phospholipids with covalently attached poly (ethylene glycol), Biophysical journal 68(5) (1995) 1921-1936.

[17] J. Als-Nielsen, D. McMorrow, Elements of Modern X-Ray Physics, Wiley, Chichester, 2001.

[18] J. Daillant, A. Gibaud, X-ray and Neutron Reflectivity: Principles and Applications, Springer, Berlin, 2009.

[19] Z. Wei, S.W. Prescott, Scattering approaches to probing surface layers under confinement, Current Opinion in Colloid & Interface Science 20(4) (2015) 253-260.

[20] M. Mezger, H. Reichert, S. Schöder, J. Okasinski, H. Schröder, H. Dosch, D. Palms, J. Ralston, V. Honkimäki, High-resolution in situ x-ray study of the hydrophobic gap at the water-octadecyl-trichlorosilane interface, Proceedings of the National Academy of Sciences 103(49) (2006) 18401-18404.

[21] J. Majewski, T.L. Kuhl, M.C. Gerstenberg, J.N. Israelachvili, G.S. Smith, Structure of phospholipid monolayers containing poly (ethylene glycol) lipids at the air-water interface, The Journal of Physical Chemistry B 101(16) (1997) 3122-3129.

[22] J.N. Israelachvili, R.M. Pashley, Molecular layering of water at surfaces and origin of repulsive hydration forces, (1983).

[23] T.J.S. W. A. Ducker, R. M. Pashley, Nature 353 (1991).

[24] V.A. Parsegian, N. Fuller, R.P. Rand, Measured work of deformation and repulsion of lecithin bilayers, Proceedings of the National Academy of Sciences 76(6) (1979) 2750-2754.

[25] W.A. Hamilton, G.S. Smith, N.A. Alcantar, J. Majewski, R.G. Toomey, T.L. Kuhl, Determining the density profile of confined polymer brushes with neutron reflectivity, Journal of Polymer Science Part B: Polymer Physics 42(17) (2004) 3290-3301.

[26] S.B. Abbott, W.M. de Vos, L.L.E. Mears, M. Skoda, R. Dalgliesh, S. Edmondson, R.M. Richardson, S.W. Prescott, Switching the Interpenetration of Confined Asymmetric Polymer Brushes, Macromolecules 49(11) (2016) 4349-4357.

[27] H. Chen, L. Yuan, W. Song, Z. Wu, D. Li, Biocompatible polymer materials: role of protein-surface interactions, Progress in Polymer Science 33(11) (2008) 1059-1087.

[28] E.P.K. Currie, W. Norde, M.A.C. Stuart, Tethered polymer chains: surface chemistry and their impact on colloidal and surface properties, Advances in colloid and interface science 100 (2003) 205-265.

[29] B. Kolaric, S. Förster, R.v. Klitzing, Interactions between polyelectrolyte brushes in free-standing liquid films: influence of ionic strength, Adsorption and Nanostructure, Springer2001, pp. 195-199.

[30] S. Weinbaum, J.M. Tarbell, E.R. Damiano, The structure and function of the endothelial glycocalyx layer, Annu. Rev. Biomed. Eng. 9 (2007) 121-167.

[31] D.D. Lasic, F.J. Martin, Stealth liposomes, CRC press1995.

[32] O. Lüderitz, M. Freudenberg, C. Galanos, V. Lehmann, E.T. Rietschel, D.H. Shaw, Membrane Lipids of Prokaryotes, Current Topics in Membranes and Transport, edited by S. Razin and S. Rottem, Academic Press, New York (1982) 79.

[33] C. Erridge, E. Bennett-Guerrero, I.R. Poxton, Structure and function of lipopolysaccharides, Microbes Infect. 4 (2002) 837–851.

[34] M. Caroff, D. Karibian, Structure of bacterial lipopolysaccharides, Carbohydr. Res. 338 (2003) 2431.

[35] C. Nilsson, A. Skoglund, A.P. Moran, H. Annuk, L. Engstrand, S. Normark, Lipopolysaccharide Diversity Evolving in Helicobacter pylori Communities through Genetic Modifications in Fucosyltransferases, PLoS One 3(11) (2008) e3811.

[36] T.D. Brock, Can. J. Microbiol. 4(65) (1958).

[37] N.M.D. Islam, T. Itakura, T. Motohiro, Bull. Jpn. Soc. Sci. Fish. 50(1705) (1984).

[38] L. Truelstrup Hansen, J.W. Austin, T.A. Gill, Int. J. Food Microbiol. 66(149) (2001).

[39] M. Vaara, Agents That Increase the Permeability of the Outer Membrane, Microbiol. Rev. 56 (1992) 395-405.

[40] R.E.W. Hancock, D.S. Chapple, Antimicrob. Agents Chemother. 43(1317) (1999).

[41] M.A.A. Grant, W. Bartlomiej, R.J. Allen, P. Cicuta, The role of mechanical forces in the planar-to-bulk transition in growing Escherichia coli microcolonies, Journal of The Royal Society Interface 11(97) (2014) 20140400.

[42] L.A. Clifton, S.A. Holt, A.V. Hughes, E.L. Daulton, W. Arunmanee, F. Heinrich, S. Khalid, D. Jefferies, T.R. Charlton, J.R.P. Webster, C.J. Kinane, J.H. Lakey, An Accurate In Vitro Model of the E. coli Envelope, Angew. Chem. Int. Ed. 54 (2015) 11952–11955.

[43] T.P. Russell, X-Ray and Neutron Reflectivity for the Investigation of Polymers Materials Science Reports 5(171) (1990).

[44] A.-J. Dianoux, G. Lander, Neutron Data Booklet (Old City Publishing, Philadelphia, 2003).

[45] V.F. Sears, Neutron scattering lengths and cross sections, Neutron News 3(26) (1992).

[46] R. Pynn, Neutron scattering by rough surfaces at grazing incidence, Phys. Rev. B 45 (1991).

[47] S.K. Sinha, E.B. Sirota, S. Garoff, X-ray and neutron scattering from rough surfaces, Phys. Rev. B 38 (1988).

[48] D.A. Doshi, E.B. Watkins, J.N. Israelachvili, J. Majewski, Reduced water density at hydrophobic surfaces: Effect of dissolved gases, Proceedings of the National Academy of Sciences of the United States of America 102 (2005).

[49] F. Rehfeldt, R. Steitz, R.v. Klitzing, S.P. Armes, A.P. Gast, M. Tanaka, Reversible

Activation of Diblock Copolymer Monolayers at the Interface by pH Modulation (2): Membrane Interactions at the Solid/Liquid Interface, J. Phys. Chem. B 110 (2006).

[50] T. Schubert, P. Seitz, E. Schneck, M. Nakamura, M. Shibakami, S.S. Funari, O. Konovalov, M. Tanaka, Structure of Synthetic Transmembrane Lipid Membranes at the Solid/Liquid Interface Studied by Specular X-ray Reflectivity, J. Phys. Chem. B 112 (2008).

[51] I.M. Tidswell, B. Ocko, P.S. Pershan, S.R. Wasserman, G.M. Whitesides, J.D. Axe, X-ray specular reflection studies of silicon coated by organic monolayers (alkylsiloxanes), Phys. Rev. B 41 (1990).
[52] E. Schneck, Generic and Specific Roles of Saccharides at Cell and Bacteria Surfaces, Springer Theses (2011).
[53] L. Névot, P. Croce, Characterization of surfaces by grazing X-ray reflection--application to the study of polishing of some silicate glasses, Rev. Phys. Appl. 15 (1980).
[54] L.G. Parratt, Surface studies of solids by total reflection of X-rays, Physical review 95(2) (1954) 359.
[55] T.S. Philipp Gutfreund, Miguel A. Gonzalez, Eric Pellegrini, Mark Laver, Charles Dewhurst, Robert Cubitt, Towards generalized data reduction on achopper-based time-of-flight neutron reflectometer, Cornell University Library (2018).
[56] R.M.A. Azzam, N.M. Bashara, Ellipsometry and polarized light (3rd edition), North-Holland Elsevier Science Publishers (1992).
[57] E. Schneck, E. Scoppola, J. Drnec, C. Mocuta, R. Felici, D. Novikov, G. Fragneto, J. Daillant, Atom-Scale Depth Localization of Biologically Important Chemical Elements in Molecular Layers, Proc. Natl. Acad. Sci. USA 113 (2016) 9521.
[58] J.K. Basu, J.C. Boulliard, B. Capelle, J. Daillant, P. Guenoun, J.W. Mays, J. Yang, Direct Probe of End-Segment Distribution in Tethered Polymer Chains, Macromolecules 40 (2007) 6333-6339.
[59] M.J. Bedzyk, D.H. Bilderback, G.M. Bommarito, M. Caffrey, J.S. Schildkraut, X-ray standing waves: a molecular yardstick for biological membranes, Science 241(4874) (1988) 1788-1791.
[60] M.J. Bedzyk, G.M. Bommarito, M. Caffrey, T.L. Penner, Diffuse-double layer at a membrane-aqueous interface measured with x-ray standing waves, Science 248(4951) (1990) 52-56.
[61] J.M. Bloch, W.B. Yun, X. Yang, M. Ramanathan, P.A. Montano, C. Capasso, Adsorption of counterions to a stearate monolayer spread at the water-air interface: A synchrotron X-ray study, Physical review letters 61(26) (1988) 2941.
[62] W. Bu, M. Mihaylov, D. Amoanu, B. Lin, M. Meron, I. Kuzmenko, L. Soderholm, M.L. Schlossman, X-ray Studies of Interfacial Strontium-Extractant Complexes in a Model Solvent Extraction System, The Journal of Physical Chemistry B 118(43) (2014) 12486-12500.
[63] V. Padmanabhan, J. Daillant, L. Belloni, S. Mora, M. Alba, O. Konovalov, Specific Ion Adsorption and Short-Range Interactions at the Air Aqueous Solution Interface, Physical Review Letters 99 (2007) 086105.
[64] E. Schneck, T. Schubert, O. Konovalov, B. Quinn, T. Gutsmann, K. Brandenburg, R.G. Oliveira, D. Pink, M. Tanaka, Quantitative determination of ion distributions in bacterial lipopolysaccharide membranes by grazing-incidence X-ray fluorescence, Proc. Natl. Acad. Sci. USA 107 (2010) 9147-9151.
[65] A. Körner, W. Abuillan, C. Deichmann, F.F. Rossetti, A. Köhler, O.V. Konovalov, D. Wedlich, M. Tanaka, Quantitative determination of lateral concentration and depth profile of histidine-tagged recombinant proteins probed by grazing incidence X-ray fluorescence, The Journal of Physical Chemistry B 117(17) (2013) 5002-5008.
[66] S. Zheludeva, N. Novikova, N. Stepina, E. Yurieva, O. Konovalov, Molecular organization in protein-lipid film on the water surface studied by x-ray standing wave measurements under total external reflection, Spectrochimica Acta Part B: Atomic Spectroscopy 63(12) (2008) 1399-1403.
[67] E. Schneck, B. Demé, Structural characterization of soft interfaces by standing-wave fluorescence with X-rays and neutrons, Current Opinion in Colloid & Interface Science (2015).
[68] M. Born, E. Wolf, Principles of optics, Cambridge university press1999.
[69] S.T. Milner, Polymer Brushes, Science 251(4996) (1991) 905-914.
[70] P. Flory, Principles of Polymer Chemistry, Cornell University Press, Ithaca, NY (1981).
[71] S. Alexander, J. Phys(Paris) 38(977) (1977).
[72] P.G.d. Gennes, J. Phys. (Paris) 37 (1976).
[73] P.G.d. Gennes, Macromolecules 13 (1980).
[74] S.T. Milner, T.A. Witten, M.E. Cates, Macromolecules 21 (1988).
[75] E.B. Zhulina, O.V. Borisov, V.A. Priamityn, J. Colloid Interface Sci. 137 (1990).

[76] A.M. Skvortsov, A.A. Gorbunov, I.V. Pavluschkov, E.B. Zhulina, O.V. Borisov, V.A. Priamitsyn, Vysokomol. Soedin. Ser. A 30 (1988).

[77] S. Alexander, Adsorption of chain molecules with a polar head: a scaling description, J. Physique (Paris) 38(983-987) (1977).

[78] P.G. de Gennes, Polymers at an Interface: a simplified view, Advances in Colloid and Interface Science 27 (1987) 189-209.

[79] T. Kreer, M.H. Müser, K. Binder, J. Klein, Frictional drag mechanisms between polymer-bearing surfaces, Langmuir 17(25) (2001) 7804-7813.

[80] M.D. Whitmore, R. Baranowski, End-Anchored Polymers: Compression by Different Mechanisms and Interpenetration of Apposing Layers, Macromolecular Theory and Simulations 14 (2005) 75-95.

[81] M. Murat, G.S. Grest, Interaction between grafted polymeric brushes: A molecular-dynamics study, Physical review letters 63(10) (1989) 1074.

[82] G.S. Grest, Interfacial sliding of polymer brushes: A molecular dynamics simulation, Physical review letters 76(26) (1996) 4979.

[83] R.l. Toral, A. Chakrabarti, R. Dickman, Forces between polymer brushes: Monte Carlo simulation of a continuous-space model, Physical Review E 50(1) (1994) 343.

[84] T.L. Kuhl, D. E. Leckband, D. D. Lasic, and J. N. Israelachvili, Modulation of interaction forces between bilayers exposing short-chained ethylene oxide headgroups, Biophys. J. 66 (1994) 1479–1488.

[85] S.P. Kelley TW, Johnson KD, Tirrell M, Frisbie CD, Direct force measurements at polymer brush surfaces by atomic force microscopy, Macromolecules 31(13) (1998) 4297-4300.

[86] D.J. Mulder, T.L. Kuhl, Polymer brushes in restricted geometries, Soft Matter 6(21) (2010) 5401-5407.

[87] T.P. Russell, Methods for Characterizing Polymer Surfaces and Interfaces, Chimia 44 (1990) 312-315.

[88] E. Schneck, I. Rodriguez-Loureiro, L. Bertinetti, E. Marin, D. Novikov, O.V. Konovalov, G. Gochev, Element-Specific Density Profiles in Interacting Biomembrane Models, J. Phys. D 50 (2017) 104001.

[89] L. Tamm, H.M. McConnell, Supported phospholipid bilayers, Biophys. J. 47 (1984) 105-113.

[90] R.M.A. Azzam, N.M. Bashara, Ellipsometry and polarized light, North-Holland. sole distributors for the USA and Canada, Elsevier Science Publishing Co., Inc.1987.

[91] S. Adachi, Model dielectric constants of Si and Ge, Physical Review B 38(18) (1988) 12966.

[92] I.H. Malitson, Interspecimen Comparison of the Refractive Index of Fused Silica, JOSA 55(10) (1965) 1205-1209.

[93] J.E. Wong, F. Rehfeldt, P. Hänni, M. Tanaka, R.v. Klitzing, Swelling behavior of polyelectrolyte multilayers in saturated water vapor, Macromolecules 37(19) (2004) 7285-7289.

[94] J. Ruths, F. Essler, G. Decher, H. Riegler, Polyelectrolytes I: polyanion/polycation multilayers at the air/monolayer/water interface as elements for quantitative polymer adsorption studies and preparation of hetero-superlattices on solid surfaces, Langmuir 16(23) (2000) 8871-8878.

[95] R. Reiter, H. Motschmann, W. Knoll, Ellipsometric characterization of streptavidin binding to biotin-functionalized lipid monolayers at the water/air interface, Langmuir 9(9) (1993) 2430-2435.

[96] J. Katsaras, M.J. Watson, Sample cell capable of 100% relative humidity suitable for x-ray diffraction of aligned lipid multibilayers, Review of Scientific Instruments 71(4) (2000) 1737-1739.

[97] S.A. Tristram-Nagle, Preparation of oriented, fully hydrated lipid samples for structure determination using X-ray scattering, Methods in Membrane Lipids 400 (2007) 63-75.

[98] E. Schneck, A. Schollier, A. Halperin, M. Moulin, M. Haertlein, M. Sferrazza, G. Fragneto, Neutron reflectometry elucidates density profiles of deuterated proteins adsorbed onto surfaces displaying poly (ethylene glycol) brushes: evidence for primary adsorption, Langmuir 29(46) (2013) 14178-14187.

[99] E. Schneck, I. Berts, A. Halperin, J. Daillant, G. Fragneto, Neutron reflectometry from poly (ethylene-glycol) brushes binding anti-PEG antibodies: Evidence of ternary adsorption, Biomaterials 46 (2015) 95-104.

[100] A.P. Dabkowska, J.P. Talbot, L. Cavalcanti, J.R.P. Webster, A. Nelson, D.J. Barlow, G. Fragneto, M.J. Lawrence, Calcium mediated interaction of calf-thymus DNA with monolayers of

distearoylphosphatidylcholine: a neutron and X-ray reflectivity study, Soft Matter 9(29) (2013) 7095-7105.

[101] E. Loizou, L. Porcar, P. Schexnailder, G. Schmidt, P. Butler, Shear-Induced Nanometer and Micrometer Structural Responses in Nanocomposite Hydrogels, Macromolecules 43 (2010) 1041-1049.

[102] S.T.M.a.T.A. Witten, Theory of the Grafted Polymer Brush, Macromolecules 21 (1988) 2610-2619.

[103] S.T. Milner, Polymer brushes, Science 251 (1991) 905-914.

[104] A. Hermelink, G. Brezesinski, Do unsaturated phosphoinositides mix with ordered phosphadidylcholine model membranes?, Journal of lipid research 49(9) (2008) 1918-1925.

[105] I. Szleifer, Statistical thermodynamics of polymers near surfaces, Current Opinion in Colloid & Interface Science 1(3) (1996) 416-423.

[106] L.J. Lis, M. McAlister, N. Fuller, R.P. Rand, V.A. Parsegian, Interactions between neutral phospholipid bilayer membranes, Biophysical journal 37(3) (1982) 657.

[107] E. Schneck, F. Sedlmeier, R.R. Netz, Hydration repulsion between biomembranes results from an interplay of dehydration and depolarization, Proceedings of the National Academy of Sciences 109(36) (2012) 14405-14409.

[108] P. Lyngs Hansen, J.A. Cohen, R. Podgornik, V.A. Parsegian, Osmotic Properties of Poly(Ethylene Glycols): Quantitative Features of Brush and Bulk Scaling Laws, Biophysical Journal 84 (2003) 350-355.

[109] T.A. Witten, L. Leibler, P.A. Pincus, Stress relaxation in the lamellar copolymer mesophase, Macromolecules 23(3) (1990) 824-829.

[110] L.G. Parratt, Surface Studies of Solids by Total Reflection of X-Rays, Phys. Rev 95 (1954) 359-369.

[111] W.H. Press, S.A. Teukolsky, W.T. Vetterling, B.P. Flannery, Numerical Recipes in C, 2 ed., Cambridge University Press, Cambridge, New York, and Port Melbourne, 1992.

[112] P.R. Bevington, D.K. Robinson, Data Reduction and Error Analysis for the Physical Sciences, Mcgraw-Hill, New York, 2003.

[113] E. Schneck, The Interaction between Soft Interfaces: Forces and Structural Aspects, Advanced Materials Interfaces (2016).

[114] I. Eggens, B. Fenderson, T. Toyokuni, B. Dean, M. Stroud, S.I. Hakomori, Specific interaction between Lex and Lex determinants. A possible basis for cell recognition in preimplantation embryos and in embryonal carcinoma cells, Journal of Biological Chemistry 264(16) (1989) 9476-9484.

[115] A. Rosenhahn, S. Schilp, H.J. Kreuzer, M. Grunze, The role of "inert" surface chemistry in marine biofouling prevention, Physical Chemistry Chemical Physics 12(17) (2010) 4275-4286.

[116] M.S. Webb, B.R. Green, Effects of neutral and anionic lipids on digalactosyldiacylglycerol vesicle aggregation, Biochimica et Biophysica Acta (BBA)-Biomembranes 1030(2) (1990) 231-237.

[117] H. Lyklema, Volume III: Liquid-fluid interfaces, Fundamentals of interface and colloid science 3 (2000) iii-v.

[118] B.V. Derjaguin, N.V. Churaev, Surface Forces, Consultants Bureau, New York, 1987.

[119] C.A. Helm, J. Als-Nielsen, Phospholipid monolayer density distribution perpendicular to the water surface. A synchrotron x-ray reflectivity study, EPL (Europhysics Letters) 4(6) (1987) 697.

[120] J. Majewski, T.L. Kuhl, K. Kjaer, M.C. Gerstenberg, J. Als-Nielsen, J.N. Israelachvili, G.S. Smith, X-ray synchrotron study of packing and protrusions of polymer-lipid monolayers at the air-water interface, Journal of the American Chemical Society 120(7) (1998) 1469-1473.

[121] T.L. Kuhl, J. Majewski, J.Y. Wong, S. Steinberg, D.E. Leckband, J.N. Israelachvili, G.S. Smith, A neutron reflectivity study of polymer-modified phospholipid monolayers at the solid-solution interface: polyethylene glycol-lipids on silane-modified substrates, Biophysical journal 75(5) (1998) 2352-2362.

[122] P. Guenoun, A. Schalchli, D. Sentenac, J.W. Mays, J.J. Benattar, Free-standing black films of polymers: a model of charged brushes in interaction, Physical review letters 74(18) (1995) 3628.

[123] J.M. Bloch, M. Sansone, F. Rondelez, D.G. Peiffer, P. Pincus, M.W. Kim, P.M. Eisenberger, Concentration profile of a dissolved polymer near the air-liquid interface: X-ray fluorescence study, Physical review letters 54(10) (1985) 1039.

[124] J. Daillant, L. Bosio, J.J. Benattar, C. Blot, Interaction of cations with a fatty acid monolayer. A grazing incidence x-ray fluorescence and reflectivity study, Langmuir 7(4) (1991) 611-614.

[125] B. Demé, C. Cataye, M.A. Block, E. Maréchal, J. Jouhet, Contribution of galactoglycerolipids to the 3-dimensional architecture of thylakoids, The FASEB Journal 28(8) (2014) 3373-3383.

[126] E. Sackmann, Supported membranes: scientific and practical applications, Science 271(5245) (1996) 43-48.

[127] H.I. Petrache, N. Gouliaev, S. Tristram-Nagle, R. Zhang, R.M. Suter, J.F. Nagle, Interbilayer interactions from high-resolution x-ray scattering, Physical Review E 57(6) (1998) 7014.

[128] A. Cerezo, A.K. Petford-Long, D.J. Larson, S. Pinitsoontorn, E.W. Singleton, The formation mechanism of aluminium oxide tunnel barriers, Journal of materials science 41(23) (2006) 7843-7852.

[129] I. Vrublevsky, V. Parkoun, J. Schreckenbach, G. Marx, Effect of the current density on the volume expansion of the deposited thin films of aluminum during porous oxide formation, Applied Surface Science 220(1) (2003) 51-59.

[130] D.E. Leckband, F.J. Schmitt, J.N. Israelachvili, W. Knoll, Direct force measurements of specific and nonspecific protein interactions, Biochemistry 33(15) (1994) 4611-4624.

[131] J.Y. Wong, T.L. Kuhl, J.N. Israelachvili, N. Mullah, S. Zalipsky, Direct measurement of a tethered ligand-receptor interaction potential, Science 275(5301) (1997) 820-822.

[132] A. Nelson, Co-refinement of multiple-contrast neutron/X-ray reflectivity data using MOTOFIT, Journal of Applied Crystallography 39(2) (2006) 273-276.

[133] S. Stepanov, R. Forrest, Fitting dynamical X-ray diffraction data over the World Wide Web, Journal of Applied Crystallography 41(5) (2008) 958-962.

[134] D.A. Pink, L.T. Hansen, T.A. Gill, B.E. Quinn, M.H. Jericho, T.J. Beveridge, Divalent Calcium Ions Inhibit the Penetration of Protamine through the Polysaccharide Brush of the Outer Membrane of Gram-Negative Bacteria, Langmuir 19 (2003) 8852–8858.

[135] N.H. Lam, Z. Ma, B.Y. Ha, Electrostatic Modification of the Lipopolysaccharide Layer: Competing Effects of Divalent Cations and Polycationic or Polyanionic Molecules, Soft Matter 10 (2014) 7528-7544.

[136] M. Herrmann, E. Schneck, T. Gutsmann, K. Brandenburg, M. Tanaka, Bacterial lipopolysaccharides form physically cross-linked, two-dimensional gels in the presence of divalent cations, Soft matter 11(30) (2015) 6037-6044.

[137] R.G. Oliveira, E. Schneck, B.E. Quinn, O.V. Konovalov, K. Brandenburg, T. Gutsmann, T. Gill, C.B. Hanna, D.A. Pink, M. Tanaka, Crucial roles of charged saccharide moieties in survival of Gram negative bacteria against protamine revealed by combination of grazing incidence x-ray structural characterizations and Monte Carlo simulations, Physical Review E 81(4) (2010) 041901.

[138] C. Jeworrek, F. Evers, J. Howe, K. Brandenburg, M. Tolan, R. Winter, Effects of Specific versus Nonspecific Ionic Interactions on the Structure and Lateral Organization of Lipopolysaccharides, Biophys. J. 105 (2011) 1444-1445.

[139] A.P. Le Brun, L.A. Clifton, C.E. Halbert, B. Lin, M. Meron, P.J. Holden, J.H. Lakey, S.A. Holt, Structural characterization of a model gram-negative bacterial surface using lipopolysaccharides from rough strains of Escherichia coli, Biomacromolecules 14(6) (2014) 2014-2022.

[140] R.G. Oliveira, E. Schneck, B.E. Quinn, O.V. Konovalov, K. Brandenburg, U. Seydel, T. Gill, C.B. Hanna, D.A. Pink, M. Tanaka, Physical mechanisms of bacterial survival revealed by combined grazing-incidence X-ray scattering and Monte Carlo simulation, Comptes Rendus Chimie 12(1) (2009) 209-217.

[141] L.A. Clifton, M.W.A. Skoda, E.L. Daulton, A.V. Hughes, A.P. Le Brun, J.H. Lakey, S.A. Holt, Asymmetric phospholipid: lipopolysaccharide bilayers; a Gram-negative bacterial outer membrane mimic, J. R. Soc. Interface 10(89) (2013).

[142] L.A. Clifton, M.W.A. Skoda, A.P. Le Brun, F. Ciesielski, I. Kuzmenko, S.A. Holt, J.H. Lakey, Effect of divalent cation removal on the structure of gram-negative bacterial outer membrane models, Langmuir 31(1) (2015) 404-412.

[143] E. Schneck, E. Papp-Szabo, B.E. Quinn, O.V. Konovalov, T.J. Beveridge, D.A. Pink, M. Tanaka, Calcium Ions Induce Collapse of Charged O-Side Chains of Lipopolysaccharides from Pseudomonas Aeruginosa, J. R. Soc. Interface 6 (2009) S671.

[144] E. Schneck, R.G. Oliveira, F. Rehfeldt, B. Demé, K. Brandenburg, U. Seydel, M. Tanaka, Mechanical properties of interacting lipopolysaccharide membranes from bacteria mutants studied by specular and off-specular neutron scattering, Physical Review E 80 (2009) 41929.

[145] S. Snyder, D. Kim, T.J. McIntosh, Lipopolysaccharide bilayer structure: effect of chemotype, core mutations, divalent cations, and temperature, Biochemistry 38 (1999) 10758-10767.

[146] N. Kucerka, E. Papp-Szabo, M. Nieh, T.A. Harroun, S.R. Schooling, J. Pencer, E.A. Nicholson, T.J. Beveridge, J. Katsaras, Effect of Cations on the Structure of Bilayers Formed by Lipopolysaccharides Isolated from Pseudomonas aeruginosa PAO1, J. Phys. Chem. B 112 (2008) 8057.

[147] T. Abraham, S.R. Schooling, T.J. Beveridge, J. Katsaras, Monolayer Film Behavior of Lipopolysaccharide from Pseudomonas aeruginosa at the Air-Water Interface, Biomacromolecules 9(10) (2008) 2799-2804.

[148] I. Rodriguez-Loureiro, E. Scoppola, L. Bertinetti, A. Barbetta, G. Fragneto, E. Schneck, Neutron reflectometry yields distance-dependent structures of nanometric polymer brushes interacting across water, Soft Matter 13 (2017) 5767-5777.

[149] D. Marsh, Lateral pressure in membranes, Biochimica et Biophysica Acta 1286 (1996) 183-223.

[150] C.R.H. Raetz, Z. Guan, B.O. Ingram, D.A. Six, F. Song, X. Wang, J. Zao, Discovery of new biosynthetic pathways: the lipid A story, Journal of lipid research 50 (2009) 103-108.

[151] O. Holst, The structures of core regions from enterobacterial lipopolysaccharides - an update, FEMS Microbiology Letters 271(1) (2007) 3-11.

[152] S. Müller-Loennies, L. Brade, H. Brade, Neutralizing and cross-reactive antibodies against enterobacterial lipopolysaccharide, International Journal of Medical Microbiology 297(5) (2007) 321-340.

[153] R. Stenutz, A. Weintraub, G. Widmalm, The structures of Escherichia coli O-polysaccharide antigens, FEMS Microbiology Reviews 30(3) (2006) 382–403.

[154] F. Sebastiani, R. Harvey, S. Khanniche, J.B. Artero, M. Haertlein, G. Fragneto, Diffraction studies on natural and model lipid bilayers, The European Physical Journal Special Topics 213(1) (2012) 355-365.

[155] H. Rasmussen, Ionic and hormonal control of Calcium Homeostasis, Am. J. Med. 50 (1971) 567-588.

[156] S. Micciulla, Y. Gerelli, R.A. Campbell, E. Schneck, A Versatile Method for the Distance-Dependent Structural Characterization of Interacting Soft Interfaces by Neutron Reflectometry, Langmuir accepted (2017).

[157] H.Z. Massoud, J.D. Plummer, E.A. Irene, Thermal Oxidation of Silicon in Dry Oxygen Growth-Rate Enhancement in the Thin Regime I. Experimental Results, Journal of the electrochemical society 132(11) (1985) 2685-2693.

[158] D.S. Snyder, T.J. McIntosh, The Lipopolysaccharide Barrier: Correlation of Antibiotic Susceptibility with Antibiotic Permeability and Fluorescent Probe Binding Kinetics, Biochemistry 39 (2000) 11777-11787.

[159] S.T. Milner, T.A. Witten, Theory of the grafted polymer brush, Macromolecules 21 (1988) 2619-2619.

[160] A.A. Peterson, E.J. McGroarty, High-Molecular-Weight Components in Lipopolysaccharides of Salmonella typhimurium, Salmonella minnesota, and Escherichia coli, Journal of Bacteriology 162(2) (1985).

[161] U.R. Pedersen, C. Leidy, P. Westh, G.n.H. Peters, The effect of calcium on the properties of charged phospholipid bilayers, Biochimica et Biophysica Acta (BBA)-Biomembranes 1758(5) (2006) 573-582.

[162] C. Gourier, F. Pincet, E. Perez, Y. Zhang, J.-M. Mallet, P. Sinay, Specific and non specific interactions involving Le X determinant quantified by lipid vesicle micromanipulation, Glycoconjugate journal 21(3-4) (2004) 165-174.

[163] H. Lis, N. Sharon, Lectins: carbohydrate-specific proteins that mediate cellular recognition, Chemical reviews 98(2) (1998) 637-674.

[164] O. Holst, The structures of core regions from enterobacterial lipopolysaccharides-an update, FEMS Microbiology Letters 271(1) (2007) 3-11.

[165] J.X. Huang, M.A.K. Azad, E. Yuriev, M.A. Baker, R.L. Nation, J. Li, M.A. Cooper, T. Velkov, Molecular Characterization of Lipopolysaccharide Binding to Human α-1-Acid Glycoprotein, Journal of Lipids 2012(Article ID 475153) (2012) 15 pages.

[166] R. Stenutz, A. Weintraub, G. Widmalm, The structures of Escherichia Coli O-polysaccharide antigens, FEMS Microbiology Reviews 30(3) (2006) 382-403.